Investigating Microstructural Effects on Hall-Petch Relationship of Mg-4Al Alloy

by

Mohsen Taheri Andani

A dissertation submitted in partial fulfillment
of the requirements for the degree of
Doctor of Philosophy
(Mechanical Engineering)
in the University of Michigan
2022

Doctoral Committee:

Professor Amit Misra, Chair
Professor John E.Allison
Assistant Professor Ashley Bucsek
Professor Emeritus Wayne Jones
Professor Veera Sundararaghavan

Mohsen Taheri Andani

mtaheri@umich.edu

ORCID iD: 0000-0001-7782-679X

To My Parents,

My Loving Wife Sajedeh

Acknowledgements

I would like to thank my advisor, Prof. Amit Misra, for the continuous academic, emotional, and financial support during my Ph.D. study. His patience and encouragement helped me through hard times. I also very much appreciated his help and time in developing my academic career. I could not have imagined having a better advisor and mentor for my Ph.D. study. You will truly be missed. I'd like to also thank Prof John Allison for his useful discussion and advice during my Ph.D. study. Additionally, great appreciation is paid to Prof. Veera Sundararaghavan and his student Aaditya Lakshmanan for helping me with simulation results that provide important insight into the observed mechanisms in the experiments. I would also like to thank my committee members Prof. John Allison, Prof. Wayne Jones, Prof. Veera Sundararaghavan, and Prof. Ashley Bucsek, for their willingness to serve on my committee as well as support throughout my research.

Many thanks go to my colleagues in Prof. Misra group, Dr. Zhihua Huang, Dr. Ben Derby, Dr. Max Powers, Dr. Qian Lei, Dr. Shujuan Wang, Dr. Yuchi Cui, Dr. Arya Chatterjee, Dr. Bibhu Sahu, Dr. Jeremy Yoo, Nick Etrick, Burt Lien, Metin Kayitmazbatir, Ethan Sprague, Daniel Yin, Forrest Wissuchek, and Arkajit Ghosh. I am also grateful for the help I received from Prof. Allison's group, Dr. Tracy Berman, Dr. Aeriel Murphy, and Duncan Greeley.

I would like to thank my close friends in Ann Arbor, who are very important to me and have me through the highs and lows of graduate school.

I am sincerely grateful to my parents Jafarali and Afsaneh, and my siblings for their unbelievable love and emotional support.

Last but certainly not least, I would also like to thank and dedicate all my success to my lovely wife, Sajedeh, for her continuous support. Thank you very much, Sajedeh.

Table of Contents

List of Tables

List of Figures

Abstract

Grain size strengthening, referred to as the Hall-Petch effect, is a common strategy to improve the yield strength of magnesium (Mg) alloys. Several theoretical studies have reported that the geometry and structure of grain boundaries in polycrystalline materials could impose a significant effect on the Hall-Petch slope. However, experimental observations are primarily limited by the ability of the techniques to accurately quantify the grain boundary barrier strength to dislocation glide and validate these theoretical models. Using high-resolution electron backscatter diffraction (HR-EBSD), the local stress tensor ahead of a slip band blocked by a grain boundary was quantified and coupled with a continuum dislocation pile-up model to assess the barrier strength of specific grain boundaries to specific slip systems, referred to as micro-Hall-Petch coefficient. For basal slip system in a deformed Mg-4Al alloy, the micro-Hall-Petch coefficient $\left(k_{\mu}^{basal}\right)$ varied significantly, from 0.054 to 0.184 $\mathrm{MPa}-\mathrm{m}^{\mathbf{1/2}}$ for nine different grain boundaries and for the prismatic slip systems the micro-Hall-Petch coefficients values ($k_{\mu}^{prismatic}$) vary from 0.138 $\mathrm{MPa.\,m}^{\mathbf{1/2}}$ to 0.685 $\mathrm{MPa.\,m}^{\mathbf{1/2}}$, which are almost three times larger than the calculated values for the basal micro-Hall-Petch. These results were correlated with geometric descriptors of the respective grain boundaries, with three-dimensional GB profile additionally measured via focused ion beam milling. It was found that the angle between the two slip plane traces on the grain boundary plane was the most sensitive parameter affecting k_{μ}^{basal} and $k_{\mu}^{prismatic}$, followed by the angle between the slip directions. A functional form for calculation of k_{μ}^{basal} and $k_{\mu}^{prismatic}$ depending on these two angles is proposed to augment crystal plasticity constitutive models with slip resistance dependent on some measure of the grain size. The method to incorporate the micro Hall-Petch equation into crystal plasticity constitutive models accounting for the microstructural features to understand the coupling between grain size, texture and loading direction was presented. A rate-dependent crystal plasticity model implemented into the open-source PRISMS-CPFE plasticity code is adopted for crystal plasticity simulations. The effect of grain size and texture is accounted for by modifying the slip resistances of individual basal and prismatic slip systems based on the micro Hall-Petch equation. This modification endows each microstructural point with a slip system-level grain size and maximum compatibility factor which are used to modify the slip resistance. Comparisons in the Hall-Petch coefficients are presented between predicted stress-strain curves using original parameters from previous work and subsequently calibrated parameters. This approach provides the foundation to quantitatively model more complicated scenarios of coupling between grain size, texture and loading direction in the plasticity of Mg alloys.

Chapter 1: Introduction

Magnesium (Mg) alloys, owing to their low density, which is 23% that of steel and 66% that of aluminum [1, 2], receive great attention in automobile and aerospace applications. However, the widespread industrial application of Mg alloys is limited by their low strength and limited room temperature formability. Fundamental understanding of defect-defect interactions such as dislocations-grain boundaries (GBs) [3-5], GBs-twins [6, 7], GBs-solute atoms [8-10], dislocations-twins [11], and dislocations-precipitates [12, 13] are key to assess the mechanical properties of polycrystalline materials. Among these interactions, grain boundaries play a crucial role in defining the strengthening of material [14-16], fatigue crack initiation [17], and stress corrosion cracking [18]. Under an applied load, dislocation glide accommodates plastic deformation until impeded by obstacles such as grain boundaries. The pileup of dislocations at a grain boundary successively increases the stress concentration until the boundary barrier to slip transmission is exceeded, resulting in slip transmission and further deformation [19]. Such a theory has been proposed to explain the empirical Hall-Petch equation [20-23], which connects the yield strength of the bulk material to its average grain size: $\sigma_y = \sigma_0 + \frac{k}{\sqrt{L}}$ where σ_y is the yield strength of the material, σ_0 is the friction stress, L is the average grain size, and k is the Hall-Petch coefficient which represents the grain boundary barrier to slip transmission. In connection with the microscopic phenomenon leading to the Hall-Petch effect, Weng [24] proposed that the flow stress of a slip system may be expressed as $\tau = \tau^{\infty} + k_{\mu}.d^{-1/2}$, where at a specific strain, τ^{∞} represents the flow stress of a slip system in a free single crystal, d is the grain size, and k_{μ} is some physical quantity that reflects the strength of the size-effect. This equation is referred to as the micro-Hall-Petch relationship in connection with the extension of the Hall-Petch equation to the slip system level in which the parameter k_μ is the micro-Hall-Petch coefficient [25, 26]. Such a proposal is based on the physical argument by Armstrong *et al*. [27] that in a polycrystalline material, dislocations approaching a grain boundary cannot freely cross the boundary, and therefore, a slip band can sustain higher stress compared to one in a single crystal. The role of individual grain boundary parameters (misorientation, tilt angle, twist angle, etc.) on slip band-GB interactions and its subsequent effect on the flow stress of a slip system and the strength of polycrystalline materials, has been theoretically studied [28, 29] but their calibration is primarily limited by the experimental technique to accurately predict the grain boundary energy or stress field induced by blocked slip band at a grain boundary. Recently, high-resolution electron backscatter diffraction (HR-EBSD) developed by Wilkinson *et al*. [30] enables the measurement of all components of the stress tensor in materials with spatial resolution on the order of 100 nm by assessing changes in Kikuchi diffraction patterns. Previous studies used this technique successfully to examine the residual stress concentration induced from a slip band blocked by a grain boundary in commercial purity titanium [31, 32] and irradiated steel [33, 34]. With the utilization of HR-EBSD in conjunction with a continuum dislocation pile-up model, the specific objectives of this dissertation work are to:

1. Develop an experimental approach to calculate the micro-Hall-Petch coefficient for different slip systems, including basal and prismatic slip systems in Mg-4Al.
2. Determine the role of grain boundary geometric parameters in micro-Hall-Petch coefficient.

3. Develop a functional form to find the micro-Hall-Petch coefficient of the basal and prismatic slip system in Mg-4Al alloy depending on the grain boundary descriptors.

Obtaining such microstructural measurements will help to accurately calibrate the crystal plasticity finite element constitutive model to predict the mechanical response of magnesium alloys, considering both the grain size and geometrical features of grain boundaries.

Chapter 2 provides a review of the literature relevant to the present work, including studies involving the Hall-Petch relationship in Mg alloys and a discussion on the HR-EBSD technique. Chapters 3, 4, and 5 represent studies prepared for publication, resulting in some repetition of background information provided in each chapter. Finally, the conclusion and recommendations for future work are outlined in Chapter 6.

1.1 References

1. Hirsch, J. and T. Al-Samman, *Superior light metals by texture engineering: Optimized aluminum and magnesium alloys for automotive applications.* Acta Materialia, 2013. **61**(3): p. 818-843.
2. Wang, X., et al., *What is going on in magnesium alloys?* Journal of Materials Science & Technology, 2018. **34**(2): p. 245-247.
3. Kacher, J., et al., *Dislocation interactions with grain boundaries.* Current Opinion in Solid State and Materials Science, 2014. **18**(4): p. 227-243.
4. Kacher, J. and I. Robertson, *Quasi-four-dimensional analysis of dislocation interactions with grain boundaries in 304 stainless steel.* Acta Materialia, 2012. **60**(19): p. 6657-6672.
5. Livingston, J. and B. Chalmers, *Multiple slip in bicrystal deformation.* Acta Metallurgica, 1957. **5**(6): p. 322-327.
6. Fernández, A., et al., *Three-dimensional investigation of grain boundary–twin interactions in a Mg AZ31 alloy by electron backscatter diffraction and continuum modeling.* Acta Materialia, 2013. **61**(20): p. 7679-7692.
7. Guo, Y., et al., *Growth of {112¯2} twins in titanium: A combined experimental and modelling investigation of the local state of deformation.* Acta Materialia, 2017. **126**: p. 221-235.
8. De Hosson, J.T., et al., *In situ TEM nanoindentation and dislocation-grain boundary interactions: a tribute to David Brandon.* Journal of materials science, 2006. **41**(23): p. 7704-7719.

9. Garg, P., et al., *Solute effect on strength and formability of Mg: a first-principle study*, in *Magnesium Technology 2017*. 2017, Springer. p. 483-489.
10. Darling, K., et al., *Influence of Mn solute content on grain size reduction and improved strength in mechanically alloyed Al–Mn alloys.* Materials Science and Engineering: A, 2014. **589**: p. 57-65.
11. Zhu, Y., et al., *Dislocation–twin interactions in nanocrystalline fcc metals.* Acta Materialia, 2011. **59**(2): p. 812-821.
12. Choudhuri, D., et al., *Exceptional increase in the creep life of magnesium rare-earth alloys due to localized bond stiffening.* Nature communications, 2017. **8**(1): p. 2000.
13. Choudhuri, D. and S.G. Srinivasan, *Density functional theory-based investigations of solute kinetics and precipitate formation in binary magnesium-rare earth alloys: A review.* Computational Materials Science, 2019. **159**: p. 235-256.
14. Hirth, J.P., *The influence of grain boundaries on mechanical properties.* Metallurgical Transactions, 1972. **3**(12): p. 3047-3067.
15. Cepeda-Jiménez, C., J. Molina-Aldareguia, and M. Pérez-Prado, *Effect of grain size on slip activity in pure magnesium polycrystals.* Acta Materialia, 2015. **84**: p. 443-456.
16. Cepeda-Jiménez, C., J. Molina-Aldareguia, and M. Pérez-Prado, *EBSD-assisted slip trace analysis during in situ SEM mechanical testing: application to unravel grain size effects on plasticity of pure Mg polycrystals.* JOM, 2016. **68**(1): p. 116-126.
17. McDowell, D. and F. Dunne, *Microstructure-sensitive computational modeling of fatigue crack formation.* International journal of fatigue, 2010. **32**(9): p. 1521-1542.
18. West, E., et al. *Influence of irradiation induced microstructure on the stress corrosion cracking behavior of austenitic alloys in supercritical water*. in *Proc. 13th International Conference on Degradation of Materials in Nuclear Power Systems—Water Reactors*. 2007. Canadian Nuclear Society, Toronto, Ontario, Canada.
19. Wang, J., *Atomistic simulations of dislocation pileup: grain boundaries interaction.* JOM, 2015. **67**(7): p. 1515-1525.
20. Hall, E., *Proc. Phys. Soc.* Series B, 1951. **64**: p. 747.
21. Hall, E., *Yield point phenomena in metals and alloys*. 2012: Springer Science & Business Media.
22. Armstrong, R.W., *60 years of Hall-Petch: past to present nano-scale connections.* Materials Transactions, 2014. **55**(1): p. 2-12.
23. Armstrong, R.W., *Hall–Petch k dependencies in nanopolycrystals.* Emerging Materials Research, 2014. **3**(6): p. 246-251.
24. Weng, G., *A micromechanical theory of grain-size dependence in metal plasticity.* Journal of the Mechanics and Physics of Solids, 1983. **31**(3): p. 193-203.
25. Sun, S. and V. Sundararaghavan, *A probabilistic crystal plasticity model for modeling grain shape effects based on slip geometry.* Acta Materialia, 2012. **60**(13-14): p. 5233-5244.
26. Liu, J., et al., *Mean-field polycrystal plasticity modeling with grain size and shape effects for laser additive manufactured FCC metals.* International Journal of Solids and Structures, 2017. **112**: p. 35-42.
27. Armstrong, R., et al., *The plastic deformation of polycrystalline aggregates.* The Philosophical Magazine: A Journal of Theoretical Experimental and Applied Physics, 1962. **7**(73): p. 45-58.

28. Bata, V. and E.V. Pereloma, *An alternative physical explanation of the Hall–Petch relation.* Acta materialia, 2004. **52**(3): p. 657-665.
29. Sangid, M.D., et al., *Energy of slip transmission and nucleation at grain boundaries.* Acta materialia, 2011. **59**(1): p. 283-296.
30. Wilkinson, A.J., G. Meaden, and D.J. Dingley, *High-resolution elastic strain measurement from electron backscatter diffraction patterns: new levels of sensitivity.* Ultramicroscopy, 2006. **106**(4-5): p. 307-313.
31. Britton, T.B. and A.J. Wilkinson, *Stress fields and geometrically necessary dislocation density distributions near the head of a blocked slip band.* Acta Materialia, 2012. **60**(16): p. 5773-5782.
32. Guo, Y., T. Britton, and A. Wilkinson, *Slip band–grain boundary interactions in commercial-purity titanium.* Acta Materialia, 2014. **76**: p. 1-12.
33. Johnson, D., et al., *Quantitative analysis of localized stresses in irradiated stainless steels using high resolution electron backscatter diffraction and molecular dynamics modeling.* Scripta Materialia, 2016. **116**: p. 87-90.
34. Johnson, D., et al., *Quantitative Linkage between the Stress at Dislocation Channel–Grain Boundary Interaction Sites and Irradiation Assisted Stress Corrosion Crack Initiation.* Acta Materialia, 2019.

Chapter 2: Literature Review and Background

In this chapter, a review of the literature on understanding the aims and objectives outlined in Chapter 1 and the experimental methods are discussed. Section 1 describes the deformation behavior in magnesium alloys. Section 2, a general description of the Hall-Petch relationship, dislocation pile-up theory, and the observed Hall-Petch behavior in magnesium alloys are discussed. Finally, Section 3 describes the concepts of High-Resolution Electron Backscatter Diffraction (HR-EBSD) and how to measure the elastic stress using this novel technique.

2.1 Deformation Behavior in Magnesium Alloys

2.1.1 Slip System and Twinning in Mg alloys

Magnesium (Mg) has a Hexagonal Close-Packed (HCP) structure that exhibits multiple slip systems, including basal, prismatic, pyramidal, and tension and compression twinning systems, as shown in Figure 2.1. Mg is plastically anisotropy due to the wide range of the critical resolved shear stress (CRSS) values of the different slip and twin systems, as shown in Figure 2.2 [1]. There are three basal slip systems (0001) $< 11\bar{2}0 >$, but only two are independent. Moreover, since basal slip systems cannot provide the strain along the <c>-axis, the non-basal slip is required for arbitrary shape change of a polycrystal [2]. There are two types of non-basal slip: prismatic and pyramidal. In the prismatic slip systems, <a> dislocation with Burgers vector 1/3 $< 11\bar{2}0 >$ can slip on the first order plane $(10\bar{1}0)$, and <c+a> dislocation with Burgers vector along c axis can slip on both the first order prismatic plane $(10\bar{1}0)$ and the second-order prismatic planes $(11\bar{2}0)$. In the pyramidal slip systems, the first-order and the second-order planes are $(10\bar{1}1)$ and $(11\bar{2}2)$, respectively. Both <a> dislocation and <c+a>-dislocation with Burgers vector along $<11\bar{2}3>$ can slip on the first-order pyramidal planes. But only <c+a> dislocation can slip on the second-order pyramidal planes. From Figure 2.2, it is obvious that the CRSS for basal slip is much smaller than that of the non-basal slip, indicating the predominance of basal slip during plastic deformation and the remarkable CRSS anisotropy. According to the Taylor criteria, at least five independent slip systems must be activated to have an arbitrary shape change. However, Taylor's criterion is usually not satisfied for HCP Mg alloys because it has only two independent slip systems in the basal plane. This causes twinning, one of the important modes of deformation in Mg alloys. Twinning is categorized as compression twin $\{10\bar{1}1\}$and tension twin $\{10\bar{1}2\}$. The activation of each type depends on the applied stress vector. The tensile twin occurs at a much higher rate than the compression twin because of its lower critical stress to nucleate. The difference between critical twinning stresses for compression and tensile twin gives rise to the tension-compression yield asymmetry [3], which provides another challenge in the formability of Mg alloys for large-scale industrial applications.

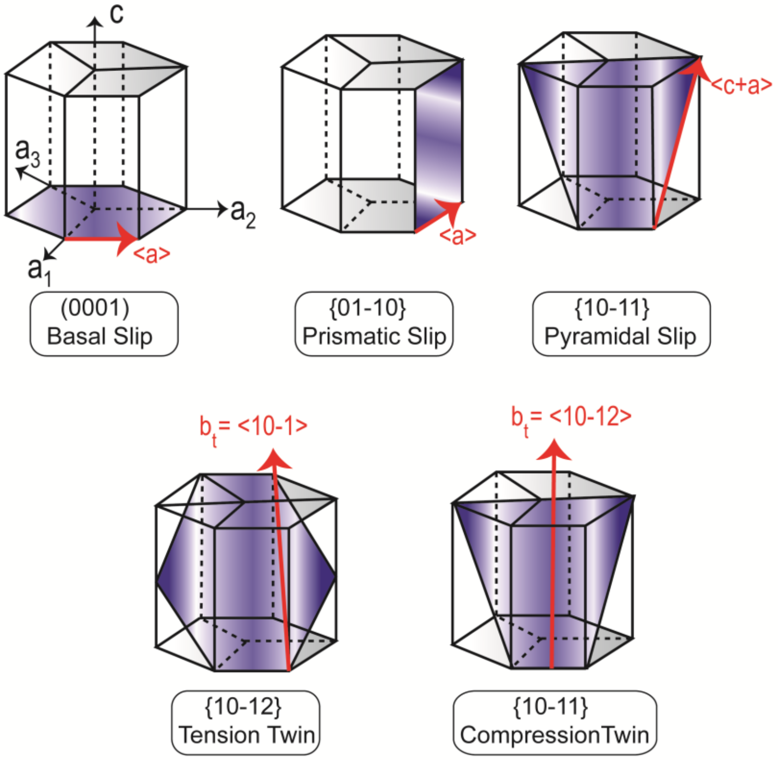

Figure 2.1 Deformation systems in Mg. Red arrows represent Burgers vector, and purple shaded area represents the slip planes

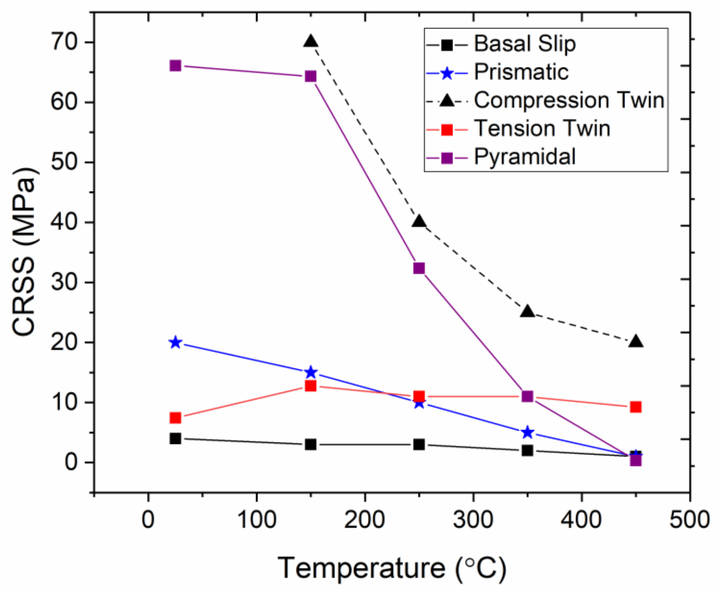

Figure 2.2 The CRSS of Mg at various temperatures [1]

2.2 Hall-Petch Relationship

Grain refinement is one of the most common techniques used to improve the yield strength of polycrystalline materials according to the well-known Hall-Petch equation [4-7], which connects the yield strength of the bulk material (σ_y) to its average grain size (D) : $\sigma_y = \sigma_0 + \frac{K}{\sqrt{D}}$ where σ_0 is the friction stress and K is the macroscopic Hall-Petch coefficient (HPC), which represents the collective strengthening effect of all the grain boundaries in the polycrystal. One of the most common mechanisms that the Hall-Petch effect is attributed to is the strength needed for a dislocation pile-up to overcome the grain boundary (treated as an obstacle) to effect slip transmission.

2.2.1 Dislocation Pile-up Theory

The following method to construct a model for a slip band based on the theory of continuous distribution of dislocations is adapted from Hirth and Lothe [8]. A slip band is idealized to a one-dimensional interval $[-L/2, L/2]$, where the boundaries of the domain represent grain boundaries (Figure 2(a)). At any point $x \in [-L/2, L/2]$ a dislocation density field $\rho(x)$ is prescribed, so that the total number of dislocations in a differential element δx is $\delta n(x) = \rho(x)\delta x$. A continuous density field in one-dimension is a continuum representation of straight, infinite dislocations of positive and negative type for a given Burgers vector. The sign of the density field refers to the group of dislocations of the corresponding sign. An applied stress field exerts a configurational force on the dislocation of the Peach-Koehler type. Additionally, there is a long-range stress field due to dislocations in the medium (by virtue of their presence), which imposes a configurational force on a dislocation present anywhere else in the medium. Any net force acting on the dislocations drives the system to an equilibrium state which is characterized by zero net configurational force. Because the expressions for the stress fields of dislocations are derived based on linear elasticity, the net configurational force is simply a sum of individual force terms. The equilibrium condition is then expressed mathematically as:

$$\tau(x)b + \frac{Gb^2}{2\pi\kappa}\int_{-\frac{L}{2}}^{\frac{L}{2}} \frac{\rho(x')}{x - x'}dx' = 0 \tag{2.2}$$

where $\tau(x)$ denotes the applied shear stress resolved along the slip system, L is the grain size, G the shear modulus for an isotropic elastic material, b the Burgers vector strength, and κ = 1 (for screw dislocations) or κ = 1-υ (for edge dislocations). It is noted that unalloyed Mg is essentially elastically isotropic so that the Eqn.2.1 is a reasonable approximation. Now given $\tau(x)$, the density field $\rho(x)$ satisfying the equilibrium equations needs to be computed. For this purpose, Eqn.1 is recast into a simpler mathematical form as follows

$$\frac{1}{\pi}\int_{-1}^{1} \frac{f(\xi')}{\xi' - \xi}d\xi' = \frac{2\kappa\tau\left(\frac{L}{2}\xi\right)}{Gb}$$

$$\equiv \mathcal{H}_\xi[f(\xi')] = \frac{2\kappa\tau\left(\frac{L}{2}\xi\right)}{Gb} \tag{2.3}$$

where $= \frac{2x}{L}$, $\xi' = \frac{2x\prime}{L}$, $f(\xi') = \rho\left(\frac{L}{2}\xi'\right)$ and $\mathcal{H}_\xi[f(\xi')]$ denotes the finite Hilbert transform of the function $f(\xi')$ expressed in terms of the new variable ξ. Solving for the dislocation density field involves inverting the operator $\mathcal{H}$, a classical problem whose solution has been presented elsewhere [9, 10]. The special case of a spatially constant resolved shear stress $\tau(x) = \tau_0$ is considered in this study resulting in

$$\mathcal{H}_\xi[f(\xi')] = \frac{2\kappa\tau_0}{Gb}$$

$$\Rightarrow f(\xi') = \frac{2\kappa\tau_0}{Gb}\frac{\xi'}{\sqrt{1-\xi'^2}} + \frac{C}{\sqrt{1-\xi'^2}}$$

$$\Rightarrow \rho(x) = \frac{2\kappa\tau_0}{Gb}\frac{x}{\sqrt{\left(\frac{L}{2}\right)^2 - x^2}} + \frac{CL}{2\sqrt{\left(\frac{L}{2}\right)^2 - x^2}} \tag{2.4}$$

where C is a constant appearing due to the homogeneous solution of the integral equation. This constant can be related to the net Burgers vector (supplemental material) considering all the dislocations appearing in the slip band, which for simplicity is assumed to be zero. In other words, there is an equal number of dislocations of both positive and negative type. Accordingly, the stress ahead of the pile-up (pileup-stress) due to the dislocation distribution alone takes the form

$$\tau_p(X) = \tau_0\left[\frac{X + \frac{L}{2}}{\sqrt{\left(X + \frac{L}{2}\right)^2 - \left(\frac{L}{2}\right)^2}} - 1\right] \tag{2.5}$$

Where X= $x - \frac{L}{2}$, is the distance from the grain boundary, as denoted in Figure 2.2(a).

In comparison with experiments, it is noted that the theoretical prediction for the pile up stress must not include the effect of the resolved stress, because the experiment measures the residual stress in the adjacent grain. This residual stress is considered to arise primarily from the development of a dislocation distribution in the slip band reminiscent of a dislocation pile-up. The sole purpose of the resolved shear stress is to generate this dislocation distribution which develops irreversibly, and hence, retains the functional form even after removal of the resolved shear stress. In other words, the generated dislocation distribution is assumed to change negligibly so that the form of the pileup stress is not affected significantly. These simplifications are debatable but in the interest of obtaining a simple analytical form, are suggested to be an appropriate starting point.

The function $\tau_p(X)$ (stress ahead of the pile up) for different values of τ_0 is plotted in Figure 2.2(b).

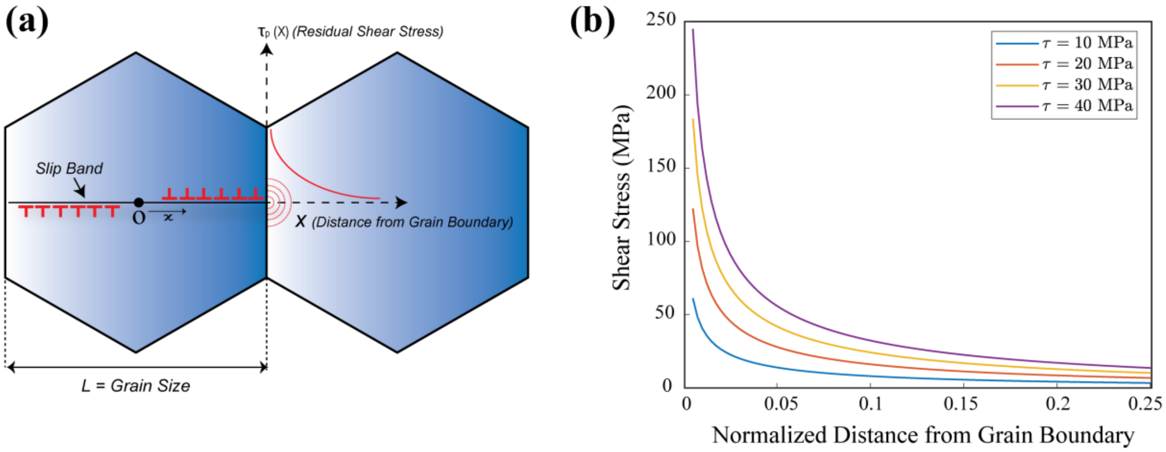

Figure 2.3 (a) Continuum model of dislocation pile-up at a grain boundary. The red curve represents the stress ahead of the pile-up based on Eqn.4. (b) Shear stress ahead of pile-up for different slip system resistance (s^α) - the pileup-stress increases proportionally with the resolved shear stress.

To purport a particular form of the resolved shear stress, two assumptions are made.

(1) The resolved shear stress on the slip system equals the initial slip system resistance, which arises by neglecting the phenomenon of work hardening on that slip system. In other words, the applied shear stress required to equilibrate a dislocation distribution is identical to the initial slip system resistance which must be overcome to produce the slip band and accommodate the majority of the applied deformation.

(2) It is assumed that the classical Hall-Petch relationship may be extended to the slip system level, formerly termed as “micro-Hall-Petch” relation [11, 12]. It is one way of separating the contribution of grain size from the local lattice resistance in the initial slip system resistance. Additionally, because the pile-up model doesn’t take into account the grain

boundary character, the grain boundary effect is subsumed in the estimates of the micro-Hall-Petch coefficients. Accordingly, the slip system resistance is expressed in the following form:

$$s^{\alpha} = \tau_0^{\alpha} + \frac{k^{\alpha}}{\sqrt{L}} \tag{2.6}$$

where τ_0^{α} is the flow stress of slip system α of a theoretically infinite single crystal, k^{α} the micro-Hall-Petch coefficient of the slip system α signifying the strength of the size effect, and L is the slip system-level grain size, which in this case represents the length of the slip band across an entire grain. In the context of the current experiment, L corresponds to the length of the slip trace measured along the direction perpendicular to the dislocation (infinite edge or screw) line and slip plane normal of the slip system from one-grain boundary to the opposite. Subsequently, we refer to L as the grain size. Then substituting Eqn.2.5 in Eqn.2.4 yields:

$$\tau_p(X) = \left(\tau_0^{\alpha} + \frac{k^{\alpha}}{\sqrt{L}}\right)\left[\frac{X + \frac{L}{2}}{\sqrt{\left(X + \frac{L}{2}\right)^2 - \left(\frac{L}{2}\right)^2}} - 1\right] \tag{2.7}$$

2.2.2 Hall-Petch Relationship in Magnesium

The Hall-Petch relationship was initially proposed based on isotropic materials. However, it is also applicable for plastically anisotropic materials such as Mg alloys but with more complexity. Table 2-1 summarizes a review of Hall-Petch coefficients in Mg alloy AZ31[13]. It can be found that the K value is relevant to the processing condition, loading direction, and grain size. For example, the K value for AZ31 changes from 0.304 $\mathrm{MPa.m^{1/2}}$ to 0.161 $\mathrm{MPa.m^{1/2}}$ by changing the processing method from extrusion to friction stir processing [14]. The influence of loading direction, processing method, and grain size is conclusively related to the deformation modes in Mg alloy. As described in section 2.1.1, the possible deformation modes in Mg alloys are complicated. A comprehensive study is needed to uncover the role of texture in K values in Mg alloys.

Table 2.1 Literature review of the H-P slopes (k) in Mg alloys as a function of the processing condition and loading path within a given range of grain size (d). FSP, ECAP, AD and PD represent the friction stir processing, equal-channel angular processing, advancing direction and processing direction, respectively. RD, TD, and ND refer to the rolling, transverse and normal direction of a rolled plate, respectively. ED and FD are the extrusion direction and flow direction of a rod [13].

Sample	**Processing**	**Loading path**	**d (μm)**	**k ($\mathrm{MPa.m^{1/2}}$)**
AZ31 [15]	Rolling	Tension//TD	26–78	0.411
AZ31 [15]	Rolling	Tension//ND	26–78	0.228
AZ31 [16]	Rolling	Tension//RD	5–25	0.319
AZ31[17]	Rolling	Tension//RD	5–17	0.231
AZ31 [17]	Rolling	Tension//RD	5–21	0.250
AZ31 [18]	Rolling	Tension//RD	2–55	0.209
AZ31 [19]	Rolling	Tension//RD	13–140	0.281
AZ31 [19]	Rolling	Tension//TD	13–140	0.272
AZ31 [14]	Extrusion	Tension//ED	2.5–8	0.304
AZ31 [14]	FSP	Tension//AD	2.6–6.1	0.161
AZ31 [20]	Extrusion	Compression//ED	3–23	0.291
AZ31 [21]	Extrusion	Compression//ED	3–11	0.390
AZ31 [21]	Extrusion	Tension//ED	3–11	0.303

AZ31 [22]	FSP	Tension//PD	1–25	0.119
AZ31 [22]	FSP	Tension//TD	1–25	0.236
AZ31 [23]	Rolling	Tension//RD	13–43	0.207
AZ31 [23]	Rolling	Compression//RD	13–43	0.472
AZ31 [24]	ECAP	Tension//FD	3–33	0.205
AZ31 [25]	ECAP	Tension//ED	2–8	0.180
AZ31 [26]	ECAP	Tension//ED	5–35	0.170
AZ31 [27]	ECAP	Tension//ED	2–8	0.203

2.3 High Resolution Electron Backscatter Diffraction (HR-EBSD)

In various applications, from structural engineering parts to semiconductor components, it is necessary to understand the state of stress fields in localized regions in the materials [28]. For example, strain accumulation in semiconductors could cause degradation of the device [29]; and stress concentration at twin/parent interface could result in crack initiation in polycrystalline materials [30]. For these reasons, experimental methods that can measure the local elastic stress/strain are desirable. Figure 2.4 summarizes the spatial resolution and strain sensitivity of the most commonly developed techniques. X-Ray [31] and Neutron Diffraction [32] methods provide strain sensitivity in the order of 10^{-4} but relatively poor spatial resolution. The Hole Drilling technique is limited to macroscopic measurement due to poor strain sensitivity and spatial resolution [33]. Spectroscopy-based measurement methods such as CL [34] and micro-Raman [35] have about one-micron spatial resolution and cannot determine full strain tensor [36]. The high-resolution SEM digital image correlation (DIC) method obtains the deformation field by comparing before and after deformation images. This type of measurement provides the strain sensitivity of 10^{-3} and spatial resolution into sub-micron scale. Still, the strain information related to the state before the first captured image cannot be measured [37]. The highest spatial resolution can be achieved using transmission electron microscopy (TEM) based techniques such as convergent beam electron diffraction (CBED) [38]. However, sample preparation and strain relaxation due to small sample thickness are significant issues in such techniques. The cross correlation-based EBSD strain characterization technique (HR-EBSD) is a novel measurement technique that provides the high spatial resolution that electron diffraction techniques can offer while not suffering so much from sample preparation [36]. This technique measures the elastic strain and lattice rotation by cross-correlating electron backscatter patterns to capture a small shift of feature between two patterns [39-42].

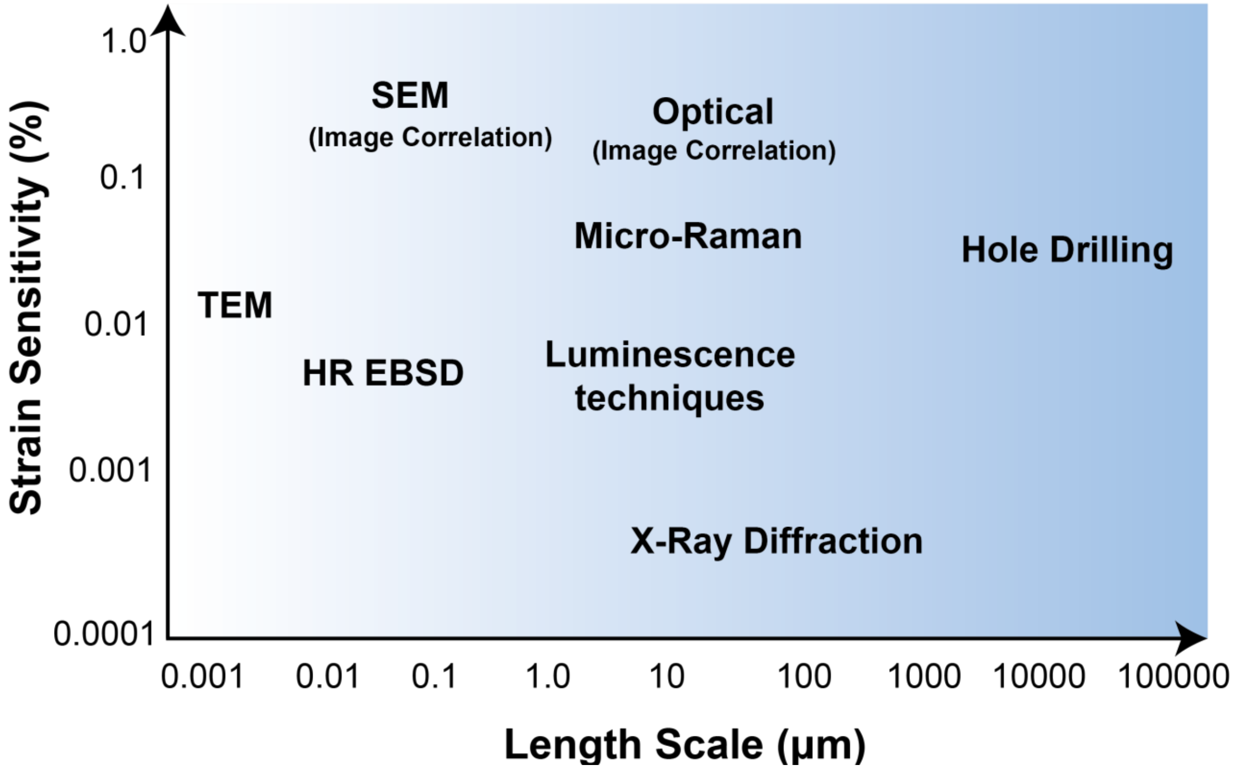

Figure 2.4 Strain sensitivity and spatial resolution related with different strain characterization methods [43].

2.3.1 Effect of Elastic Strain on Kikuchi Pattern

According to Bragg's law, changes in lattice spacing due to elastic strain results in changing the bandwidth in the diffraction pattern, followed by a shift of the zone axis. As it is shown in Figure 2.5, if the lattice is bent, in addition to zone axis shift, there will also be blurring of the edges of the diffraction bands [44].

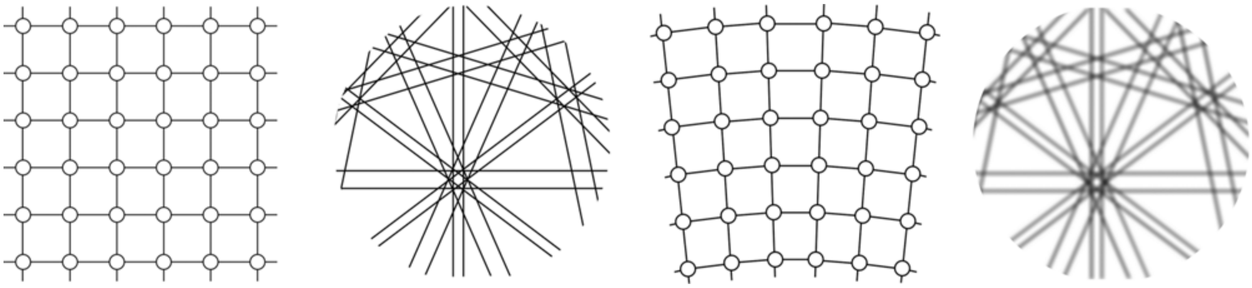

Figure 2.5 Crystal lattice and related diffraction pattern in the undistorted state (left) and distorted state (right) [44].

2.3.2 Linking Pattern Shift to Strain

The below method was developed by Wilkinson *et al*. [36, 40-42] and it was improved by Britton and Wilkinson [45, 46]. The following is a generalized description adopted from [28] .

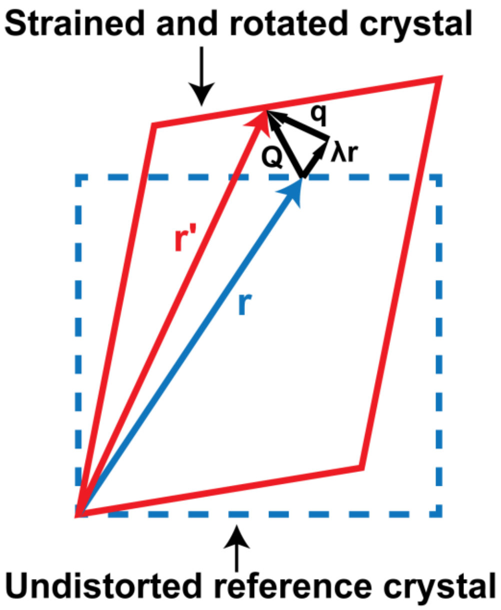

Figure 2.6 Schematic diagram showing exaggerated zone axis (**r**) shift from the undeformed state (blue) to deformed state (red), adopted from [36].

As is shown in Figure 2.6, an arbitrary strain and rigid body rotation change a vector **r** from reference crystal to r' in deformed crystal. The change from **r** to r' can be described by a strain gradient tensor **A**:

$$\mathbf{A} - \mathbf{I} = \begin{pmatrix} \frac{\partial u_1}{\partial x_1} & \frac{\partial u_1}{\partial x_2} & \frac{\partial u_1}{\partial x_3} \\ \frac{\partial u_2}{\partial x_1} & \frac{\partial u_2}{\partial x_2} & \frac{\partial u_2}{\partial x_3} \\ \frac{\partial u_3}{\partial x_1} & \frac{\partial u_3}{\partial x_2} & \frac{\partial u_3}{\partial x_3} \end{pmatrix} \tag{2.8}$$

where **u** = $(u_1\ u_2\ u_3)$ is the displacement at position **x** = $(x_1\ x_2\ x_3)$ and **I** is the identity matrix.

Therefore,

$$\boldsymbol{r}' = \mathbf{Ar} \tag{2.9}$$

The strain and rotation lead to displacement **Q**:

$$\mathbf{Q} = \boldsymbol{r}' - \mathbf{r} = (\mathbf{A} - \mathbf{I})\,\mathbf{r} \tag{2.10}$$

The EBSD technique can only measure the projection of **Q** onto phosphor screen, which is represented by **q**:

$$\mathbf{q} = \mathbf{Q} - \boldsymbol{\lambda}\mathbf{r} = \{\mathbf{A} - (\boldsymbol{\lambda} + 1)\mathbf{I}\}\mathrm{x}\mathbf{r} \tag{2.11}$$

The component of the vector **q** can be calculated using the above equation and some mathematical manipulation [43]:

$$q_1 = r_1 e_{xx} + r_2 e_{xy} + r_3 e_{xz} - \lambda r_1 \tag{2.12}$$

$$\mathrm{q_2 = r_2 e_{yy} + r_1 e_{xy} + r_3 e_{yz}} - \lambda \mathrm{r_2} \tag{2.13}$$

$$\mathrm{q_3 = r_3 e_{zz} + r_1 e_{xz} + r_2 e_{yz}} - \lambda \mathrm{r_3} \tag{2.14}$$

where e_{ij} is the displacement gradient described in equation (2.8), and λ is an unknown constant. The constant λ can be eliminated by combining pairs of the above equations and yields two equations in eight variables:

$$\mathrm{r_1 r_3}\left[\frac{\partial \mathrm{u_1}}{\partial \mathrm{x_1}} - \frac{\partial \mathrm{u_3}}{\partial \mathrm{x_3}}\right] + \mathrm{r_2 r_3}\frac{\partial \mathrm{u_1}}{\partial \mathrm{x_2}} + \mathrm{r_3}^2\,\frac{\partial \mathrm{u_1}}{\partial \mathrm{x_3}} - \mathrm{r_1}^2\,\frac{\partial \mathrm{u_3}}{\partial \mathrm{x_1}} - \mathrm{r_2 r_1}\frac{\partial \mathrm{u_3}}{\partial \mathrm{x_2}} \tag{2.15}$$

$$= \mathrm{r_3} q_1 - \mathrm{r_1} q_3$$

$$\mathrm{r_2 r_3}\left[\frac{\partial \mathrm{u_2}}{\partial \mathrm{x_2}} - \frac{\partial \mathrm{u_3}}{\partial \mathrm{x_3}}\right] + \mathrm{r_1 r_3}\frac{\partial \mathrm{u_2}}{\partial \mathrm{x_1}} + \mathrm{r_3}^2\,\frac{\partial \mathrm{u_2}}{\partial \mathrm{x_3}} - \mathrm{r_2}^2\,\frac{\partial \mathrm{u_3}}{\partial \mathrm{x_2}} - \mathrm{r_2 r_1}\frac{\partial \mathrm{u_3}}{\partial \mathrm{x_1}} \tag{2.16}$$

$$= \mathrm{r_3} q_2 - \mathrm{r_2} q_3$$

Because shifts are only measured in the phosphor screen, so $Q_3 = 0$, therefore, from equation (2.11):

$$\mathrm{q_3} = -\lambda \mathrm{r_3} \tag{2.17}$$

The right side of equations (2.15) and (2.16) can then be written as:

$$\mathrm{r_3 q_1 + r_1 q_3 = r_3(q_1} + \lambda \mathrm{r_1)} \tag{2.18}$$

$$\mathrm{r_3 q_2 - r_2 q_3 = r_3(q_2} + \lambda \mathrm{r_2)} \tag{2.19}$$

Equation (2.10) can be rearranged as:

$$\mathbf{Q} = \mathbf{q} + \lambda \mathbf{r} \tag{2.20}$$

Substitute equation (2.20) into equation (2.18) and (2.19):

$$\mathrm{r_3 q_1 - r_1 q_3 = r_3 Q_1} \tag{2.21}$$

$$\mathrm{r_3 q_2 - r_2 q_3 = r_3 Q_2} \tag{2.22}$$

$$r_1\left[\frac{\partial u_1}{\partial x_1}-\frac{\partial u_3}{\partial x_3}\right] + r_2\frac{\partial u_1}{\partial x_2}+r_3\frac{\partial u_1}{\partial x_3}-\frac{{r_1}^2}{r_3}\frac{\partial u_3}{\partial x_1}-\frac{r_2 r_1}{r_3}\frac{\partial u_3}{\partial x_2} = Q_1 \tag{2.23}$$

$$r_2\left[\frac{\partial u_2}{\partial x_2}-\frac{\partial u_3}{\partial x_3}\right] + r_1\frac{\partial u_2}{\partial x_1}+r_3\frac{\partial u_2}{\partial x_3}-\frac{{r_2}^2}{r_3}\frac{\partial u_3}{\partial x_2}-\frac{r_2 r_1}{r_3}\frac{\partial u_3}{\partial x_1} = Q_2 \tag{2.24}$$

Equations (2.23) and (2.24) can be written in matrix form as following:

$$\begin{pmatrix} r_1 & r_2 & r_3 & 0 & 0 & 0 & -\frac{{r_1}^2}{r_3} & -\frac{r_2 r_1}{r_3} \\ 0 & 0 & 0 & r_1 & r_2 & r_3 & -\frac{r_2 r_1}{r_3} & -\frac{{r_2}^2}{r_3} \end{pmatrix} \begin{pmatrix} \left[\frac{\partial u_1}{\partial x_1}-\frac{\partial u_3}{\partial x_3}\right] \\ \frac{\partial u_1}{\partial x_2} \\ \frac{\partial u_1}{\partial x_3} \\ \frac{\partial u_2}{\partial x_1} \\ \left[\frac{\partial u_2}{\partial x_2}-\frac{\partial u_3}{\partial x_3}\right] \\ \frac{\partial u_2}{\partial x_3} \\ \frac{\partial u_3}{\partial x_1} \\ \frac{\partial u_3}{\partial x_2} \end{pmatrix} = \begin{pmatrix} Q_1 \\ Q_2 \end{pmatrix} \tag{2.25}$$

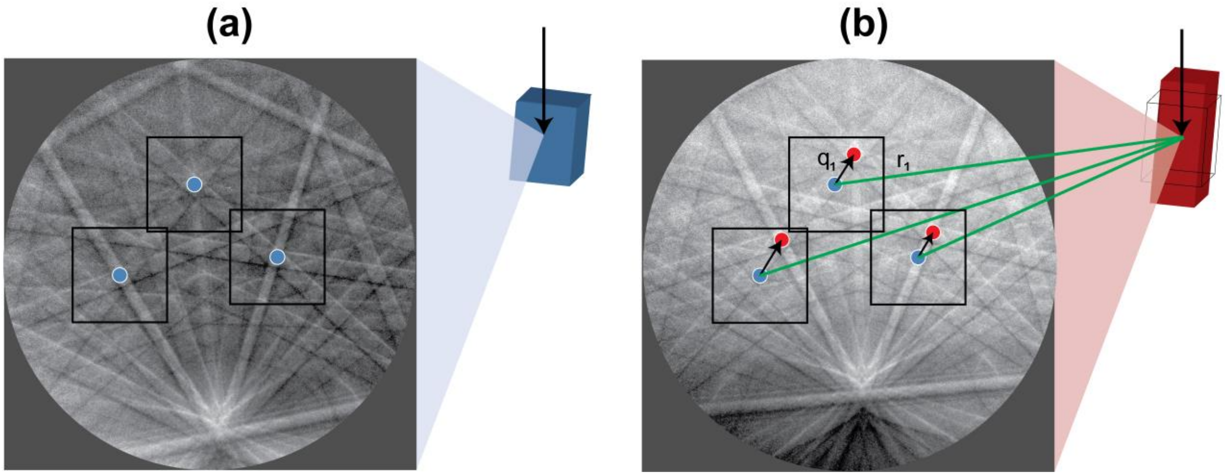

Figure 2.7 Schematic of the pattern intensity shifts in three low indexed zone axes between a) an elastically strain-free, and b) elastically strained crystal. Here unrealistically high shifts are shown in order to understand the process.

In this equation, the left part (**r**) is the vector from source point to center of subset on phosphor screen (as is shown in Figure 2.7) and is only related with calibration parameter and the position of subset; therefore, it is constant for each subset once the pattern center is known. The part to the right of the equation, Q_i, is the pattern shift for each subset that can be measured. The middle part contains 8 unknowns, therefore once four or more subsets are measured, values of $\left[\frac{\partial u_1}{\partial x_1} - \frac{\partial u_3}{\partial x_3}\right], \frac{\partial u_1}{\partial x_2}, \frac{\partial u_1}{\partial x_3}, \frac{\partial u_2}{\partial x_1}, \left[\frac{\partial u_2}{\partial x_2} - \frac{\partial u_3}{\partial x_3}\right], \frac{\partial u_2}{\partial x_3}, \frac{\partial u_3}{\partial x_1}, \frac{\partial u_3}{\partial x_2}$ can be determined. Normal components of the displacement gradient tensor (Equation 2.8) can be calculated by assuming the normal stress perpendicular to sample surface is zero and Hooke's law to write the stress in terms of strains and elastic constants, then an additional equation can be generated, which combined with the calculated values of $\left[\frac{\partial u_1}{\partial x_1} - \frac{\partial u_3}{\partial x_3}\right]$ and $\left[\frac{\partial u_2}{\partial x_2} - \frac{\partial u_3}{\partial x_3}\right]$ allows the normal components to be calculated. The above procedure allows the calculation of the displacement gradient tensor. This tensor can be split into symmetric and asymmetric parts that represent elastic strains ε_{ij} and rotations w_{ij} respectively:

$$\varepsilon_{ii} = \frac{\partial u_i}{\partial x_i} \tag{2.26}$$

$$\varepsilon_{ij} = \frac{1}{2}\left(\frac{\partial u_i}{\partial x_j} + \frac{\partial u_j}{\partial x_i}\right) \tag{2.27}$$

$$w_{ij} = \frac{1}{2}\left(\frac{\partial u_i}{\partial x_j} - \frac{\partial u_j}{\partial x_i}\right) \tag{2.28}$$

2.3.3 Measuring Small Pattern Shift in HR-EBSD

In order to accurately determine pattern shift using the cross correlation-based method, the below steps should be followed. The below instruction is adopted from [28].

First, a series of high-quality EBSD patterns must be obtained; the detailed technical parameters can be found in [40-43]. To calculate the pattern shifts, the Kikuchi pattern of the highest quality in the series was selected as the reference and compared with other Kikuchi patterns in the series. First, each pattern is divided into several regions of interest (ROI). It was previously reported that 20 ROIs decrease the standard deviation of displacement gradient tensor to 10^{-4} [41]. A typical ROI of 256x256 pixels for a 1000x1000 pixel Kikuchi pattern was recommended in the research by Wilkinson *et al*. [41, 42].

For each individual ROI, the mean intensity is calculated and then subtracted from every pixel. The resulting intensity is then multiplied by a weighting function:

$$f(x, y) = \cos\left(\frac{\pi x}{256}\right)\cos\left(\frac{\pi y}{256}\right) \tag{2.29}$$

where (x, y) is the position of the pixel relative to the ROI center.

This weighting function brings the intensity at the edge of the ROI to zero, as shown in Figure 2.9.

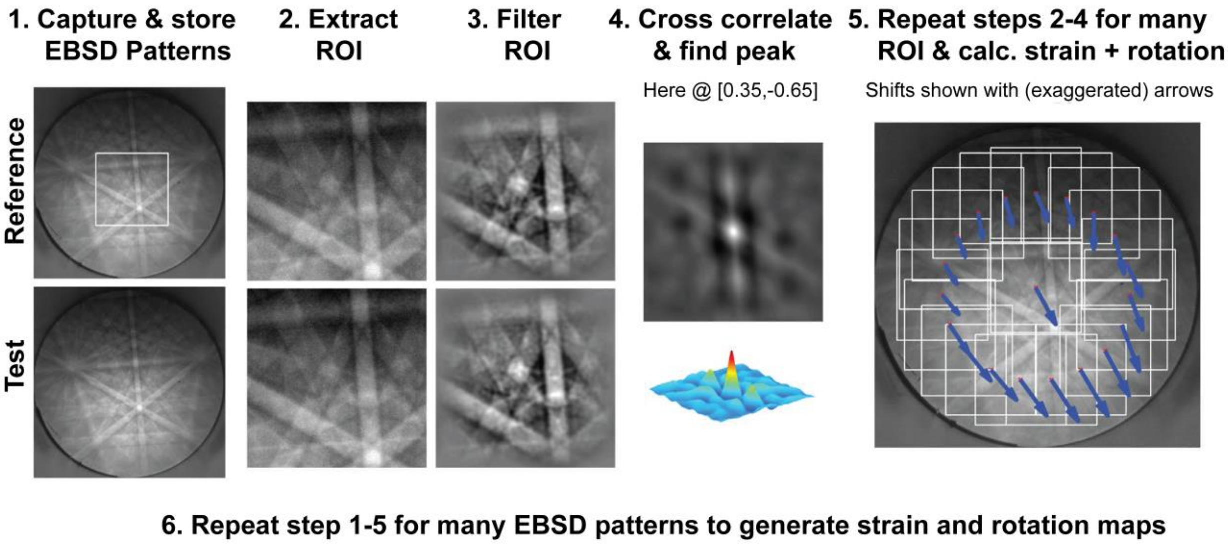

Figure 2.8 Schematic of HR-EBSD analysis process [47].

The diffraction patterns converted to the Fourier domain to be more computationally efficient in calculating the cross-correlation function at this ROI size. In the Fourier domain, the pattern is filtered by a high pass frequency filter to remove the low-frequency elements and a low pass frequency filter to eliminate the high-frequency fluctuations associated with noise of the CCD readout (Figure 2.8).

The normalized cross-correlation function (χ) can be assessed by comparing the Kikuchi patterns in the Fourier domain:

$$X^2 = \frac{\sum \mathrm{FG}}{\sqrt[2]{\sum \mathrm{F}^2 \sum \mathrm{G}^2}} \tag{2.30}$$

where F is the FFT of the reference and G is the FFT of the test ROI. The cross-correlation function is represented as an intensity distribution, where the intensity at each point means the degree of correlation.

2.4 References:

1. Chapuis, A. and J.H. Driver, *Temperature dependency of slip and twinning in plane strain compressed magnesium single crystals.* Acta Materialia, 2011. **59**(5): p. 1986-1994.
2. Yu, Q., *Size-related Mechanical Properties of Pure Magnesium*. 2012: University of California, Berkeley.
3. Chino, Y., et al., *Mechanical anisotropy due to twinning in an extruded AZ31 Mg alloy.* Materials Science and Engineering: A, 2008. **485**(1-2): p. 311-317.
4. Hall, E., *Proc. Phys. Soc.* Series B, 1951. **64**: p. 747.
5. Petch, N., *The cleavage strength of polycrystals.* Journal of the Iron and Steel Institute, 1953. **174**: p. 25-28.
6. Armstrong, R.W., *60 years of Hall-Petch: past to present nano-scale connections.* Materials Transactions, 2014. **55**(1): p. 2-12.
7. Armstrong, R.W., *Hall–Petch k dependencies in nanopolycrystals.* Emerging Materials Research, 2014. **3**(6): p. 246-251.
8. Hirth, J.P. and J. Lothe, *Theory of dislocations.* 1982.
9. Muskhelishvili, N.I. and J.R.M. Radok, *Singular integral equations: boundary problems of function theory and their application to mathematical physics*. 2008: Courier Corporation.
10. Tricomi, F.G., *On the finite Hilbert transformation.* The Quarterly Journal of Mathematics, 1951. **2**(1): p. 199-211.
11. Weng, G., *A micromechanical theory of grain-size dependence in metal plasticity.* Journal of the Mechanics and Physics of Solids, 1983. **31**(3): p. 193-203.
12. Armstrong, R., et al., *The plastic deformation of polycrystalline aggregates.* The Philosophical Magazine: A Journal of Theoretical Experimental and Applied Physics, 1962. **7**(73): p. 45-58.
13. Yu, H., et al., *Hall-Petch relationship in Mg alloys: a review.* Journal of Materials Science & Technology, 2018. **34**(2): p. 248-256.
14. Guo, L., Z. Chen, and L. Gao, *Effects of grain size, texture and twinning on mechanical properties and work-hardening behavior of AZ31 magnesium alloys.* Materials Science and Engineering: A, 2011. **528**(29-30): p. 8537-8545.
15. Yuan, W., et al., *Influence of grain size and texture on Hall–Petch relationship for a magnesium alloy.* Scripta Materialia, 2011. **65**(11): p. 994-997.
16. Yu, H., et al., *The mechanism for the high dependence of the Hall-Petch slope for twinning/slip on texture in Mg alloys.* Acta Materialia, 2017. **128**: p. 313-326.
17. Tong, L., et al., *Reducing the tension–compression yield asymmetry of extruded Mg–Zn–Ca alloy via equal channel angular pressing.* Journal of Magnesium and Alloys, 2015. **3**(4): p. 302-308.
18. Doiphode, R., et al., *Grain growth in calibre rolled Mg–3Al–1Zn alloy and its effect on hardness.* Journal of Magnesium and Alloys, 2015. **3**(4): p. 322-329.
19. Wang, Y. and H. Choo, *Influence of texture on Hall–Petch relationships in an Mg alloy.* Acta Materialia, 2014. **81**: p. 83-97.

20. Chino, Y., et al., *Mechanical properties and press formability at room temperature of AZ31 Mg alloy processed by single roller drive rolling.* Materials Transactions, 2002. **43**(10): p. 2554-2560.
21. Del Valle, J., F. Carreño, and O.A. Ruano, *Influence of texture and grain size on work hardening and ductility in magnesium-based alloys processed by ECAP and rolling.* Acta Materialia, 2006. **54**(16): p. 4247-4259.
22. Shaw, L.L., A.L. Ortiz, and J.C. Villegas, *Hall–Petch relationship in a nanotwinned nickel alloy.* Scripta Materialia, 2008. **58**(11): p. 951-954.
23. Jain, A., et al., *Grain size effects on the tensile properties and deformation mechanisms of a magnesium alloy, AZ31B, sheet.* Materials Science and Engineering: A, 2008. **486**(1-2): p. 545-555.
24. Barnett, M., et al., *Influence of grain size on the compressive deformation of wrought Mg–3Al–1Zn.* Acta materialia, 2004. **52**(17): p. 5093-5103.
25. Chang, L., et al., *Grain size and texture effect on compression behavior of hot-extruded Mg–3Al–1Zn alloys at room temperature.* Materials characterization, 2009. **60**(9): p. 991-994.
26. Kim, D., et al., *Experimental investigation into effect of annealing treatment on springback of magnesium alloy sheets.* Materials Research Innovations, 2011. **15**(sup1): p. s183-s186.
27. Somekawa, H. and T. Mukai, *Hall–Petch relation for deformation twinning in solid solution magnesium alloys.* Materials Science and Engineering: A, 2013. **561**: p. 378-385.
28. Guo, Y., *Exploration of microstructure related deformation gradients in commercial purity titanium*. 2015, The University of Oxford: The University of Oxford.
29. Yoo, M., *Slip, twinning, and fracture in hexagonal close-packed metals.* Metallurgical transactions A, 1981. **12**(3): p. 409-418.
30. Sugiura, L., *Comparison of degradation caused by dislocation motion in compound semiconductor light-emitting devices.* Applied physics letters, 1997. **70**(10): p. 1317-1319.
31. Bowen, D. and B. Tanner, *A method for the accurate comparison of lattice parameters.* Journal of applied crystallography, 1995. **28**(6): p. 753-760.
32. Stone, H., et al., *Comparison of three different techniques for measuring the residual stresses in an electron beam-welded plate of WASPALOY.* Metallurgical and Materials Transactions A, 1999. **30**(7): p. 1797-1808.
33. Sabate, N., et al., *Measurement of residual stress by slot milling with focused ion-beam equipment.* Journal of Micromechanics and Microengineering, 2006. **16**(2): p. 254.
34. Burton, N., et al., *Strain and microstructure variation in grains of CVD diamond film.* Diamond and related materials, 1995. **4**(10): p. 1222-1234.
35. Dietrich, B., et al., *Raman investigations of elastic strain relief in Si1− x Ge x layers on patterned silicon substrate.* Journal of applied physics, 1993. **74**(12): p. 7223-7227.
36. Wilkinson, A.J., D.J. Dingley, and G. Meaden, *Strain mapping using electron backscatter diffraction*, in *Electron Backscatter Diffraction in Materials Science*. 2009, Springer. p. 231-249.

37. Quinta da Fonseca, J., P. Mummery, and P. Withers, *Full-field strain mapping by optical correlation of micrographs acquired during deformation.* Journal of microscopy, 2005. **218**(1): p. 9-21.
38. Maier, H., et al., *On the unique evaluation of local lattice parameters by convergent-beam electron diffraction.* Philosophical Magazine A, 1996. **74**(1): p. 23-43.
39. Troost, K., P. Van der Sluis, and D. Gravesteijn, *Microscale elastic-strain determination by backscatter Kikuchi diffraction in the scanning electron microscope.* Applied Physics Letters, 1993. **62**(10): p. 1110-1112.
40. Wilkinson, A.J., *Measurement of elastic strains and small lattice rotations using electron back scatter diffraction.* Ultramicroscopy, 1996. **62**(4): p. 237-247.
41. Wilkinson, A.J., G. Meaden, and D.J. Dingley, *High resolution mapping of strains and rotations using electron backscatter diffraction.* Materials Science and Technology, 2006. **22**(11): p. 1271-1278.
42. Wilkinson, A.J., G. Meaden, and D.J. Dingley, *High-resolution elastic strain measurement from electron backscatter diffraction patterns: new levels of sensitivity.* Ultramicroscopy, 2006. **106**(4-5): p. 307-313.
43. Dingley, D.J., et al., *Elastic strain tensor measurement using electron backscatter diffraction in the SEM.* Journal of electron microscopy, 2010. **59**(S1): p. S155-S163.
44. Wright, S.I., M.M. Nowell, and D.P. Field, *A review of strain analysis using electron backscatter diffraction.* Microscopy and microanalysis, 2011. **17**(3): p. 316-329.
45. Britton, T. and A. Wilkinson, *Measurement of residual elastic strain and lattice rotations with high resolution electron backscatter diffraction.* Ultramicroscopy, 2011. **111**(8): p. 1395-1404.
46. Britton, T. and A.J. Wilkinson, *High resolution electron backscatter diffraction measurements of elastic strain variations in the presence of larger lattice rotations.* Ultramicroscopy, 2012. **114**: p. 82-95.
47. Britton, T.B., et al., *Probing deformation and revealing microstructural mechanisms with cross-correlation-based, high-resolution electron backscatter diffraction.* Jom, 2013. **65**(9): p. 1245-1253.

Chapter 3: Quantitative Study of the Effect of Grain Boundary Parameters on the Slip System Level Hall-Petch Slope for Basal Slip System in Mg-4l

3.1 Abstract

Several theoretical studies have reported that the geometry and structure of grain boundaries in polycrystalline materials could impose a significant effect on the Hall-Petch slope. However, experimental observations are primarily limited by the ability of the techniques to accurately quantify the grain boundary strength and validate these theoretical models. Using high-resolution electron backscatter diffraction (HR-EBSD), the local stress tensor ahead of a slip band blocked by a grain boundary was quantified and coupled with a continuum dislocation pile-up model to assess the barrier strength of specific grain boundaries to specific slip systems, referred to as micro-Hall-Petch coefficient. For basal slip system in a deformed Mg-4Al alloy, the micro-Hall-Petch coefficient $\left(k_{\mu}^{basal}\right)$ varied significantly, from 0.054 to 0.184 $\mathrm{MPa}{-}\mathrm{m}^{\mathbf{1/2}}$ for nine different grain boundaries. These results were correlated with geometric descriptors of the respective grain boundaries, with three-dimensional GB profile additionally measured via focused ion beam milling. It was found that the angle between the two slip plane traces on the grain boundary plane was the most sensitive parameter affecting k_{μ}^{basal}, followed by the angle between the slip directions. A functional form for calculation of k_{μ}^{basal} depending on these two angles is proposed to augment crystal plasticity constitutive models with slip resistance dependent on some measure of the grain size. The method allows a new pathway to calibrate grain size strengthening parameters in crystal plasticity models, allowing further computational investigations of the interrelationship between texture, grain morphology, and the Hall Petch effect.

3.2 Introduction

Magnesium (Mg) alloys, owing to their low density, which is 23% that of steel and 66% that of aluminum [1, 2], continue to receive significant attention for weight-saving applications. However, the widespread industrial application of Mg alloys is hindered by their low strength and limited room temperature formability. Several strategies have been proposed to improve the strength and formability of Mg alloys include solid solution alloying [3-5], precipitate hardening [6-8], grain refinement [9, 10], and basal texture weakening [11-13]. Among these techniques, grain refinement is one of the most common techniques used to improve the yield strength of Mg alloys according to the well-known Hall-Petch equation [14-17], which connects the yield strength of the bulk material (σ_y) to its average grain size (D): $\sigma_y = \sigma_0 + \frac{K}{\sqrt{D}}$ where σ_0 is the friction stress and K is the macroscopic Hall-Petch coefficient (HPC), which represents the collective strengthening effect of all the grain boundaries in the polycrystal. One of the most common mechanisms that the Hall-Petch effect is attributed to is the strength needed for a dislocation pile-up to overcome the grain boundary (treated as an obstacle) to effect slip transmission. Extensive research into slip transmission phenomena in polycrystalline materials has unraveled its complexity via dependence on a multitude of local factors such as GB energy [18, 19], atomic structure of GB [20], residual Burgers vectors [21-24], resolved shear stress on each slip system [24-26] and a combination of these factors [27-33]. While these are important to the eventual understanding of their effect on the HPC, an attempt to analyze the effect of crystallographic properties on the HPC forms an initial step to tackle this problem.

Many studies in the literature have reported that the HPC for face-centered cubic (FCC) and body-centered cubic (BCC) materials are less sensitive to crystallographic texture [34-38] as compared to hexagonal close-packed (HCP) metals such as Mg and its alloys [10, 39-41]. Texture variations can alter dominant deformation modes, on which the grain boundaries can have a different effect, which in turn can result in different values of the HPC [41]. Accordingly, various efforts have been made to estimate the HPC for a wide variety of alloys by considering the effect of texture, intergranular relationships, and a dependence of the slip system resistance on grain size [9, 42-44]. To reflect these changes occurring at the microscale, the Hall-Petch relationship is specialized to the slip system level as $\tau^{\alpha} = \tau_0^{\alpha} + k_{\mu}^{\alpha}.L^{-1/2}$, where τ^{α} is the critical resolved shear stress of slip system α, τ_0^{α} is the critical resolved shear stress of slip system α of a theoretically infinite single crystal, k_{μ}^{α} the Hall-Petch coefficient of the slip system α (henceforth referred to as micro-Hall-Petch coefficient) and L is the slip system-level grain size [45-47]. Wang *et al*. [41] and Singh *et al*. [48] proposed an approach to estimate the k_{μ}^{α} using macroscopic tensile test data of Mg alloy samples with four different average grain sizes. They calculated the resolved shear stress of the dominant slip system at yielding by dividing the yield strength of the material by the average Schmid factor values of that specific slip system. The micro-Hall-Petch coefficient is then obtained from the slope of the linear regression model which assumes a linear relationship between the resolved shear stress data and the inverse square root of the average grain size. While their studies provide a rough estimate of k_{μ}^{α}, their approach does not consider the structure and geometry of the grain boundaries.

Several theoretical models have reported that the geometry and structure of the grain boundary (GB) plays an important role in impeding slip transmission within the material and hence contributing to the strength of polycrystalline materials [18, 20, 28]. However, experimental observations to accurately quantify the grain boundary strength and validate these theoretical models are primarily limited by the ability of experimental techniques to measure the stress field ahead of a slip band blocked by a grain boundary.

Recently, the development of high-resolution electron backscatter diffraction (HR-EBSD) technique provides the possibility of measuring the stress components locally in materials with the spatial resolution on the order of 100 nm [49]. Using this technique, the local stress concentration, ahead of dislocation pile-ups, has been successfully examined in commercial purity titanium [50-52], irradiated steel [53, 54], and unalloyed Mg [55].

In this work, HR-EBSD measurements are analyzed using a continuum dislocation pile-up model to calculate the micro-Hall-Petch coefficient of the basal slip system for nine different grain boundaries in a deformed Mg-4Al sample. HR-EBSD is a surface measurement technique, while grain boundary descriptors such as GB tilt and twist angles are three-dimensional quantities not directly accessible through HR-EBSD. The novelty of this current work is the use of the focused ion beam (FIB) milling to obtain additional insights on the three-dimensional GB geometry for all nine grain boundaries. Based on the combined experimental data and model, different functional expressions are examined, which involve three-dimensional geometric descriptors of the respective GBs, and a functional form for the micro-Hall-Petch coefficient of the basal system depending on these descriptors is proposed. Their possible usage in crystal plasticity constitutive models is explored, and some outstanding issues are addressed.

3.3 Methods

The author conducted the computational work in collaboration with Prof. Veera Sundararaghavan and his student Aaditya Lakshmanan.

3.3.1 Materials and experimental procedures

The alloy selected for this work was extruded Mg-4Al (wt.%) bar produced by CanmetMaterials [Hamilton, Ontario, Canada]. The as-extruded microstructure and texture of the material are shown in Figure 3.1. The microstructure contains equiaxed grains with an average grain diameter of 50 µm. Tensile test samples with the gauge dimensions of 10 mm × 2 mm × 2 mm were cut using electrical discharge machining (EDM). Prior to mechanical testing, the samples were mechanically polished using standard metallographic techniques, with the final step using 0.05 µm polycrystalline diamond solution. The samples were then etched using an acetic-nitric solution (10 mL nitric acid, 5 mL acetic acid, 20 mL water, and 60 mL ethanol) for 3 seconds to reveal the GB structures under scanning electron microscopy (SEM).

The as-extruded microstructure and texture were measured using EBSD, as shown in Figure 3.1a and Figure 3.1b. The samples were then subjected to tensile loading parallel to the extrusion direction (shown in Figure 3.1a) to produce slip bands. SEM imaging was then used to find and document the position of the blocked slip band-GB interactions. Two examples of such interactions are shown in Figure 3.1c, and Figure 3.1d, with slip bands, blocked at grain boundaries without evidence of slip transfer to the adjacent grain. Specific grain boundaries were chosen for this work based on the existence of blocked slip bands at GBs and various misorientation angles. Table 3.1 summarizes the GB misorientation and the corresponding rotation axis determined by EBSD of the selected GBs.

EBSD scans with the average size of 10 µm × 30 µm with a square grid and 200 nm step size, were captured near the slip band-GB interaction regions using FEI Quanta 650 ESEM equipped with an integrated Oxford AZtec EDS and EBSD system. The Kikuchi patterns were obtained at each step in the scan with a resolution of 1024 × 1024 pixels and saved in the TIFF image format with 12-bit depth.

CrossCourt4 (CC4) software package developed by BLG Vantage [56] was used for analyzing the Kikuchi patterns. For each Kikuchi pattern, 50 regions of interest (ROIs) with the

256 × 256 pixels in size were used. The ROIs were compared with the corresponding ROIs of the low-stress reference pattern of each grain using the cross-correlation method developed by Wilkinson *et al*. [49] to calculate the full stress tensor fields. The remapping algorithm developed by Britton and Wilkinson [57] was used during CC4 analysis to reduce the effect of minor lattice rotation on the assessment of stress tensor.

After the HR-EBSD measurement was completed, focused ion beam (FIB) milling was performed using a dual-beam FEI Helios Nanolab 650 microscope to lift out a lamella perpendicular to the GB line and the surface normal, to discover the GB tilt relative to the surface normal.

Table 3.1 List of GB misorientation angles and the corresponding rotation axis determined by EBSD of the selected GB-slip band interactions zones.

Grain Boundary ID	**Misorientation (°)**	**Rotation Axis**
1	73.70	$[\bar{4}\ 8\ \bar{4}\ \bar{3}]$
2	54.89	$[1\ 0\ \bar{1}\ 0]$
3	38.30	$[\bar{5}\ 1\ 4\ \bar{3}]$
4	39.21	$[5\ \bar{1}\ \bar{4}\ \bar{3}]$
5	26.65	$[\bar{7}\ 2\ 5\ 3]$
6	55.98	$[4\ \bar{5}\ 1\ 3]$
7	47.91	$[\bar{7}\ 2\ 5\ 0]$
8	89.01	$[\bar{7}\ 2\ 5\ 0]$
9	89.82	$[\bar{7}\ 2\ 5\ \bar{3}]$

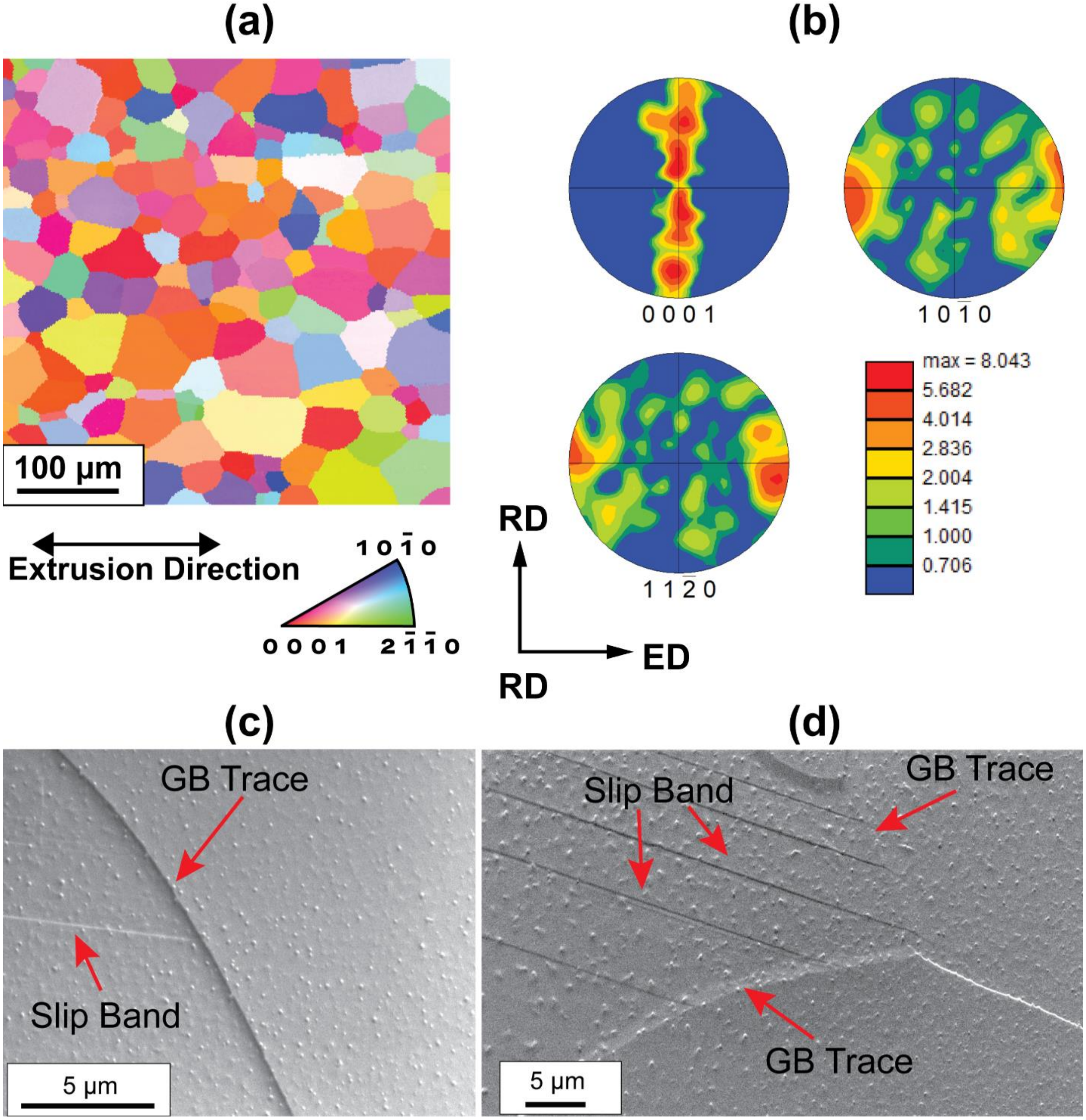

Figure 3.1 (a) Representative microstructure and (b) pole figure of extruded Mg-4Al (wt.%) used in this study. The microstructure contains equiaxed grains with an average grain diameter of 50 μm. RD: Radial Direction; ED: Extrusion Direction (c), (d) Two examples of   Two examples of blocked slip bands at grain boundaries which blocked slip bands in one grain and no-slip transfer or slip band formation in the adjacent grain, is observed.

3.3.2 Numerical Methods

While the blocked slip band in one grain is observed, it is also important to identify the most likely slip system to be activated in the adjacent grain where no slip bands are seen. The primary slip system in the adjacent grain that is likely to get activated is affected by factors such as slip orientation relative to loading and load redistribution due to the grain neighborhood. Crystal plasticity finite element (CPFE) simulations allow a detailed computational understanding of these factors. The single crystal constitutive model for CPFE was first calibrated by comparing the polycrystal stress-strain response with the experimental stress-strain curves. These parameters were then used to simulate the different GB neighborhoods to identify the likely primary slip system in the grains sharing the respective grain boundary of interest. All the crystal plasticity simulations were carried out using PRISMS-Plasticity [58, 59], an open-source 3-D CPFE framework based on a fully implicit implementation of an elastoplastic single crystal model. Crystallographic slip, twinning, and re-orientation of crystals were assumed to be the primary mechanisms of plastic deformation. For a crystal with N slip/twin systems the slip resistance offered by slip system α at time t, $s^{\alpha}(t)$, depends on the plastic slip rates via the hardening law:

$$\dot{s}^{\alpha}(t) = \sum_{\beta=1}^{N} h^{\alpha\beta}\left|\dot{\gamma}^{\beta}\right|, \quad \text{where } \dot{s}^{\alpha}(0) = s_0^{\alpha} \tag{3.1}$$

$$h^{\alpha\beta} = h_0^{\beta}\left(q + (1-q)\,\delta_{\alpha\beta}\right)\left(1 - \frac{s^{\beta}(t)}{s_{sat}^{\beta}}\right), \quad \text{(no sum on } \beta\text{)} \tag{3.2}$$

where the latent hardening is included through the coefficient q which is chosen to be 1, and $\delta_{\alpha\beta}$ denotes the N x N identity matrix. s_0^{α} denotes the initial slip resistance of slip system α, while h_0^{β} and s_{sat}^{β} signify the hardening modulus and saturation stress, respectively, for slip system β . These three parameters were calibrated for each slip system such that the CPFE model predicts the experimental stress-strain response in the plastic regime satisfactorily. Additional details of the model, including elastoplastic decomposition, flow rule and constitutive update algorithm, are detailed in [60].

For the calibration step, the polycrystal idealized as an 8 × 8 × 8 voxelated RVE was constructed, where each voxel was assigned a distinct orientation. Orientations were sampled from an EBSD map of a microstructure (Figure 3.1a and Figure 3.1b) with 856 grains to ensure that the texture was satisfactorily represented in the idealized polycrystal (Figure 3.2a). This microstructure was subject to axisymmetric tension along the y direction up to approximately 3.5% strain. Figure 3.2b depicts the comparison of stress-strain response from the simulation to the experiment at the end of calibration. The list of constitutive model parameters post-calibration is included in Table 3.2.

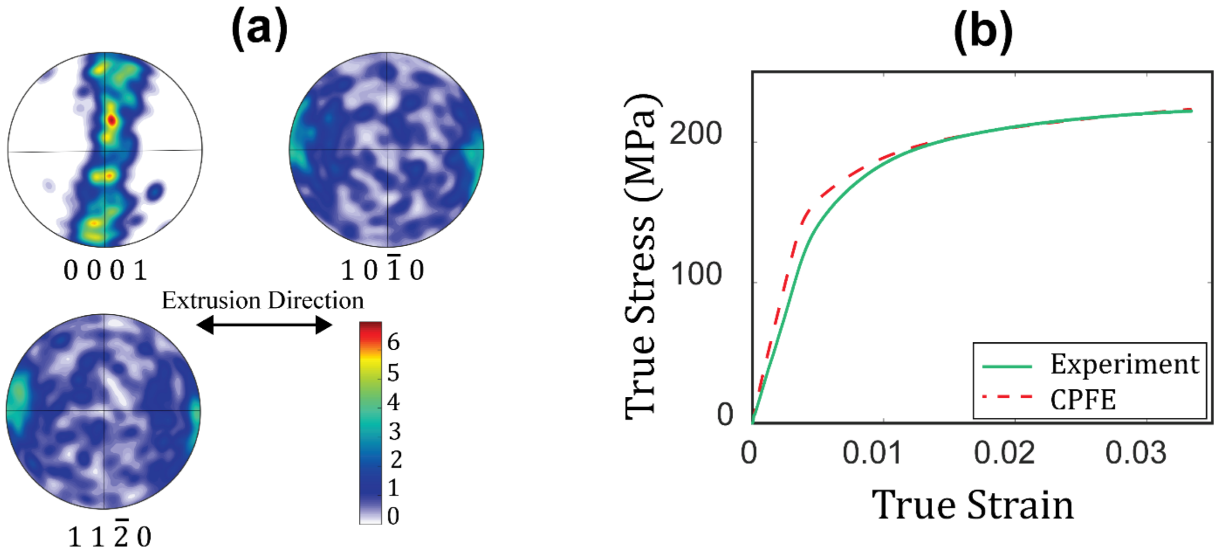

Figure 3.2 (a) Pole figures of the polycrystalline RVE represented as an 8x8x8 voxelated grid with one orientation per voxel, (b) Comparison of simulated stress-strain response with experiment resulting in the calibrated parameters in Table 3.2.

Table 3.2 Initial slip resistance and hardening parameters post-calibration

Mode	s_0^α	h_0^α	s_{sat}^α
Basal <a>	6.0	76.0	120.0
Prismatic <a>	78.0	163.0	150.0
Pyramidal <a>	78.0	163.0	150.0
Pyramidal <c + a>	140.0	187.0	150.0
Twin <c + a>	13.0	116.0	100.0

3.4 Results

3.4.1 Stress concentration calculation ahead of blocked slip bands at grain boundaries

Slip bands blocked at grain boundaries were identified using SEM (two examples of such regions are shown in Figure 3.1c and Figure 3.1d), and 10 μm × 30 μm regions around the interaction area were selected for HR-EBSD scans as shown in Figure 3.3a. For each grain, a reference point for the measurement of stress was selected far away from the grain boundaries, where stress was assumed to be low relative to the GB vicinity. An example of a reference pattern site marked with a yellow cross is shown in Figure 3.3a, and the corresponding high-quality image Kikuchi pattern is shown in Figure 3.3b. For each Kikuchi pattern, 50 ROIs were used and compared with the corresponding ROIs of the reference pattern to calculate the distortion tensor and from that the full stress tensor (more details provided in section 3.2.1). The stress components were obtained relative to the $x_1x_2x_3$ reference frame (Figure 3.4a), which we refer to as the sample frame. An example of the full stress tensor as the output of HR-EBSD analysis is shown in Figure 3.3c. The stress concentration induced by slip bands blocked at the GB can be clearly observed from the σ_{11}, σ_{12} and σ_{23} stress components. σ_{33} is negligible because the sample surface was unconstrained.

To calculate the shear stress resolved onto the slip system corresponding to the slip band, the slip system was first determined (explained in section 3.2.2), and then the stress tensor was rotated to another axis system, $\mathrm{x}_1^\mathrm{r}\mathrm{x}_2^\mathrm{r}\mathrm{x}_3^\mathrm{r}$ as shown in Figure 3.4a. In this axis system, x_1^r is the direction of the slip plane normal while x_3^r and x_2^r are in the direction of the Burgers vector of the determined active slip system in the deformed grain (upper grain) and the direction perpendicular to it on the slip plane, respectively. Figure 3.4b shows τ_{13}^r component of the rotated tensor, which represents the resolved shear stress of interest on the slip system corresponding to the slip band of the deformed grain.

In our previous work [55], the slip band blocked at the GB was interpreted as a pile-up of dislocations, which was then modeled using a 1D double-ended continuum dislocation pile-up. The theoretical model is briefly reviewed first.

In the 1D double-ended continuum dislocation pile-up model, the equilibrium dislocation distribution is obtained for the case when a spatially constant resolved shear stress is applied throughout a grain of size L. The balance between the applied stress and the dislocation-dislocation interactions results in an equilibrium dislocation distribution from which the stress field ahead of the pile-up [61] is obtained as

$$\tau_p(X) = \tau \,. \left[\frac{X + \frac{L}{2}}{\sqrt{\left(X + \frac{L}{2}\right)^2 - \left(\frac{L}{2}\right)^2}} - 1 \right] \tag{3.3}$$

where $\tau_p(X)$ represents the resolved shear stress ahead of the pile-up, L is the grain size, and X is the coordinate measured from the grain boundary. Considering a specific slip system of interest indexed as α, substituting the phenomenological micro-Hall-Petch equation [34, 45], $\tau = \tau^{\alpha} = \tau_0^{\alpha} + \frac{k_{\mu}^{\alpha}}{\sqrt{L}}$ into Equation 3.4 yields

$$\tau_p(X) = \left(\tau_0^{\alpha} + \frac{k_{\mu}^{\alpha}}{\sqrt{L}}\right)\left[\frac{X + \frac{L}{2}}{\sqrt{\left(X + \frac{L}{2}\right)^2 - \left(\frac{L}{2}\right)^2}} - 1\right] \tag{3.4}$$

where τ_0^{α} is the critical resolved shear stress of slip system α of a theoretically infinite single crystal, k_{μ}^{α} the micro-Hall-Petch coefficient of the slip system α, L is the slip system-level grain size, and X is the distance from the GB, as denoted in Figure 3.4b. The micro-Hall-Petch coefficients were computed for different GB types by fitting the experimentally measured stress field ahead of the pile-up (Figure 3.4b) to the calculation (Equation 3.4). It must be noted that using a 1D continuum dislocation pile-up model is an oversimplification of the actual physics, which is much more complicated. Additionally, the back-stress that might arise from GND distributions in the vicinity of the GB is not considered explicitly in the pile-up model. Their importance has been demonstrated in the context of large grained titanium [62] where correlations were drawn between GND content and geometric metrics of the GB. However, quantification of this back-stress for informing micromechanical models like the present pile-up model is yet to be performed. In the interest of drawing a simple analogy to a blocked slip band and obtaining first-order analytical expressions, we have resorted to the aforementioned model 1D continuum pile-up model without GND induced back-stress.

A line scan was taken along the slip direction of the deformed grain (upper grain) but continued to the lower grain, labeled by X direction in Figure 3.4b, to capture the stress profile ahead of the slip band pile up at the GB as shown in Figure 3.4c. This stress was then resolved onto the active slip system to yield the resolved shear stress profile ahead of the blocked slip band, which was fitted with Equation 3.3. The experimental data follow a similar trend as the dislocation pile-up model presented in Equation 3.3 (Figure 3.4c). The micro-Hall-Petch coefficient of the active slip system α, can be obtained by curve fitting the experimental stress profile with the continuum dislocation pile-up model. k_{μ}^{α} for all analyzed grain boundaries are measured and reported in Table 3.3. Since the active slip systems of the deformed grains in all different boundaries studied in this work were basal slip systems (Table 3.6), τ_{0}^{α} is computed by incorporating the effect of solid solution strengthening due to 4 wt. % Al [63] resulting in τ_{0}^{α} = 4.34 MPa. Accordingly, the calculated micro-Hall-Petch coefficient is denoted as k_{μ}^{basal}.

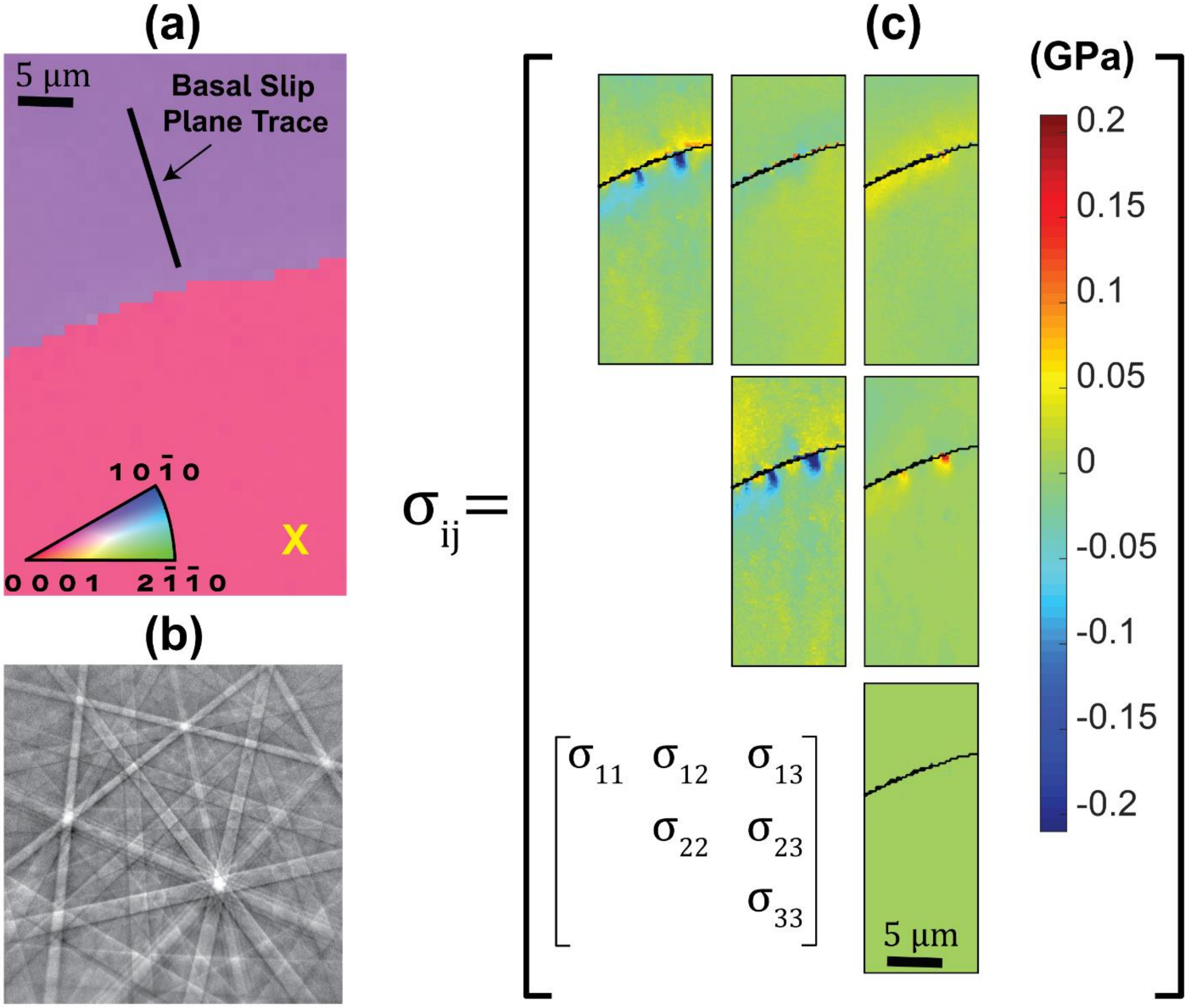

Figure 3.3 (a) An example of selected 10 μm × 30 μm regions around the slip band-GB interaction for HR-EBSD scans. (b) Kikuchi diffraction pattern of the reference point marked by a yellow cross in Figure 3.3a. (c) An example of HR-EBSD output which is a full stress tensor calculated in the sample frame. (For interpretation of the references to color in this figure legend, the reader is referred to the web version of this article.

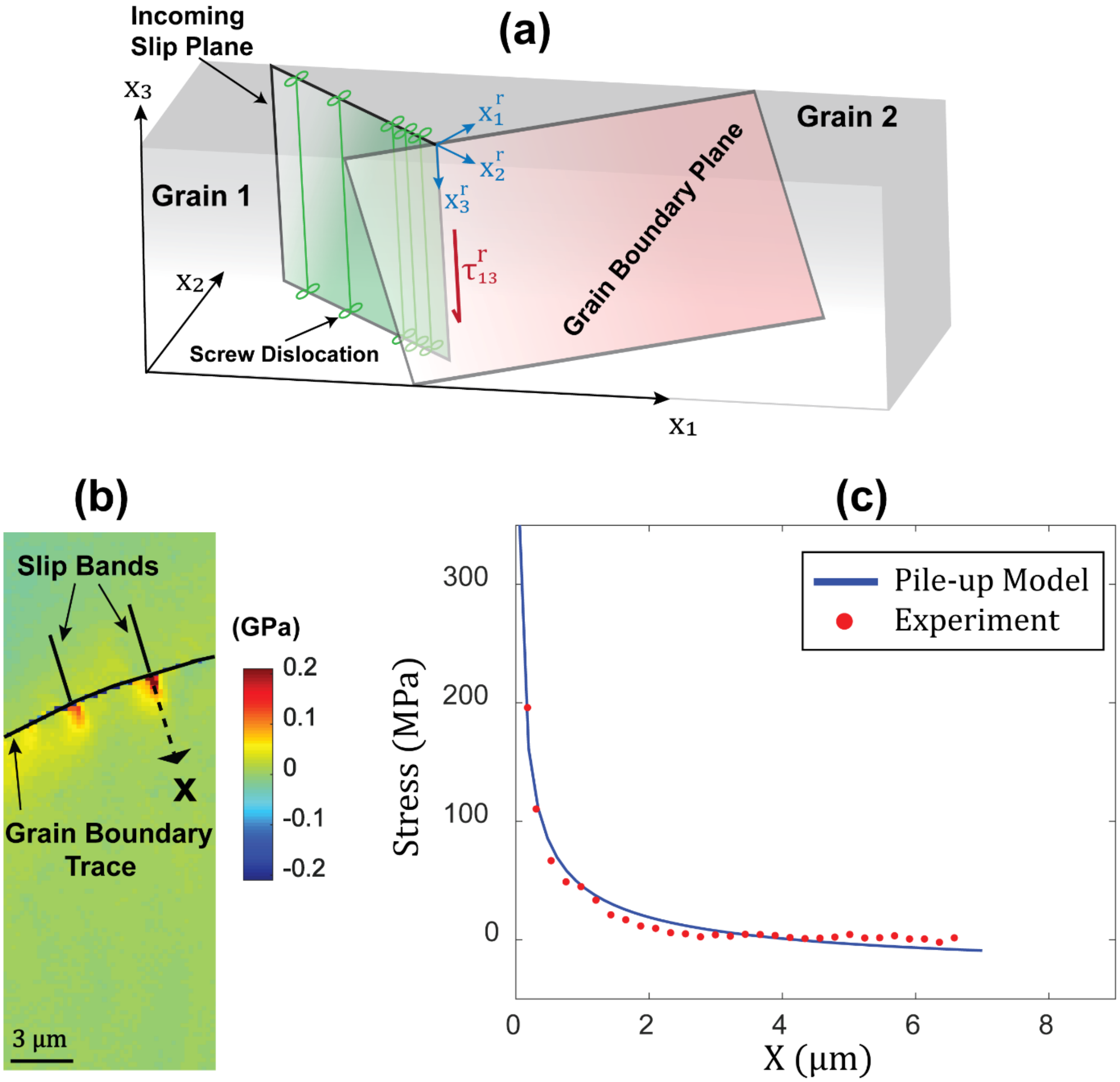

Figure 3.4 (a) Schematic of a dislocation pile-up at a GB. HR-EBSD is used to measure the stress in the sample frame $x_1x_2x_3$. To calculate the shear stress resolved onto the active slip system observed experimentally by the slip band (τ_{13}^r), the stress tensor was rotated into another axis system, $x_1^r x_2^r x_3^r$. (b) HR-EBSD map of resolved shear stress τ_{13}^r onto the active slip system in the upper grain. The stress concentration ahead of pile up at GB can be observed. The solid lines represent the position of the slip bands, and the dashed line with an arrowhead indicates the direction along which the stress profile shown in Figure 3.4c was extracted. (c) The resolved shear stress profile ahead of a slip band blocked by a GB with comparison to the continuum dislocation pile-up model to calculate the micro-Hall-Petch coefficient of each individual GB.

Table 3.3 Micro-Hall-Petch coefficient of the basal slip system for different grain boundaries

Grain boundary ID	1	2	3	4	5	6	7	8	9
Slip System Level Grain Size (μm)	48	55	27	8	65	21	50	60	48
k_{μ}^{basal} ($\mathbf{MPa.m^{1/2}}$)	0.164 ± 0.02	0.091 ± 0.01	0.149 ± 0.02	0.172 ± 0.02	0.054 ± 0.01	0.108 ± 0.01	0.070 ± 0.01	0.143 ± 0.01	0.184 ± 0.02

3.4.2 Understanding the effect of grain boundary on the micro-Hall-Petch Coefficient

The goal of this study is to first calculate the micro-Hall-Petch coefficient of various type of grain boundaries (section 3.3.1) and then correlate k_{μ}^{α} values with the quantitative geometrical expressions describing the slip band-GBs interactions. Figure 3.5 shows a schematic of slip transfer across a grain boundary. θ is the angle between the two slip plane traces on the GB plane, κ is the angle between slip directions (Burgers vector), ψ is the angle between slip plane normal directions, and δ is the angle between the incoming slip direction and the intersection of the incoming slip plane with the GB plane. $\vec{b}$, $\vec{n}$, $\vec{l}$, and $\vec{d}$ represent the Burgers vector of the slip plane, the slip plane normal, the intersection line of slip plane and GB plane, and the slip direction, respectively. To find the above mentioned quantitative geometrical expressions for each slip band-GB interaction cases studied in this work, it is required to find the grain boundary plane orientation, the slip systems associated with the observed slip band at the grain boundary and the outgoing slip system of least resistance. The outgoing slip system of least resistance is interpreted as the slip system in the adjacent grain (Grain 2 in Figure 3.4), which offers the least resistance to transmission of the slip system in Grain 1. Crystal plasticity simulations are set up for the grain boundary neighborhoods to provide exactly this piece of information, the details of which are described later.

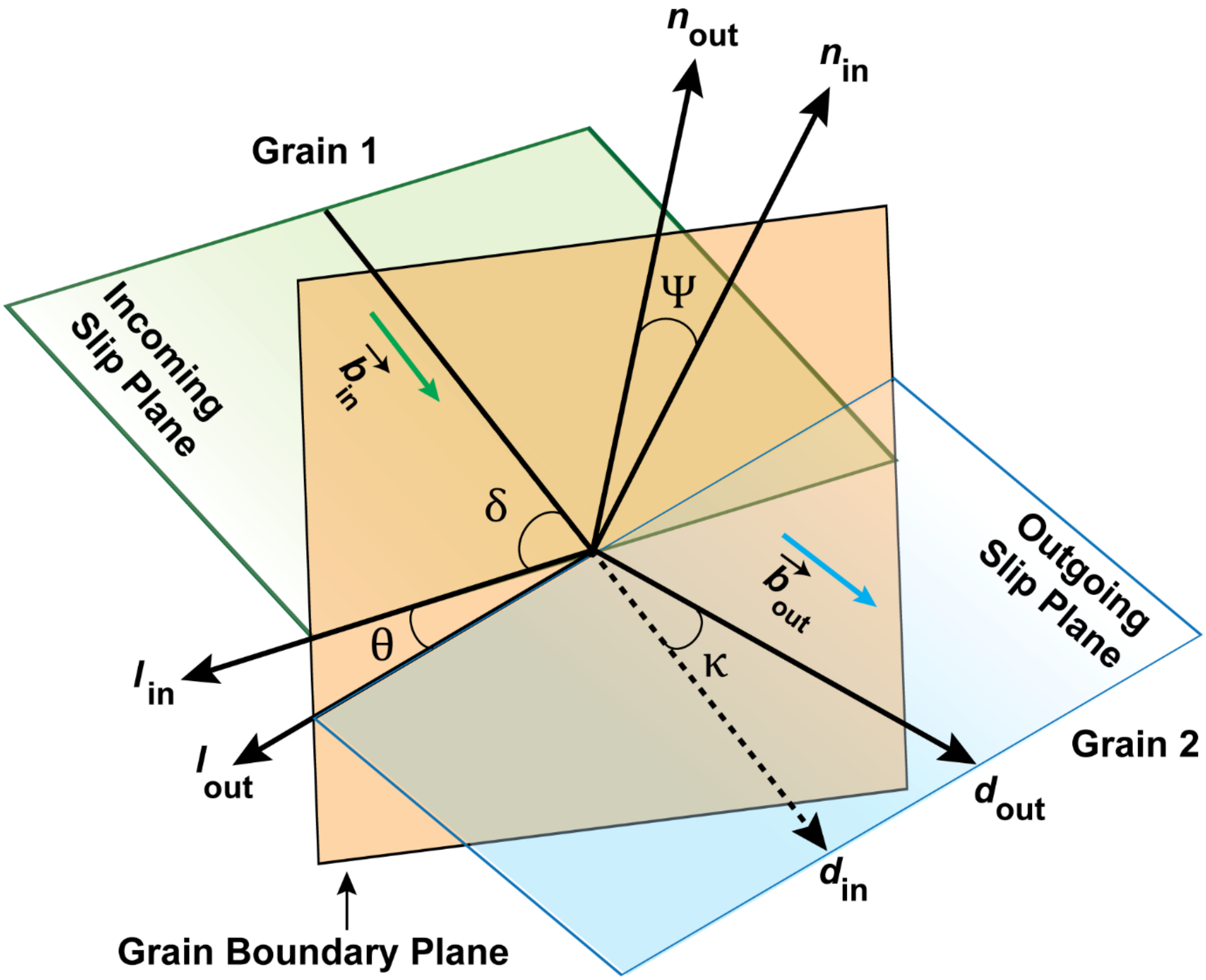

Figure 3.5 Schematic of a slip transmission through a grain boundary.

3.4.2.1 Grain Boundary Plane Orientations

The grain boundary plane (Figure 3.6a) can be described by the grain boundary *trace* angle (α), the angle between the line made by grain boundary plane on the sample surface and the loading axis (extrusion direction) (Figure 3.6b), and the grain boundary *plane* angle (β), the angle between the grain boundary plane and the sample surface normal (Figure 3.6c). The grain boundaries were first examined using SEM, and the plan view images of the grain boundaries were obtained after the horizontal direction was aligned with the loading axis, as shown in Figure 3.6d. This image was then post-processed manually to compute α. Subsequently, focused ion beam (FIB) milling on a FEI Helios Nanolab 650 was used to prepare cross-section lamellae of grain boundaries, as shown in Figure 3.6e. This image was then post-processed manually to obtain β. Since the slip band was not visible in the cross-sectional images, care was taken to ensure that these cross-sections were close enough to the slip band-GB intersection region to minimize error in the measured β value.

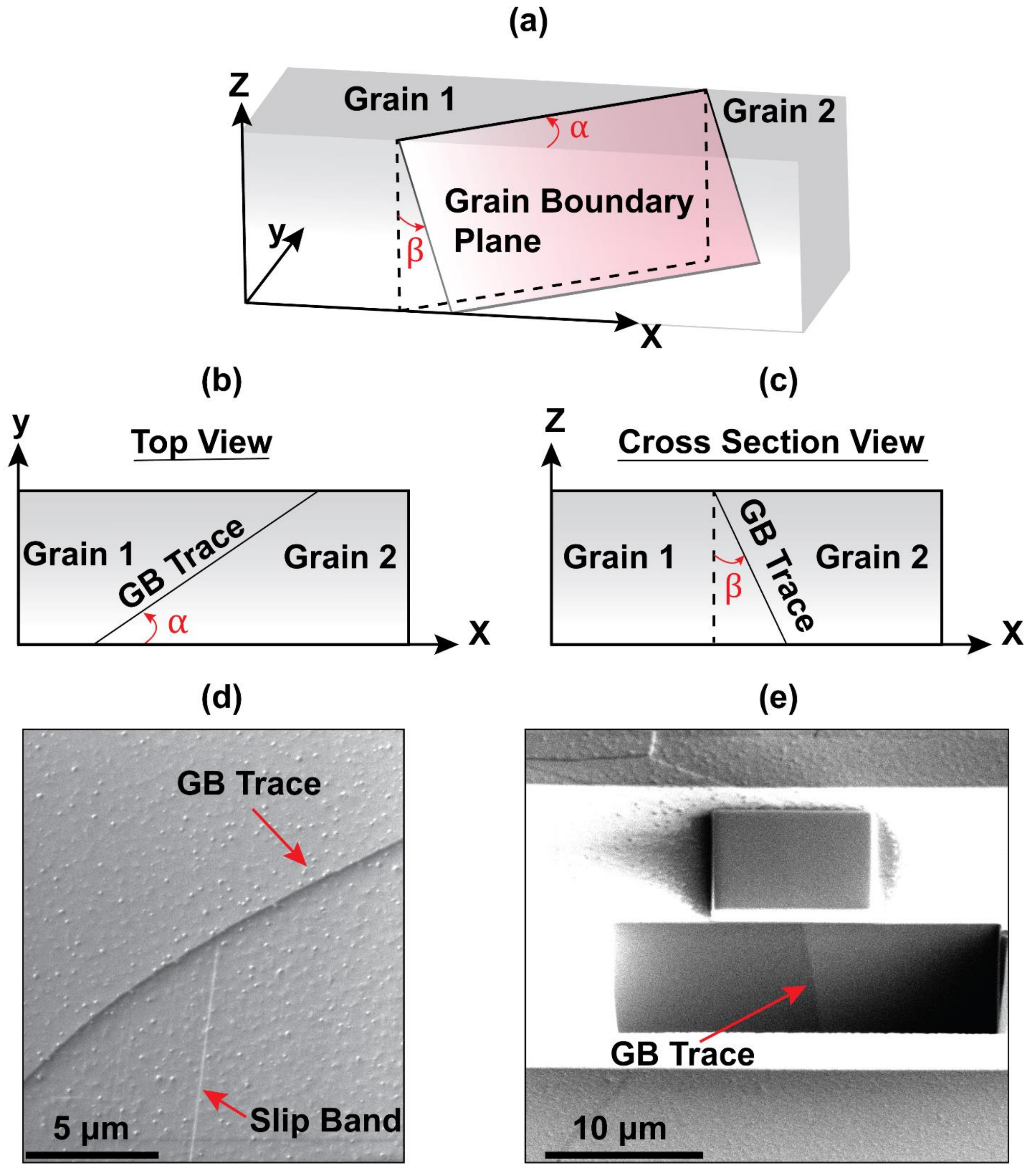

Figure 3.6 (a) Schematic showing the grain boundary plane, which can be described by (b) the grain boundary trace angle, and (c) the grain boundary plane angle. (d) The grain boundary trace angle (α) can be measured using the plan view image of the grain boundary. (e) The grain boundary plane angle (β) can be measured using cross-section lamellas of grain boundary prepared by FIB milling.

Table 3.4 Grain boundary plane orientation for different grain boundaries studied in this work.

GB ID	1	2	3	4	5	6	7	8	9
α (°)	58.35	104.59	40.21	109.96	91.98	17.75	91.33	65.47	16.43
β (°)	76.28	0.51	24.81	49.66	11.79	67.78	13.30	45.06	66.82

3.4.2.2 Grain neighborhood simulations

CPFE simulations were performed on microstructural neighborhoods of each GB of interest, consisting of the grains sharing that boundary and a few other surrounding grains. The aim was to find the active slip system associated with the observed slip band and predict the outgoing slip system of the least resistance. Since EBSD maps were available for just one section (sample surface), three-dimensionality of the problem was preserved by extruding the 2D section to obtain a one element slice of unit thickness, also implying that the subsurface grains were not considered as a part of the simulation. This is not problematic since the surface of the simulated microstructure is a traction-free surface in the experimental test as well. Earlier work [64] showed that under such circumstances, the inclusion of subsurface grains in the simulation affected the basal slip activity to a minor extent relative to simulations on the microstructure slice. Additionally, to overcome the lack of knowledge of the state of stress or displacements at the boundary of those neighborhoods, boundary conditions were enforced as follows:

(i) The x and y components of displacements were enforced on the lateral boundaries based on a constant velocity gradient reminiscent of uniaxial tension along direction y.

$$L = \dot{F}F^{-1},\ \ F(0) = I\ \Rightarrow\ F = \exp(tL)\ ;\ L\ = \begin{bmatrix} -0.5 & 0 & 0 \\ 0 & 1 & 0 \\ 0 & 0 & -0.5 \end{bmatrix} \tag{3.5}$$

$$u_x = F_{11}x + F_{12}y + F_{13}z\ , u_y = F_{21}x + F_{22}y + F_{23}z \tag{3.6}$$

where L is the velocity gradient, F is the deformation gradient, t is the time, and u_x and u_y are the x and y components of the displacement, respectively.

(ii) The $x - y$ face at $z = 0$ is constrained from displacing along the z direction while the opposite face is treated as a free surface.

Slices of the simulated microstructure were deformed to a strain of approximately 2% where the grains of interest show some slip activity in order to identify the most active system, which is computed as follows. For each element of the FE mesh, the accumulated slip for each slip system was computed based on the information available at the integration points. The most active slip systems were then identified as the one with the highest accumulated slip at the end of deformation. These IDs refer to those appearing in column 2 of Table 3.4.

The neighborhood microstructure corresponding to Grain Boundary 1 is shown in Figure 3.7a which consists of 21 grains. Figure 3.7b shows a map of the most active slip systems for each voxel of the entire microstructure visualized by their ID. It is evident that in the grain neighborhood shown in Figures 3.7a and 3.7b, basal slip is predicted to be the most active slip system. Grain Boundary 1 and the grains of interest are depicted in Figure 3.7c identifying the grain containing the slip band and the grain blocking the slip band, Figure 3.7d shows a map of the most active slip systems for all voxels belonging to the two grains of interest and Figure 3.7e depicts the von Mises equivalent stress map for the simulated microstructure. For the grain containing the slip band, CPFE augments the slip trace analysis because slip traces only convey information about the slip plane, but nothing is known about the slip direction. That is where the CPFE simulation results dictate the choice of the most active slip system, which is correlated with the slip trace in that grain. For the grain blocking the slip band (the adjacent grain) the most active slip system (potentially outgoing slip system) is interpreted as the one offering the least resistance to the slip band so that when slip transmission ensues, it occurs with the highest probability on this most active slip system. For this purpose, the region at the grain boundary containing the slip band in the real microstructure was identified by its corresponding voxel (V1) in the voxelated structure. Then the voxel next to V1 in the adjacent grain was identified, and the most active slip system was obtained. This slip system was chosen as the one offering the least resistance to the slip band. For Grain Boundary 1 based on prior arguments, the most active slip system in the adjacent grain has ID 1 which corresponds to the system $(0001)[11\bar{2}0]$ while the slip system corresponding to the slip bands has ID 3 which corresponds to the system $(0001)[1\bar{2}10]$.

Table 3.5 Slip and twin systems for Mg alloys.

Slip System	**ID**	**Slip Direction**	**Slip Plane**
Basal	1	$[11\bar{2}0]$	(0001)
	2	$[\bar{2}110]$	(0001)
	3	$[1\bar{2}10]$	(0001)
Prismatic<a>	4	$[1\bar{2}10]$	$(10\bar{1}0)$
	5	$[2\bar{1}\bar{1}0]$	$(01\bar{1}0)$
	6	$[11\bar{2}0]$	$(\bar{1}100)$
Pyramidal<a>	7	$[1\bar{2}10]$	$(10\bar{1}1)$
	8	$[\bar{2}110]$	$(01\bar{1}1)$
	9	$[\bar{1}\bar{1}20]$	$(\bar{1}101)$
	10	$[\bar{1}2\bar{1}0]$	$(\bar{1}011)$

	11	$[2\bar{1}\bar{1}0]$	$(0\bar{1}11)$
	12	$[11\bar{2}0]$	$(1\bar{1}01)$
Pyramidal<c+a>	13	$[\bar{1}\bar{1}23]$	$(11\bar{2}2)$
	14	$[1\bar{2}13]$	$(\bar{1}2\bar{1}2)$
	15	$[2\bar{1}\bar{1}3]$	$(\bar{2}112)$
	16	$[11\bar{2}3]$	$(\bar{1}\bar{1}22)$
	17	$[\bar{1}2\bar{1}3]$	$(1\bar{2}12)$
	18	$[\bar{2}113]$	$(2\bar{1}\bar{1}2)$
Twin<c + a>	19	$[\bar{1}011]$	$(10\bar{1}2)$
	20	$[10\bar{1}1]$	$(\bar{1}012)$
	21	$[\bar{1}101]$	$(1\bar{1}02)$
	22	$[1\bar{1}01]$	$(\bar{1}102)$
	23	$[0\bar{1}11]$	$(01\bar{1}2)$
	24	$[01\bar{1}1]$	$(0\bar{1}12)$

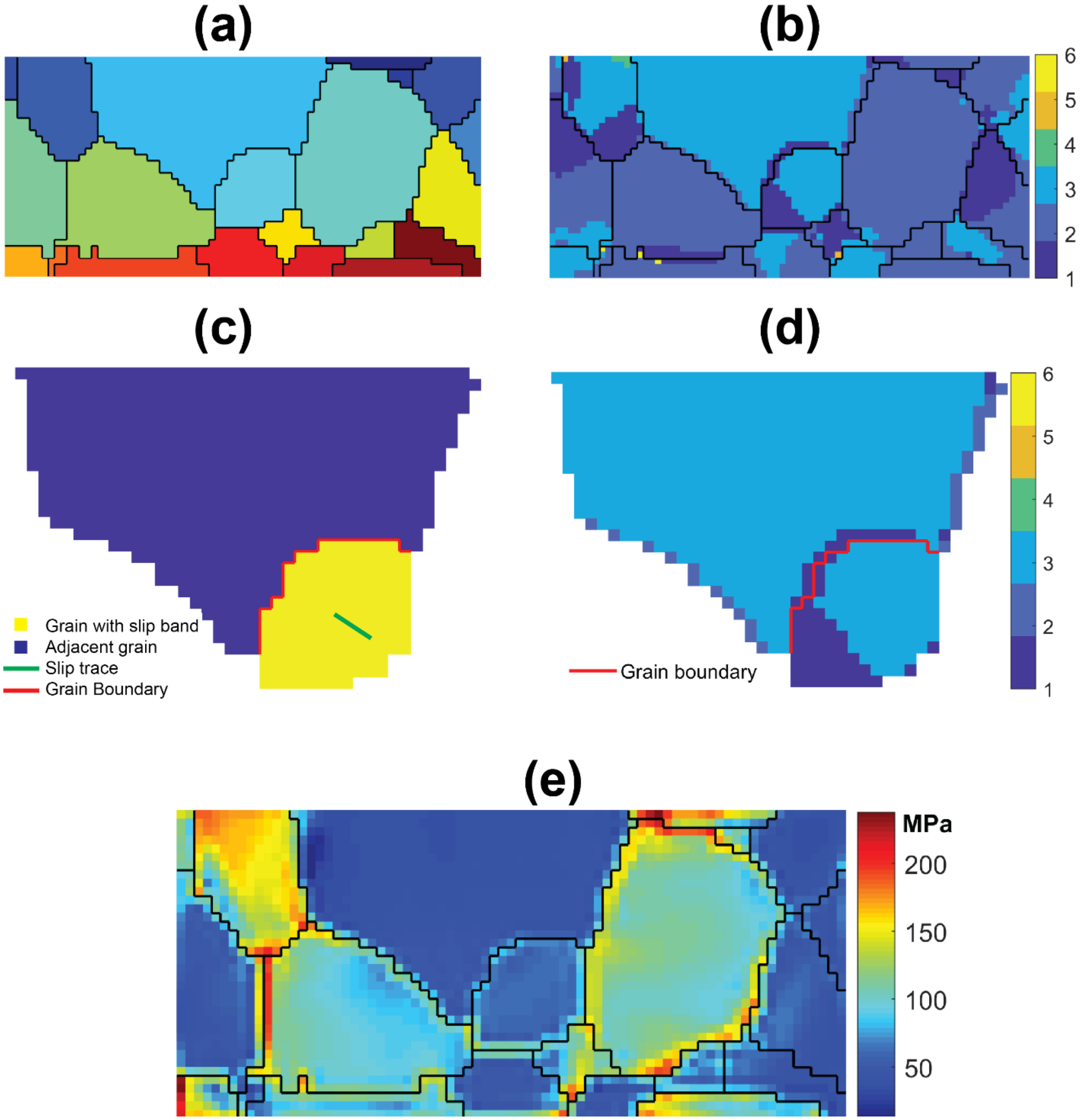

Figure 3.7 (a) Neighborhood microstructure related to Grain Boundary#1, and (b) its corresponding map of most active slip system ID (c) Microstructure of the grains sharing the grain boundary of interest, identifying the grain containing the slip band, the grain blocking the slip band, the grain boundary and the trace of the basal plane, and (d) a map of the most active slip systems in each voxel belonging to the grains sharing the grain boundary. Legend numbers (1-6) refer to the active slip system IDs in Table 3.5, and (e) von Mises equivalent stress map of the simulated microstructure.

3.4.3 Relationship between the micro-Hall-Petch coefficient and the quantitative geometrical expressions describing the slip band-GB interactions

Table 3.6 summarizes the slip systems of the identified incoming and potentially outgoing (offering the least resistance) slip system for each GB analyzed. The quantitative geometrical expressions (θ, κ, ψ, δ) were calculated for each GB cases, are also listed in Table 3.6. The total number of grains for each of the simulated microstructures described in section 3.3.2 is included in Table 3.6.

Table 3.6 Summary of the list of the incoming slip system and the predicted potentially outgoing slip system of each GB, and the quantitative geometrical expressions (θ,κ,ψ, δ) describing the slip band-GB interactions associated with each GB.

GB ID	Number of grains in the simulated microstructure	Incoming Slip System	Outgoing Slip System	θ (°)	κ (°)	ψ (°)	δ (°)
1	21	$(0001)[1\bar{2}10]$	$(0001)[11\bar{2}0]$	58.54	73.75	70.68	84.55
2	21	$(0001)[1\bar{2}10]$	$(0001)[1\bar{2}10]$	53.31	5.61	54.59	73.21
3	24	$(0001)[\bar{2}110]$	$(0001)[\bar{2}110]$	73.79	37.30	31.70	45.24
4	34	$(0001)[11\bar{2}0]$	$(0001)[11\bar{2}0]$	76.16	87.81	31.77	55.64
5	17	$(0001)[\bar{2}110]$	$(0001)[1\bar{2}10]$	33.87	55.69	25.95	26.46
6	28	$(0001)[1\bar{2}10]$	$(0001)[1\bar{2}10]$	38.84	54.14	48.32	86.18
7	16	$(0001)[\bar{2}110]$	$(0001)[\bar{2}110]$	46.52	46.94	47.13	24.57
8	21	$(0001)[1\bar{2}10]$	$(0001)[1\bar{2}10]$	74.92	66.16	87.18	34.41

9	25	$(0001)[11\bar{2}0]$	$(0001)[\bar{2}110]$	70.16	88.42	86.91	86.38

The micro-Hall-Petch coefficient values presented in Table 3.3 plotted against the angle between the two slip plane traces on the GB plane (θ) (Figure 3.8a), the angle between slip directions (κ) (Figure 3.8b), the angle between slip plane normal directions (ψ) (Figure 3.8c), and the angle between the incoming slip direction and the intersection of the incoming slip plane with the GB plane (δ) (Figure 3.8d). In order to quantify the correlation between the micro-Hall-Petch coefficient values and each of the quantitative geometrical expressions (θ,κ,ψ, δ), the *R*-squared value, also known as the coefficient of determination, was computed. This statistical correlation parameter is an indicator that ranges in value from 0 to 1. The higher the *R*-squared value, the more reliable the linear regression is. The calculated R-squared values are shown in each plot.

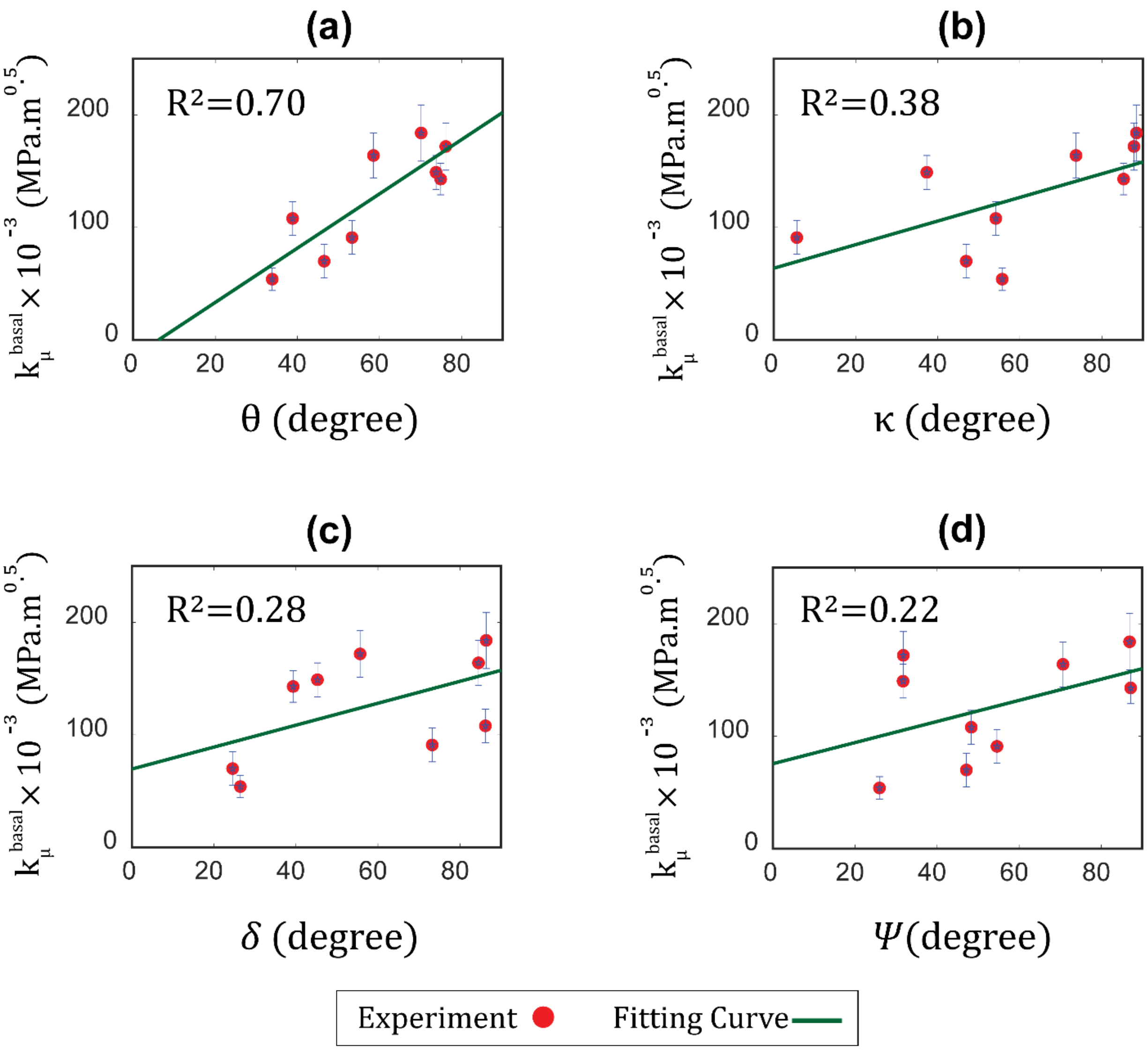

Figure 3.8 The micro-Hall-Petch coefficient values against (a) the angle between the two slip plane traces on the GB plane (θ). (b) the angle between slip directions (κ). (c) the angle between slip plane normal directions (ψ). (d) the angle between the incoming slip direction and the intersection of the incoming slip plane with the GB plane (δ).

3.5 Discussion

The blocked slip bands at the grain boundaries in Mg-4Al were investigated using HR-EBSD, cross-correlation analysis, and CPFE. Nine different grain boundaries were selected based on the existence of blocked slip bands at the GBs and various misorientation angles (Table 3.1).

CPFE and trace analysis (section 3.2.2) confirmed that the slip band in each case was associated with a basal slip system (Table 3.5). The full stress concentration tensor induced by the slip bands blocked at the GB was calculated using the HR-EBSD technique combined with the cross-correlation analysis (Section 3.3.1). The stress field was then resolved onto the active slip plane of the incoming slip band, and the resulting resolved shear stress profile was fit with the continuum dislocation pile-up model at a GB (Equation 3.3) to obtain the micro-Hall-Petch coefficient of each GB case (Table 3.3). The k_{μ}^{basal} values vary from 0.054 $\mathrm{MPa-m}^{\mathbf{1/2}}$ to 0.184 $\mathrm{MPa-m}^{\mathbf{1/2}}$ suggesting that the stress concentration ahead of a pile-up depends on the strength of each individual GB against slip transmission.

The k_{μ}^{basal} values are plotted against the quantitative geometrical expressions ($\theta, \kappa, \psi, \delta$), which describe the slip band-GBs interactions, as shown in Figure 3.8. The R^2 value used to find out which angle has a major effect on k_{μ}^{basal}. R^2 is higher for Figure 3.8a, which depicts the plot of k_{μ}^{basal} against the angle between the two slip plane traces on the GB plane (θ), suggesting the critical role of the grain boundary plane orientations in stress concentration ahead of pile up. The angle between slip plane traces on the GB plane also appears in Davis [65], where the investigations into slip continuity (transmission) motivated the stepped dislocation (see Figure 3.9) formation energy as a determining factor for slip transmission. The work done in order to overcome the energy barrier for stepped dislocation formation, under a number of assumptions of the theoretical model, was shown to be proportional to $\sin(\theta)$, hence motivating the consideration of θ as an important parameter in determining the strength of the GB to slip transmission and consequently the micro-Hall-Petch coefficient.

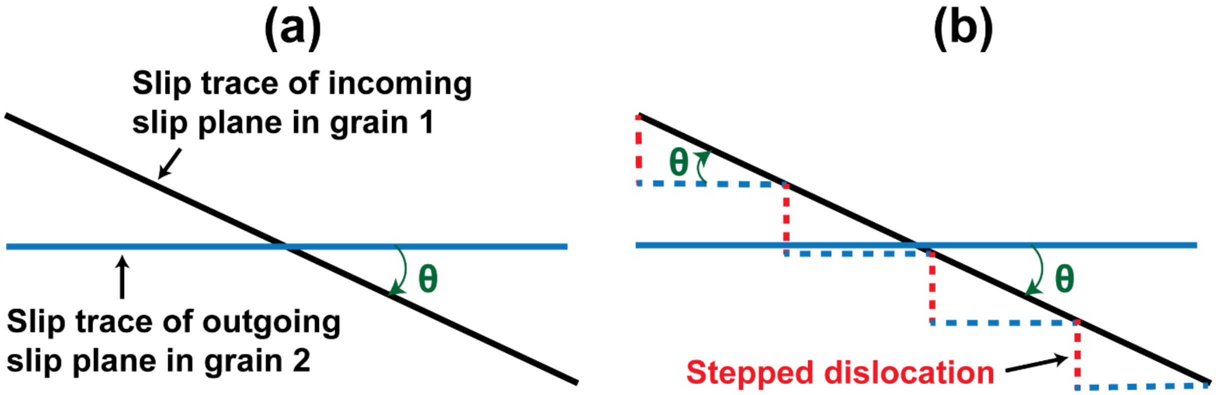

Figure 3.9 (a) Schematic of slip traces of incoming and outgoing slip planes looking into the grain boundary plane. (b) Schematic of the formation of a stepped dislocation in grain 2 when a dislocation crosses from grain 1. The dotted line represents the dislocation in grain 2. [65]

The angle between slip directions (κ) (Figure 3.8b) is the second most effective (R^2=0.38) quantitative geometrical expression in determining the k_{μ}^{basal}. Previous studies [66, 67] have reported that if the slip planes in two neighboring grains possess the same grain boundary trace and the Burgers vectors of dislocations are parallel (κ=0), then the dislocations in one grain can pass unhindered through the grain boundary into the adjacent grain. Consequently, increasing κ could result in an increase in the stress concentration ahead of pile up. It worth noting that since the incoming slip systems and predicted outgoing slip systems for all the nine-grain boundaries studied in this work are basal slip systems, the magnitude of residual Burgers vector (RBV) is directly proportional to $\sin\left(\frac{\kappa}{2}\right)$ which clearly increases with κ. The RBV has been previously studied as a criterion to evaluate the strength of a GB against slip transmission [68-71].

As shown in Figure 3.8c and 3.8d, k_{μ}^{basal}does not show a noticeable correlation with the ψ, the angle between slip plane normal directions, and δ, the angle between the incoming slip direction and the intersection of the incoming slip plane with the GB plane. This is because ψ does not capture the grain boundary plane orientations, which is present in the definition of θ, while δ does not have any information about the neighboring grain.

Taking into account both the geometrical and energetics aspects of k_{μ}^{α}, the following relationship is proposed:

$$k_{\mu}^{basal} = K^{basal}(1 - \cos(\theta)\cos(\kappa))^{c} \ ; c > 0 \qquad (3.7)$$

where K^{basal} and c are model parameters. The factor cos(θ)cos(κ) was initial proposed by Lee–Robertson–Birnbaum[61, 72, 73] as being relevant in the context of determining the outgoing slip system as a result of slip transmission across grain boundaries, based on *in situ* straining TEM experiments on FCC alloys. This relationship agrees with the Lim *et al*. [74] study where the strengthening effect of grain boundaries in Fe‑3%Si was modeled by defining the grain boundary obstacle stress τ_{obs} as $\tau_{obs} = (1 - \cos(\theta)\cos(\kappa)\ )\ \tau^{*}$ where τ^{*} represents the maximum obstacle strength. The Hall-Petch coefficient is known to be correlated with the GB obstacle stress [75] and hence, is indirectly related to the factor $(1 - \cos(\theta)\cos(\kappa))$.

k_{μ}^{basal} values obtained for the nine different cases in this study (Table 3.2) were fit with Equation 3.7 obtaining the model parameters $K^{basal} = 0.173\ \pm 0.083$ MPa $-$ m$^{\mathbf{1/2}}$ and c = 1.04. For the nine cases, k_{μ}^{basal} values are plotted against $(1 - \cos(\theta)\cos(\kappa))^{c}$ as shown in Figure 3.10. R^{2} value of 0.78 indicates the good correlation between the k_{μ}^{basal} and the proposed relationship. The aforementioned approach and findings are similar in spirit to the suggestions made by Guo [76] where a full three-dimensional analysis of the grain boundary geometry was deemed necessary to obtain a well-informed relationship between the stress concentration induced by blocked slip band at a grain boundary.

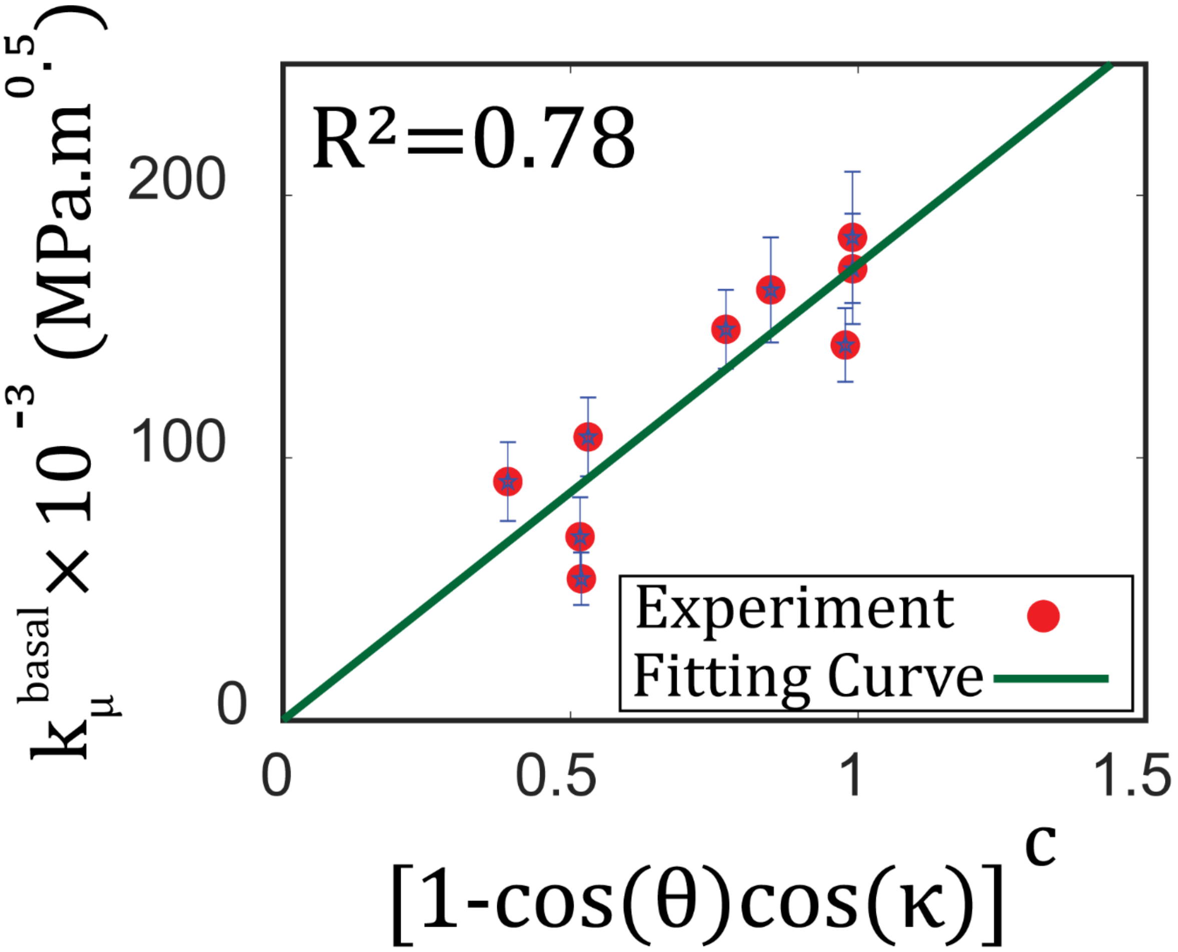

Figure 3.10 The basal slip system micro-Hall-Petch coefficients $\left(k_{\mu}^{basal}\right)$ for the nine-cases are plotted against the factor $(1-\cos(\theta)\cos(\kappa))^{c}$ where the model parameters K^{basal} and c were obtained from fitting the data points to a power-law. For this fit, R^2 is 0.78 which reflects close to the linear relationship between k_{μ}^{basal} and $(1-\cos(\theta)\cos(\kappa))^{c}$.

One may notice that the obtained values for k_{μ}^{basal} or K^{basal} may not be in complete agreement with the macroscopic Hall-Petch coefficients reported in the literature for Mg-4Al. For example, Deda *et al*. [77] obtained the value of 0.31 $\mathrm{MPa}-\mathrm{m}^{\mathbf{1/2}}$ for the macroscopic Hall-Petch slope of Mg-4Al. This discrepancy highlights the need for understanding the relationship between the macroscopic Hall-Petch coefficients and the strength of each grain boundary identified by micro-Hall-Petch coefficients. Although there are few studies on this topic [41, 44], what is still missing is a procedure to estimate the macroscopic Hall-Petch slope considering the effect of multiple factors simultaneously like texture, loading direction, alloying, misorientation distribution, etc. Equation 3.7 addresses part of this issue by encoding the effect of geometrical relationships into parameters quantifying size-effect at the slip system level. This must necessarily be complemented by some homogenization scheme to obtain estimates of the macroscopic Hall-Petch slope, which will be a subject of future work.

Crystal plasticity simulations have proven to be an indispensable tool in guiding our understanding of the effect of microstructure on the elastoplastic material behavior of polycrystalline solids. While classical crystal plasticity constitutive formulations provide a sound theoretical basis for modeling, their ability to incorporate microstructural size effect informed by experiments has been quite limited. The experiments performed in this work combined with adequate post-processing of the data can augment crystal plasticity models, where the micro-Hall-Petch equation can be used to modify the slip resistance based on the micro-Hall-Petch coefficient and some measure of the grain size. More importantly, since the current work proposes a functional form for the micro-Hall-Petch coefficient depending on the geometric properties of a grain and its immediate neighbors, the effect of texture can be directly encoded into this coefficient. Furthermore, instead of resorting to the average grain size for the entire microstructure, each point in a grain can be assigned an effective distance from the grain boundary, which can be used as the measure of grain size for that point. Once crystal plasticity models are appropriately calibrated, they can also be used to generate macroscopic Hall-Petch slope datasets amenable to data-mining approaches [78], which can furnish a pipeline (as opposed to a simple formula) to estimate the macroscopic Hall-Petch slope for a complex microstructure.

It is important to note that while the functional dependence of the micro-Hall-Petch coefficient is useful, crystal plasticity simulations may not predict macroscopic stress-strain curves consistent with experiments if these values are directly used to modify the slip resistances. This discrepancy can be attributed to multiple factors. Firstly, the analysis described in this work relies on data obtained from the vicinity of a slip band blocked by a grain boundary, which is a local measurement. Crystal plasticity simulations, however, are unable to model a slip band since they capture the physics in an average sense, i.e., the slip band itself is not modeled, but the accumulated slip in a grain conveys something about the accommodation of plastic deformation and the possibility of slip bands. Hence the attempt to use the micro-Hall-Petch coefficient from such local experiments into crystal plasticity simulations must be accompanied by a sensible scaling of the coefficient. Secondly, estimates of the micro-Hall-Petch coefficient have been obtained when a sufficient number of blocked slip bands were visually identified, and this meant deforming the sample to a higher strain than where the onset of plasticity actually occurs. Along with blocked slip bands, there were also grain boundaries through which slip transmission occurred, which were not the subject of this study but which clearly contribute to the polycrystalline size effect. It is still unclear how the information from transmitted slip and blocked slip bands can be used together to better estimate the micro-Hall-Petch coefficient that can be directly embedded into crystal plasticity constitutive models to predict the macroscopic stress-strain curves and Hall-Petch effect correctly. Finally, the stress profile ahead of a blocked slip band is expected to change depending on the accumulated plastic strain, and hence the total strain to which the sample was deformed. In other words, if the sample was deformed to a higher value of strain and the slip bands identified earlier continued to be blocked, a higher value of the micro-Hall-Petch coefficient would be expected to fit the resolved stress measurements. This begs the question as to which value would be appropriate. One way to bypass the previous issues is to consider only the dependence of the micro-Hall-Petch coefficient on the geometric parameters while selecting K^{basal} by calibrating stress-strain curve predictions from CPFEM to experiments. This also demands an acceptable representation of the grain boundary in the discretization of the microstructure because the $[\cos(\theta)\cos(\kappa)]$ factor depends on the grain boundary plane orientations and hence is sensitive to the discretization as well. All these issues represent challenges to incorporating the results from this work into crystal plasticity constitutive models and setting up acceptable simulations. This will be a subject of future work.

3.6 Conclusions

- High resolution electron backscatter diffraction method was used to measure the local stress ahead of blocked slip bands at grain boundaries in a deformed Mg-4Al alloy for nine different grain boundaries. The results were combined with a continuum dislocation pile-up model to assess the slip system level Hall-Petch slope for basal slip system (k_{μ}^{basal}). The results indicate that k_{μ}^{basal} values vary from 0.054 $\mathrm{MPa-m}^{\mathbf{1/2}}$ to 0.184 $\mathrm{MPa-m}^{\mathbf{1/2}}$.
- The k_{μ}^{basal} values were found to strongly correlate with the angle between the two slip plane traces on the GB plane (θ). This understanding highlights the important role of the grain boundary plane orientations in the slip system level Hall-Petch slope.
- The angle between slip directions (κ) was found to be the second most effective geometric parameter in determining the magnitude of k_{μ}^{basal}.
- A new equation, $k_{\mu}^{basal} = K^{basal}(1-\cos(\theta)\cos(\kappa))^{c}$, was proposed considering both the angle between the two slip plane traces on the GB plane (θ), and the angle between slip

directions (κ) to predict the slip system level Hall-Petch slope for basal slip system. This equation can be used to incorporate microstructural size effects in the crystal plasticity models.

3.7 References

1. Hirsch, J. and T. Al-Samman, *Superior light metals by texture engineering: Optimized aluminum and magnesium alloys for automotive applications.* Acta Materialia, 2013. **61**(3): p. 818-843.
2. Wang, X., et al., *What is going on in magnesium alloys?* Journal of Materials Science & Technology, 2018. **34**(2): p. 245-247.
3. Singh, A., et al., *Quasicrystal strengthened Mg–Zn–Y alloys by extrusion.* Scripta Materialia, 2003. **49**(5): p. 417-422.
4. Wu, B., et al., *Ductility enhancement of extruded magnesium via yttrium addition.* Materials Science and Engineering: A, 2010. **527**(16-17): p. 4334-4340.
5. Sandlöbes, S., et al., *Ductility improvement of Mg alloys by solid solution: Ab initio modeling, synthesis and mechanical properties.* Acta Materialia, 2014. **70**: p. 92-104.
6. Ma, X., et al., *Effect of Basal Precipitates on Extension Twinning and Pyramidal Slip: A Micro-mechanical and Electron Microscopy Study of a Mg-Al Binary Alloy.* Acta Materialia, 2020.
7. Nie, J.F., *Effects of precipitate shape and orientation on dispersion strengthening in magnesium alloys.* Scripta Materialia, 2003. **48**(8): p. 1009-1015.
8. Robson, J.D., N. Stanford, and M.R. Barnett, *Effect of precipitate shape on slip and twinning in magnesium alloys.* Acta materialia, 2011. **59**(5): p. 1945-1956.
9. Yu, H., et al., *Hall-Petch relationship in Mg alloys: a review.* Journal of Materials Science & Technology, 2018. **34**(2): p. 248-256.
10. Yuan, W., et al., *Influence of grain size and texture on Hall–Petch relationship for a magnesium alloy.* Scripta Materialia, 2011. **65**(11): p. 994-997.
11. Bohlen, J., et al., *The texture and anisotropy of magnesium–zinc–rare earth alloy sheets.* Acta Materialia, 2007. **55**(6): p. 2101-2112.
12. Stanford, N., et al., *Effect of microalloying with rare-earth elements on the texture of extruded magnesium-based alloys.* Scripta Materialia, 2008. **59**(7): p. 772-775.
13. Mishra, R.K., et al., *Influence of cerium on texture and ductility of magnesium extrusions*, in *Essential Readings in Magnesium Technology*. 2016, Springer. p. 363-368.
14. Hall, E., *Proc. Phys. Soc.* Series B, 1951. **64**: p. 747.
15. Petch, N., *The cleavage strength of polycrystals.* Journal of the Iron and Steel Institute, 1953. **174**: p. 25-28.
16. Armstrong, R.W., *60 years of Hall-Petch: past to present nano-scale connections.* Materials Transactions, 2014. **55**(1): p. 2-12.
17. Armstrong, R.W., *Hall–Petch k dependencies in nanopolycrystals.* Emerging Materials Research, 2014. **3**(6): p. 246-251.
18. Sangid, M.D., et al., *Energy of slip transmission and nucleation at grain boundaries.* Acta materialia, 2011. **59**(1): p. 283-296.

19. Han, J., S.L. Thomas, and D.J. Srolovitz, *Grain-boundary kinetics: A unified approach.* Progress in Materials Science, 2018. **98**: p. 386-476.
20. Wang, J., *Atomistic simulations of dislocation pileup: grain boundaries interaction.* JOM, 2015. **67**(7): p. 1515-1525.
21. Sangid, M.D., T. Ezaz, and H. Sehitoglu, *Energetics of residual dislocations associated with slip–twin and slip–GBs interactions.* Materials Science and Engineering: A, 2012. **542**: p. 21-30.
22. Kacher, J. and I.M. Robertson, *In situ TEM characterisation of dislocation interactions in α-titanium.* Philosophical Magazine, 2016. **96**(14): p. 1437-1447.
23. Kacher, J. and I.M. Robertson, *In situ and tomographic analysis of dislocation/grain boundary interactions in α-titanium.* Philosophical Magazine, 2014. **94**(8): p. 814-829.
24. Kacher, J. and I. Robertson, *Quasi-four-dimensional analysis of dislocation interactions with grain boundaries in 304 stainless steel.* Acta Materialia, 2012. **60**(19): p. 6657-6672.
25. Tucker, G.J., M.A. Tschopp, and D.L. McDowell, *Evolution of structure and free volume in symmetric tilt grain boundaries during dislocation nucleation.* Acta Materialia, 2010. **58**(19): p. 6464-6473.
26. Dewald, M. and W. Curtin, *Multiscale modelling of dislocation/grain boundary interactions. II. Screw dislocations impinging on tilt boundaries in Al.* Philosophical Magazine, 2007. **87**(30): p. 4615-4641.
27. Bayerschen, E., et al., *Review on slip transmission criteria in experiments and crystal plasticity models.* Journal of materials science, 2016. **51**(5): p. 2243-2258.
28. Spearot, D.E. and M.D. Sangid, *Insights on slip transmission at grain boundaries from atomistic simulations.* Current Opinion in Solid State and Materials Science, 2014. **18**(4): p. 188-195.
29. Koning, M.d., et al., *Modelling grain-boundary resistance in intergranular dislocation slip transmission.* Philosophical Magazine A, 2002. **82**(13): p. 2511-2527.
30. Kacher, J., et al., *Dislocation interactions with grain boundaries.* Current Opinion in Solid State and Materials Science, 2014. **18**(4): p. 227-243.
31. Patriarca, L., et al., *Slip transmission in bcc FeCr polycrystal.* Materials science and engineering: a, 2013. **588**: p. 308-317.
32. Bieler, T., et al., *Grain boundaries and interfaces in slip transfer.* Current Opinion in Solid State and Materials Science, 2014. **18**(4): p. 212-226.
33. Pineau, A., *Crossing grain boundaries in metals by slip bands, cleavage and fatigue cracks.* Philosophical Transactions of the Royal Society A: Mathematical, Physical and Engineering Sciences, 2015. **373**(2038): p. 20140131.
34. Armstrong, R., et al., *The plastic deformation of polycrystalline aggregates.* The Philosophical Magazine: A Journal of Theoretical Experimental and Applied Physics, 1962. **7**(73): p. 45-58.
35. Seok, M.-Y., et al., *Estimation of the Hall–Petch strengthening coefficient of steels through nanoindentation.* Scripta Materialia, 2014. **87**: p. 49-52.
36. Wu, D., et al., *Grain-boundary strengthening in nanocrystalline chromium and the Hall–Petch coefficient of body-centered cubic metals.* Scripta Materialia, 2013. **68**(2): p. 118-121.
37. Armstrong, R., *Theory of the tensile ductile-brittle behavior of poly-crystalline hcp materials, with application to beryllium.* Acta Metallurgica, 1968. **16**(3): p. 347-355.

38. Yuan, R., I.J. Beyerlein, and C. Zhou, *Coupled crystal orientation-size effects on the strength of nano crystals.* Scientific reports, 2016. **6**(1): p. 1-9.
39. Yu, H., et al., *The mechanism for the high dependence of the Hall-Petch slope for twinning/slip on texture in Mg alloys.* Acta Materialia, 2017. **128**: p. 313-326.
40. Wang, Y., et al., *Texture and weak grain size dependence in friction stir processed Mg–Al–Zn alloy.* Scripta Materialia, 2006. **55**(7): p. 637-640.
41. Wang, Y. and H. Choo, *Influence of texture on Hall–Petch relationships in an Mg alloy.* Acta Materialia, 2014. **81**: p. 83-97.
42. Armstrong, R.W., *Dislocation pile-ups, material strength levels, and thermal activation.* Metallurgical and Materials Transactions A, 2016. **47**(12): p. 5801-5810.
43. Wilson, D. and J. Chapman, *Effects of preferred orientation on the grain size dependence of yield strength in metals.* Philosophical Magazine, 1963. **8**(93): p. 1543-1551.
44. Guan, B., et al., *Quantitative prediction of texture effect on Hall–Petch slope for magnesium alloys.* Acta Materialia, 2019. **173**: p. 142-152.
45. Weng, G., *A micromechanical theory of grain-size dependence in metal plasticity.* Journal of the Mechanics and Physics of Solids, 1983. **31**(3): p. 193-203.
46. Sun, S. and V. Sundararaghavan, *A probabilistic crystal plasticity model for modeling grain shape effects based on slip geometry.* Acta Materialia, 2012. **60**(13-14): p. 5233-5244.
47. Liu, J., et al., *Mean-field polycrystal plasticity modeling with grain size and shape effects for laser additive manufactured FCC metals.* International Journal of Solids and Structures, 2017. **112**: p. 35-42.
48. Singh, A., et al., *Effect of microstructure on strength and ductility of high strength quasicrystal phase dispersed Mg–Zn–Y alloys.* Materials Science and Engineering: A, 2014. **611**: p. 242-251.
49. Wilkinson, A.J., G. Meaden, and D.J. Dingley, *High-resolution elastic strain measurement from electron backscatter diffraction patterns: new levels of sensitivity.* Ultramicroscopy, 2006. **106**(4-5): p. 307-313.
50. Britton, T.B. and A.J. Wilkinson, *Stress fields and geometrically necessary dislocation density distributions near the head of a blocked slip band.* Acta Materialia, 2012. **60**(16): p. 5773-5782.
51. Guo, Y., T. Britton, and A. Wilkinson, *Slip band–grain boundary interactions in commercial-purity titanium.* Acta Materialia, 2014. **76**: p. 1-12.
52. Guo, Y., et al., *Dislocation density distribution at slip band-grain boundary intersections.* Acta Materialia, 2020. **182**: p. 172-183.
53. Johnson, D., et al., *Quantitative analysis of localized stresses in irradiated stainless steels using high resolution electron backscatter diffraction and molecular dynamics modeling.* Scripta Materialia, 2016. **116**: p. 87-90.
54. Johnson, D., et al., *Quantitative Linkage between the Stress at Dislocation Channel–Grain Boundary Interaction Sites and Irradiation Assisted Stress Corrosion Crack Initiation.* Acta Materialia, 2019.
55. Andani, M.T., et al., *A quantitative study of stress fields ahead of a slip band blocked by a grain boundary in unalloyed magnesium.* Scientific reports, 2020. **10**(1): p. 1-8.
56. *BLG Vantage (*http://www.hrebsd.com.

57. Britton, T. and A. Wilkinson, *High resolution electron backscatter diffraction measurements of elastic strain variations in the presence of larger lattice rotations.* Ultramicroscopy, 2012. **114**: p. 82-95.
58. Yaghoobi, M., et al., *PRISMS-Plasticity: An open-source crystal plasticity finite element software.* Computational Materials Science, 2019. **169**: p. 109078.
59. Aagesen, L., et al., *Prisms: An integrated, open-source framework for accelerating predictive structural materials science.* JOM, 2018. **70**(10): p. 2298-2314.
60. Ganesan, S., *Microstructural response of magnesium alloys: 3D crystal plasticity and experimental validation*. 2017.
61. Shen, Z., R. Wagoner, and W. Clark, *Dislocation and grain boundary interactions in metals.* Acta metall., 1988. **36**(12): p. 3231-3242.
62. Hansen, L.T., et al., *An investigation of geometrically necessary dislocations and back stress in large grained tantalum via EBSD and CPFEM.* Materials Science and Engineering: A, 2020. **772**: p. 138704.
63. Akhtar, A. and E. Teghtsoonian, *Substitutional solution hardening of magnesium single crystals.* Philosophical Magazine, 1972. **25**(4): p. 897-916.
64. Githens, A., et al., *Characterizing microscale deformation mechanisms and macroscopic tensile properties of a high strength magnesium rare-earth alloy: A combined experimental and crystal plasticity approach.* Acta Materialia, 2020. **186**: p. 77-94.
65. Davis, K.G., *Slip continuity across grain boundaries in aluminum*. 1959, University of British Columbia.
66. Brandl, C., et al., *Slip transfer through a general high angle grain boundary in nanocrystalline aluminum.* Applied Physics Letters, 2007. **91**(11): p. 111914.
67. Beyerlein, I., et al., *Structure–property–functionality of bimetal interfaces.* Jom, 2012. **64**(10): p. 1192-1207.
68. Bollmann, W., *Crystal defects and crystalline interfaces*. 2012: Springer Science & Business Media.
69. Lim, L. and R. Raj, *The role of residual dislocation arrays in slip induced cavitation, migration and dynamic recrystallization at grain boundaries.* Acta Metallurgica, 1985. **33**(12): p. 2205-2214.
70. Marcinkowski, M. and W.F. Tseng, *Dislocation behavior at tilt boundaries of infinite extent.* Metallurgical Transactions, 1970. **1**(12): p. 3397-3401.
71. Lee, T., I. Robertson, and H. Birnbaum, *AnIn Situ transmission electron microscope deformation study of the slip transfer mechanisms in metals.* Metallurgical Transactions A, 1990. **21**(9): p. 2437-2447.
72. Shen, Z., R. Wagoner, and W. Clark, *Dislocation pile-up and grain boundary interactions in 304 stainless steel.* Scripta metallurgica, 1986. **20**(6): p. 921-926.
73. Lee, T., I. Robertson, and H. Birnbaum, *TEM in situ deformation study of the interaction of lattice dislocations with grain boundaries in metals.* Philosophical Magazine A, 1990. **62**(1): p. 131-153.
74. Lim, H., et al., *Simulation of polycrystal deformation with grain and grain boundary effects.* International Journal of Plasticity, 2011. **27**(9): p. 1328-1354.
75. Hirth, J.P., J. Lothe, and T. Mura, *Theory of dislocations*. 1983, American Society of Mechanical Engineers Digital Collection.
76. Guo, Y., *Exploration of microstructure related deformation gradients in commercial purity titanium*. 2015, The University of Oxford.

77. Deda, E., T.D. Berman, and J.E. Allison, *The influence of Al content and thickness on the microstructure and tensile properties in high-pressure die cast magnesium alloys.* Metallurgical and Materials Transactions A, 2017. **48**(4): p. 1999-2014.
78. Ramprasad, R., et al., *Machine learning in materials informatics: recent applications and prospects.* npj Computational Materials, 2017. **3**(1): p. 1-13.

Chapter 4: Estimation of Micro-Hall-Petch Coefficients for Prismatic Slip System in Mg-4Al as A Function of Grain Boundary Parameters

4.1 Abstract

Grain size strengthening, referred to as the Hall-Petch effect, is a common strategy to improve the yield strength of magnesium (Mg) alloys. Several experimental studies have reported that the Hall-Petch slope strongly depends on the texture of the alloy. This effect arises from altering grain boundaries (GBs) resistance to different slip systems to transfer across adjacent grains. The grain boundary barrier strength of certain grain boundaries to basal slip, referred to as basal micro-Hall-Petch, was investigated in the previous chapter. In this chapter, the micro-Hall-Petch coefficient values for the prismatic slip ($k_{\mu}^{prismatic}$) in Mg-4Al and their correlation with the grain boundary parameters were investigated. An experimental method was developed to initiate the prismatic slip band at low-stress levels. High-resolution electron backscatter diffraction (HR-EBSD) was used to measure the residual stress tensor, from which the resolved shear stress ahead of blocked prismatic slip bands was computed for seven different grain boundaries. $k_{\mu}^{prismatic}$ values for each individual GB were calculated by coupling the stress profile information with a continuum dislocation pile-up model. The $k_{\mu}^{prismatic}$ values vary from 0.138 $\mathrm{MPa.\,m}^{\mathbf{1/2}}$ to 0.685 $\mathrm{MPa.\,m}^{\mathbf{1/2}}$ which are almost three times larger than the calculated values for the basal micro-Hall-Petch. The $k_{\mu}^{prismatic}$ values were correlated with the GB parameters, and a functional relationship depending on the two most effective angles, the angle between the traces of the slip planes on the GB plane (θ) and the angle between incoming and outgoing slip directions (κ), was

proposed to estimate the Hall-Petch barrier for prismatic slip system. The work provides coefficients that can be supplied as input to crystal plasticity models to couple the effect of texture and grain size effectively.

4.2 Introduction

Owing to their low mass density, Mg alloys are attractive candidates for a range of industrial applications such as automotive [1], aerospace [2], and biomedical [3, 4] sections. However, the wide use of Mg alloys is limited by the low yield strength and formability at room temperature compared to the other structural materials such as aluminum and titanium. Alternative strategies to engineer the microstructure of Mg alloys to improve the yield strength and strain hardening include grain size refinement [5, 6], precipitate strengthening [7-10], solute strengthening [11-13], and texture modifications [14, 15].

Grain size strengthening is one of the most common strategies to enhance the yield strength of Mg alloys. The empirical Hall-Petch relationship defines the yield strength (σ_y) of a material as a function of its average grain size (D) following $\sigma_y = \sigma_0 + \frac{K}{\sqrt{D}}$, where K is the Hall-Petch coefficient and σ_0 is the friction stress [16-19]. Several experimental studies investigated the Hall-Petch relationship in Mg alloy and indicate that the Hall-Petch coefficient strongly depends on the texture of the alloy [5, 20-22]. For example, Yuan *et al*. [5] reported that the Hall-Petch coefficient for Mg–3Al–1Zn varies from 0.411 $\mathrm{MPa.m}^{\mathbf{1/2}}$ to 0.228 $\mathrm{MPa.m}^{\mathbf{1/2}}$ by changing the loading direction along two orthogonal directions. The reported correlation between the Hall-Petch slope and texture in Mg alloys is primarily due to the underlying crystal structure, hexagonal close-packed (HCP), being plastically anisotropic, i.e., the presence of different deformation modes with unequal strengths in these alloys. Texture variations can lead to activation of different deformation modes/systems, on which the GBs resistance to them can have a different effect, which results in altering the Hall-Petch coefficient.

To better understand the interactions of the Hall-Petch effect (grain size), texture, and grain boundary parameters, in the strengthening of materials, the Hall-Petch relationship needs to be investigated at the slip system level for each individual deformation mode. The Hall-Petch relationship extended to the microscale is given by $\tau^{\alpha} = \tau_0^{\alpha} + k_{\mu}^{\alpha}. L^{\alpha-1/2}$, where τ^{α} is the critical resolved shear stress corresponding to slip system α, τ_0^{α} is the critical resolved shear stress corresponding to slip system α of a theoretically infinite single crystal, k_{μ}^{α} the microscopic Hall-Petch coefficient of the slip system α (micro-Hall-Petch coefficient), and L^{α} is the grain size at the slip system-level for system α [23-25]. Since experimental approaches to quantify the stress tensor at the grain level are limited, very few studies focused on finding the micro-Hall-Petch coefficients for each individual slip system and the subsequent effect on the macroscopic Hall-Petch relationship [20, 26, 27]. Wang *et al*. [20] used the macroscopic tensile data of Mg–3Al–1Zn samples and estimate the variation of the resolved shear stress for each individual slip system by changing the grain size to calculate the micro-Hall-Petch slopes. They reported the micro-Hall-Petch coefficients for basal slip, prismatic slip, and pyramidal slip to be $0.091\mathrm{MPa.m}^{\mathbf{1/2}}$, $0.154\ \mathrm{MPa.m}^{\mathbf{1/2}}$ and $0.311\ \mathrm{MPa.m}^{\mathbf{1/2}}$, respectively. In our previous works [28, 29], we proposed using HR-EBSD to measure the local stress at the grain level and calculate the micro-Hall-Petch coefficient values for the basal slip in Mg alloys. The results show the micro-Hall-Petch coefficient values for the basal slip in Mg-4Al varies from $0.054\ \mathrm{MPa.m}^{\mathbf{1/2}}$ to $0.184\ \mathrm{MPa.m}^{\mathbf{1/2}}$ depending on the angle between incoming slip direction and the potential outgoing slip direction, and the angle between the two slip plane intersections with the GB.

In this chapter, we further expand on our previous results in order to understand the micro-Hall-Petch relationship for prismatic slip system in Mg-4Al. First, we present a novel method using micro-focused ion beam (FIB) notches to locally activate prismatic slip bands. We then use HR-EBSD measurements to assess the stress ahead of prismatic slip bands blocked at seven different GBs. The results are compared with a developed continuum dislocation pile-up model considering the presence of micro-FIB notch under two different boundary conditions to calculate the micro-Hall-Petch coefficient for prismatic slip systems. FIB milling is used to capture the three-dimensional grain boundary parameters (tilt and twist angles) of each individual grain boundary. A functional form to find the micro-Hall-Petch coefficient values of prismatic slip depending on the grain boundary descriptors is proposed, and the potential way to implement it to crystal plasticity constitutive models is discussed.

4.3 Methods

The author conducted the computational work in collaboration with Prof. Veera Sundararaghavan and his student Aaditya Lakshmanan.

4.3.1 Materials and experimental procedures

Mg-4Al (wt.%) produced by CanmetMaterials in the form of extruded bar is used in this study. The texture of the as-extruded material is shown in Figure 4.1a. The basal poles are oriented normal to the extrusion direction. This texture leads to activation of primarily basal and prismatic slip systems during plasticity when the loading direction is parallel to the extrusion direction. The average grain size of the as-received material was 55 µm. Further heat treatment is conducted to produce samples with average grain sizes of approximately 187 µm (515°C for 15 minutes) and 333 µm (550°C for 150 minutes) with a texture very similar to that shown in Figure 4.1a. Tensile tests are performed at a strain rate of $1 \times 10^{-3}\ s^{-1}$ for the samples with different grain sizes up to 2% strain. Figure 4.1b depicts the variation of the yield strength (0.2% offset) with average grain size, reflecting the Hall-Petch effect for this alloy. The linear fit of this data results in a Hall-Petch slope of $0.372\ \mathrm{MPa.m^{1/2}}$, consistent with previous findings for Mg-4Al [30].

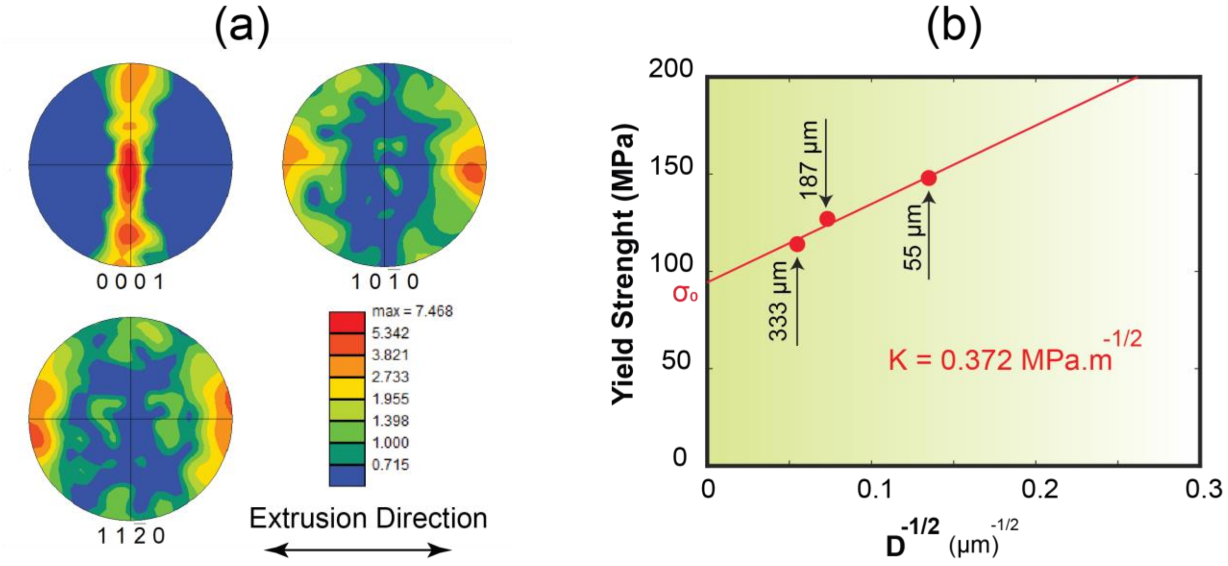

Figure 4.1 (a) Pole figure and (b) Hall-Petch relationship of extruded Mg-4Al (wt.%) sample used in this work. Linear fit yields $\sigma_0 = 94.33\ MPa\ , K = 0.372\ \mathrm{MPa.m^{1/2}}$.

Figure 4.2 depicts a microstructure section of the sample with the average grain size of 55 µm, which is primarily composed of equiaxed grains. From this sample, specimens with the gauge dimensions of 10 mm × 2 mm × 2 mm are cut using electrical discharge machining (EDM). The samples are then mechanically ground using SiC papers up to a grit of 1200. Polishing is completed using 6, 3, and 1 μm diamond suspensions, followed by a final polish using Buehler Masterpolish on a Buehler Chemomet polishing cloth. Samples are lightly chemically etched in acetic-nitric solution (60 mL ethanol, 20 mL water, 15mL acetic acid, and 5 mL nitric acid) for 3-5 seconds to highlight the grain boundaries.

Figure 4.2 EBSD inverse pole figure map of extruded Mg-4Al (wt.%) with the average grain size of 55 μm.

Our primary goal in this study is to initiate prismatic slip in the form of localized slip bands which would then be blocked by the grain boundary. It is well known that the anisotropy of the HCP crystal structure reflects significantly higher critical resolved shear stress for prismatic relative to the basal slip system. To preferentially activate prismatic slip at the low level of stress (which is important to consider for capturing high-resolution Kikuchi patterns) a series of sharp micro-notches are machined in grains oriented (relative to the loading direction) specifically for the prismatic slip to act as slip initiation sites. Given the EBSD data of the microstructure section (Figure 4.2), grains were chosen which satisfied the following conditions:

1. There is at least one prismatic slip system with a Schmid factor (corresponding to tension along the extrusion direction) greater than or equal to 0.4. This was to ensure that there is at least one prismatic slip system-oriented favorably for plastic slip relative to loading.
2. The ratio of the maximum Schmid factor of basal to the maximum Schmid factor of prismatic is at most 0.2. This was to ensure that the basal system is not as favorably oriented as the prismatic system obtained from step 1.

3. For ease of fabricating the notch using FIB-milling, with prismatic systems obtained from step 1 having a plane normal lying favorably in the plane of the sample surface.

The above steps were automated using a MATLAB script which employed the MTEX toolbox [31, 32] to post-process EBSD data. Once the grains of interest are identified, the micro-notches were created using an FEI Helios Nanolab 650 microscope equipped with a gallium ion source (see Figure 4.3a). Notches are machined parallel to the prismatic slip plane, and each had an approximate length of 20 µm, a width of 1 µm, and a depth of 10 µm (Figure 4.3(b)). The orientation of the prismatic slip system is known due to orientation data available from EBSD.

The tensile samples are then subjected to loading to observe slip band generation from notches. Figure 4.3(c) shows two examples of slip bands that initiate from notches; one was blocked at the grain boundary (GB#1), and the other one transferred to the adjacent grain (GB#2). Seven-grain boundaries are analyzed for this work since our focus is on boundaries that blocked slip transfer. Table 4.1 summarizes the information of these GBs based on the misorientation between adjacent grains.

Kikuchi patterns ahead of blocked slip bands are captured using a TESCAN RISE microscope equipped with a Hikari Super EBSD detector provided by EDAX. The EBSD maps had an average size of 20 µm × 20 µm with a square grid, and 200 nm step size. The CrossCourt4 (CC4) software package developed by BLG Vantage is used to analyze the Kikuchi patterns and assess the full strain/stress fields across the grains by implementing the cross-correlation approach developed by Wilkinson *et al*. [33]. The remapping method developed by Britton and Wilkinson [34] is also applied to minimize the effect of the lattice rotation on calculated strain/stress values.

Upon completing the EBSD analysis, the subsurface grain boundary orientations are measured to understand the grain boundary plane orientations. To accomplish this, FIB milling is used to lift out lamellae perpendicular to the grain boundary line using an FEI Helios Nanolab 650 microscope.

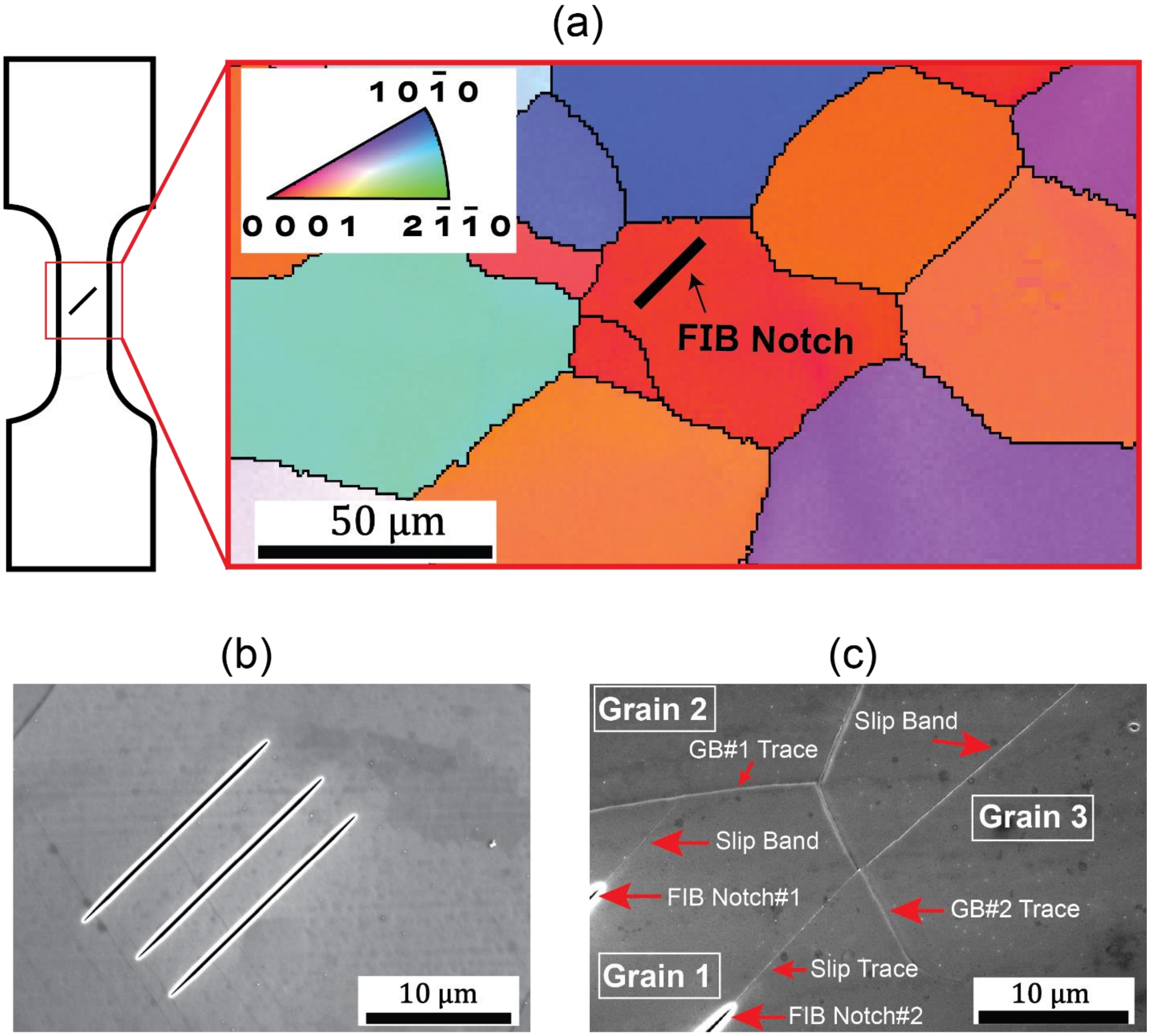

Figure 4.3 (a) Diagram showing placement of FIB notch parallel to prismatic slip planes, (b) Examples of micro-notch machined on the surface of the samples to act as slip initiation sites, (c) Example of slip bands initiate from FIB notch and interact with GBs. Slip transmission occurs in GB#2, and pile-up occurs in GB#1.

Table 4 .4.1 Misorientation angle and rotation axis of the GBs investigated in this work.

GB Number	Misorientation (°)	Rotation Axis
1	84.70	$[\bar{6}\ 11\ \bar{5}\ 1]$
2	52.38	$[8\ \bar{9}\ 1\ 1]$
3	79.89	$[\overline{11}\ \bar{9}\ 20\ 1]$
4	62.67	$[9\ 3\ \overline{12}\ \bar{1}]$
5	65.61	$[\overline{17}\ \bar{2}\ 19\ 1]$
6	38.36	$[5\ 8\ \overline{13}\ 1]$
7	36.84	$[9\ 8\ \overline{17}\ 0]$

4.3.2 Analytical and Numerical Methods

This section is devoted to outlining the analytical and numerical methods that form the basis of our work. First, the continuum dislocation pile-up theory in 1D is reviewed, which furnishes a closed-form expression for the stress ahead of the pile-up. Following that, essential aspects of the rate-dependent crystal plasticity are described which are implemented into the PRISMS-Plasticity [35] crystal plasticity finite element (CPFE) framework. Finally, the calibration procedure to obtain constitutive model parameters is outlined, followed by the methodology to simulate neighborhoods of grain boundaries of interest-based on experimental data.

4.3.2.1 Dislocation Pile-up Model of Notch and Slip Band

A simple one-dimensional continuum dislocation pile-up model is used as an analogy to describe the region in the grain constituting the notch and the slip band (Figure 4.4). Both the notch and the slip band are represented by a continuous distribution of straight parallel edge dislocations [36, 37] with the dislocation line pointing in the z-direction, and Burgers vector along the x −direction with magnitude b_e.

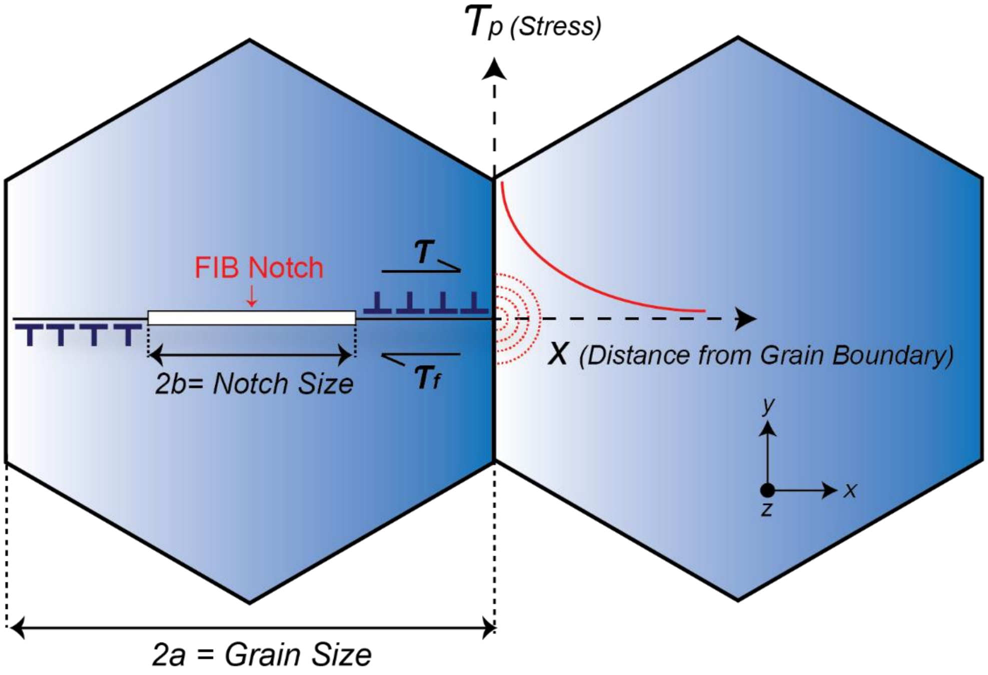

Figure 4.4 Notch and slip band idealized as a continuous distribution of parallel edge dislocations.

Let *ρ(x)* denote the distribution of dislocations in the domain [-*a*, *a*] where the subdomain [-*b*, *b*] represents the notch. We would then like to solve for *ρ(x)* which is in equilibrium with an effective resolved stress $\tau_e(x)$, where the equilibrium condition takes the following form [38]

$$\frac{\mu b_e}{2\pi(1-\nu)}\left\{\int_{-a}^{-b}\frac{\rho(x')dx'}{x - x'}+\int_{-b}^{b}\frac{\rho(x')dx'}{x - x'}+\int_{b}^{a}\frac{\rho(x')dx'}{x - x'}\right\}+\tau_e(x)=0$$

$$\tau_e(x) = \begin{cases}\tau & ;\ |x| < b\\ \tau-\tau_f & ;\ b < |x| < a\end{cases} \tag{4.1}$$

where μ is the shear modulus, ν is the Poisson's ratio and τ_f is a friction stress acting only in the slip band, which inhibits the motion of the prismatic dislocations. τ_f is assumed to be a constant. We are interested in a closed-form expression for the resolved stress ahead of the pile-up, $\tau_p(x)$, defined as follows:

$$\tau_p(x) := \frac{\mu b_e}{2\pi(1-\nu)}\left\{\int_{-a}^{-b}\frac{\rho(x')dx'}{x - x'} + \int_{-b}^{b}\frac{\rho(x')dx'}{x - x'} + \int_{b}^{a}\frac{\rho(x')dx'}{x - x'}\right\};\ x > a \qquad (4.2)$$

Eqn. 4.1 is an integral equation with a closed-form solution [39] for $\rho(x)$, which upon substituting in Eqn. 4.2 yields

$$\tau_p(x) = \frac{\left(\tau - 2\tau_f \cos^{-1}\left(\frac{b}{a}\right)\right)}{\sqrt{1 - \left(\frac{a}{x}\right)^2}} + 2\tau_f \operatorname{cosec}^{-1}\left(\sqrt{1 + \frac{(x^2 - a^2)b^2}{(a^2 - b^2)x^2}}\right) - \tau;\ x > a \qquad (4.3)$$

Shifting the origin to $x = a$ by defining $X = x - a$, and substituting x in terms of X yields

$$\tau_p(X) = \frac{\left(\tau - 2\tau_f \cos^{-1}\left(\frac{b}{a}\right)\right)}{\sqrt{1 - \left(\frac{a}{X+a}\right)^2}} + 2\tau_f \operatorname{cosec}^{-1}\left(\sqrt{1 + \frac{((X+a)^2 - a^2)b^2}{(a^2 - b^2)(X+a)^2}}\right) - \tau \qquad (4.4)$$

Eqn. (4.4) is now valid for $X > 0$. We now invoke the micro-Hall-Petch assumption [28, 29] where τ is additively decomposed into size-independent and size-dependent contributions. Since we invoke this at the level of the slip system, we replace τ with τ^α corresponding to slip system α. The decomposition then takes the simple form

$$\tau^\alpha = \tau_0^\alpha + \frac{k_\mu^\alpha}{\sqrt{2a}} \qquad (4.5)$$

where τ_0^α is the lattice friction stress for slip system α, k_μ^α is the micro-Hall-Petch coefficient and a is the grain size as defined in Figure 4.4. Substituting Eqn. 4.5 into Eqn. 4.4 and specializing to slip system α yields.

$$\tau_p^\alpha(X) = \frac{\left(\tau_0^\alpha + \frac{k_\mu^\alpha}{\sqrt{a-b}} - 2\tau_f^\alpha \cos^{-1}\left(\frac{b}{a}\right)\right)}{\sqrt{1-\left(\frac{a}{X+a}\right)^2}} + 2\tau_f^\alpha \operatorname{cosec}^{-1}\left(\sqrt{1 + \frac{((X+a)^2 - a^2)b^2}{(a^2-b^2)(X+a)^2}}\right) - \left(\tau_0^\alpha + \frac{k_\mu^\alpha}{\sqrt{2a}}\right) \tag{4.6}$$

Eqn. 6 furnishes an expression for the resolved stress ahead of the pile-up, which is fit to the data obtained from HR-EBSD residual stress measurements. Here a and b are length dimensions that can be measured from the images (Figure 4.3). An estimate of τ_0^α is obtained using σ_0 (y-intercept in Figure 4.1(b)) and the average Schmid factor associated with prismatic slip for the present as-extruded texture. The average Schmid factor for prismatic slip is obtained by first computing the maximum Schmid factor for each orientation among the prismatic slip systems, and then finding the mean of those values. In our case, this value is 0.451, very similar to previous work [40] which reported a value of 0.43. σ_0 denotes the yield strength for the microstructure with theoretically infinite grain size and multiplying this by the average Schmid factor for prismatic slip results in an estimate of the grain-size independent critical resolved shear stress for prismatic slip. In our case setting $\sigma_0 = 94.33\ MPa$ and using 0.451 as the Schmid factor for prismatic slip [40], yields $\tau_0^\alpha = 42.54\ MPa$. The parameters k_μ^α and τ_f^α are the unknowns which are optimized by performing a least-squares fit of Eqn. 4.6 to the residual stress measurements.

4.3.2.2 Single Crystal Constitutive Model

We adopt a rate-dependent crystal plasticity constitutive model within the finite deformation continuum mechanics framework. The primary kinematic ingredient is the deformation gradient, $\mathbf{F}$, which maps infinitesimal material fibers in the reference configuration to corresponding fibers in the deformed configuration. We assume $\mathbf{F}$ to abide by a multiplicative decomposition [41, 42] into elastic and plastic components, denoted by $\mathbf{F}^{\mathrm{e}}$ and $\mathbf{F}^{\mathrm{p}}$, respectively, as follows:

$$\mathbf{F} = \mathbf{F}^{\mathrm{e}}\mathbf{F}^{\mathrm{p}} \tag{4.7}$$

Physically, $\mathbf{F}^{\mathrm{p}}$ encodes the homogenized distortion of the body as a consequence of crystallographic slip via dislocation motion on specific slip systems. It maps the reference configuration to an intermediate configuration where the underlying lattice remains unchanged. $\mathbf{F}^{\mathrm{e}}$, on the other hand, captures the elastic stretch and lattice rotation and maps the intermediate configuration to the deformed configuration. Since plasticity is inherently deformation path-dependent, we invoke certain deformation rates.

Using Eqn. (4.7), the velocity gradient, $\mathbf{L} = \dot{\mathbf{F}}\mathbf{F}^{-1}$, can then be expanded additively decomposed into elastic and plastic components

$$\mathbf{L} = \underbrace{\dot{\mathbf{F}}^{\mathrm{e}}\mathbf{F}^{\mathrm{e}-1}}_{\text{Elastic part}} + \underbrace{\mathbf{F}^{\mathrm{e}}\dot{\mathbf{F}}^{\mathrm{p}}\mathbf{F}^{\mathrm{p}-1}\mathbf{F}^{\mathrm{e}-1}}_{\text{Plastic part}} \tag{4.8}$$

The contributions to the velocity gradient from elastic and plastic parts are both defined in the deformed configuration. We can alternatively work with the plastic part of the velocity gradient defined on the intermediate configuration, $\mathbf{L}^{\mathrm{p}}$, as:

$$\mathbf{L}^{\mathrm{p}} = \dot{\mathbf{F}}^{\mathrm{p}}\mathbf{F}^{\mathrm{p}-1} \tag{4.9}$$

Noting that the kinematics of crystallographic slip effectively involves shearing of the lattice on specific crystallographic slip planes along with specific crystallographic slip directions, we have

$$\mathbf{L}^{\mathrm{p}} = \dot{\mathbf{F}}^{\mathrm{p}}\mathbf{F}^{\mathrm{p}-1} = \sum_{\alpha=1}^{n_s} \dot{\gamma}^{\alpha}\mathbf{m}^{\alpha}\otimes\mathbf{n}^{\alpha} = \sum_{\alpha=1}^{n_s} \dot{\gamma}^{\alpha}\mathbf{S}^{\alpha} \tag{4.10}$$

where $\dot{\gamma}^{\alpha}$ is the shearing rate on slip system α, n_s is the number of slip systems, $\mathbf{m}^{\alpha}$ and $\mathbf{n}^{\alpha}$ are slip direction and slip plane normal unit vectors, respectively. $\mathbf{S}^{\alpha}$, referred to as the Schmid tensor for the slip system α, is a shorthand for the dyadic product of $\mathbf{m}^{\alpha}$ and $\mathbf{n}^{\alpha}$. We note that $\mathbf{m}^{\alpha}$ and $\mathbf{n}^{\alpha}$ are crystallographic vectors in the intermediate configuration.

We adopt a rate-dependent crystal plasticity framework, where the shearing rate $\dot{\gamma}^{\alpha}$ is a function of the resolved shear stress τ^{α} through a phenomenological power law [43] as follows:

$$\dot{\gamma}^{\alpha} = \dot{\gamma}_0 \left|\frac{\tau^{\alpha}}{s^{\alpha}}\right|^{m} \mathrm{sign}(\tau^{\alpha}) \tag{4.11}$$

where $\dot{\gamma}_0$ is the reference shearing rate, m is the strain rate, sensitivity exponent, τ^{α} is the resolved shear stress on slip system α, s^{α} is the slip resistance on slip system α and 'sign' refers to the signum function. The resolved shear stress is expressed in terms of the second Piola-Kirchoff stress in the intermediate configuration [44, 45], $\mathbf{T}$, via the following relation

$$\tau^{\alpha} = (\mathbf{F}^{\mathrm{eT}}\mathbf{F}^{\mathrm{e}}\mathbf{T}) : \mathbf{S}^{\alpha} \tag{4.12}$$

where ':' denotes the inner product of second-order tensors defined as $\mathbf{A} : \mathbf{B} = A_{ij}B_{ij}$. Eqn. (4.12) is derivable by equating the plastic part of the internal mechanical power to the power expended in crystallographic shearing of slip system α with resolved shear stress τ^{α} and shearing rate $\dot{\gamma}^{\alpha}$. The second Piola-Kirchoff stress in the intermediate configuration is linked to the elastic Green-Lagrange strain as follows

$$\mathbf{T} = \mathcal{L} \cdot \mathbf{E}^{\mathrm{e}} = \frac{1}{2}\mathcal{L} \cdot (\mathbf{F}^{\mathrm{eT}}\mathbf{F}^{\mathrm{e}} - \mathbf{I}) \tag{4.13}$$

where $\mathbf{E}^{\mathrm{e}}$ is the elastic Green-Lagrange strain tensor, $\mathcal{L}$ is the elastic stiffness (a fourth-order tensor) and $\mathbf{I}$ is the second-order identity tensor. '·' denotes the product between a fourth-order tensor and second-order tensor to furnish a resultant second-order tensor, defined as $(\mathcal{L} \cdot \mathbf{A})_{ij} = \mathcal{L}_{ijkl}A_{kl}$. We additionally note that the Cauchy stress, $\boldsymbol{\sigma}$, and the first Piola-Kirchoff stress in the reference configuration, $\mathbf{P}$, can be computed from $\mathbf{T}$ as follows:

$$\mathbf{T} = \mathbf{F}^{\mathrm{e}-1}\mathbf{P}\,\mathbf{F}^{T}\mathbf{F}^{\mathrm{e}-T} = \det(\mathbf{F}^{\mathrm{e}})\mathbf{F}^{\mathrm{e}-1}\boldsymbol{\sigma}\,\mathbf{F}^{\mathrm{e}-T} \tag{4.14}$$

Finally, the evolution of slip resistance for slip system α, which governs isotropic hardening, is defined as follows [45]:

$$\dot{s}^{\alpha} = \sum_{\beta} h^{\alpha\beta}\dot{\gamma}^{\beta} \tag{4.15}$$

where $h^{\alpha\beta}$, denotes the hardening rate on slip system α due to the slip-on system β. The hardening moduli $h^{\alpha\beta}$ are prescribed as a power-law relationship involving the combined effect of work hardening and recovery, with both self and latent hardening contributions as follows:

$$h^{\alpha\beta} = \begin{cases} h_0^{\beta}\left[1 - \dfrac{s^{\beta}}{s_s^{\beta}}\right]^{a^{\beta}} & ;\ \text{coplanar systems} \\ h_0^{\beta} q\left[1 - \dfrac{s^{\beta}}{s_s^{\beta}}\right]^{a^{\beta}} & ;\ \text{otherwise} \end{cases} \tag{4.16}$$

where h_0^{β} denotes the hardening parameter for slip system β, q is the latent hardening ratio, s_s^{β} is the saturation slip resistance for slip system β, and a^{β} is a material constant for slip system β governing the sensitivity of the hardening moduli to the slip resistance.

The constitutive model is implemented in the PRISMS-Plasticity CPFE code, an open-source, scalable software framework to simulate elasto-plastic boundary value problems [35, 46] using the finite element method. In the interest of being succinct, only the constitutive model has been outlined here. For detailed derivations including the incremental constitutive update scheme and derivation of an algorithmic tangent modulus, the reader is referred to previous work [47].

4.3.2.3 Constitutive Model Calibration

The crystal plasticity constitutive model parameters are obtained by matching the stress-strain curves between simulations and experiments for Mg-4Al samples for two scenarios. Figs. 4.5(a)- 4.5(b) depict the pole figures corresponding to the samples from these scenarios along with the sample reference frame x-y-z. In the first scenario, the sample was subject to uniaxial tension along the y-direction (Figure 4.5(a)), deformed up to a strain of approximately 2.5%. In the second scenario, the sample was subjected to uniaxial tension along the z-direction (Figure 4.5(b)), deformed up to a strain of approximately 0.6%. For the simulations, cubical synthetic microstructures were generated using DREAM.3D [48] using the respective textures. For both the cases, 60x60x60 voxelated microstructures containing approximately 2000 grains were instantiated, with the cube length set to L = 500 μm. The cubes were subject to symmetry boundary conditions, depicted in Figs. 4.5(c)- 4.5(e), where u_0 denotes the maximum displacement applied to the face subject to non-zero displacement boundary condition, similar to the experiment. For the first scenario, u_0 was set to 10 μm (0.025 x L), while for the second scenario u_0 was set to 3 μm (0.006 x L). These match the approximate macroscopic strain levels that the samples were subject to in the experiments.

All crystal plasticity simulations were performed assuming possible activity of 12 slip systems - 3 basal, 3 prismatic, 6 pyramidal <c+a> - and 6 pyramidal <c+a> twin systems. Figure 4.5(f) and Figure 4.5(g) depict the comparison between the stress-strain curves from CPFE simulations and experiments for the first and second scenario, respectively, showing a satisfactory match in the plastic regime for the strain regimes considered. Table 4.2 lists the elastic stiffness constants used in calibration [49-51] and Table 4.3 lists the crystal plasticity constitutive model parameters obtained post-calibration. In the hardening law, the latent hardening coefficient was set to $q = 1.0$, while the flow rule parameters were set as $\dot{\gamma}_0 = 0.001$ and $m = 34$.

4.3.2.4 Grain Boundary Neighborhood Simulations

To construct grain boundary descriptors through which a relationship can be drawn to the micro-Hall-Petch coefficient, some information about the slip activity in the grains is necessary. By virtue of capturing the resolved stress ahead of the blocked slip band, the slip system in the adjacent grain which could potentially accommodate slip transmission, is not known. In the grain containing the slip band, the slip trace and crystallographic orientation can be used to infer the slip system corresponding to that slip band (incoming slip system). To find the slip system that could potentially accommodate slip transmission (potential outgoing slip system), crystal plasticity simulations are employed.

To accomplish this, for each grain boundary case studied, a rectangular region around this grain boundary is identified (Figure 4.6(a)), which contains the grains sharing this boundary and some of their neighbors. The approximate coordinates of the center of the notch and its length are identified (Figure 4.6(b)). This information is then used to create a rectangular geometry of the region of interest, with the notch approximated as an ellipse with the same center as that of the notch and major axis length equal to the length of the notch. The minor axis length of the ellipse is set to 1 μm. This microstructure section (a 2D section) is then meshed using 4-node quadrilateral elements via the functionality of Gmsh [52], an open-source 3D finite element mesh generator (Figure 6(d)). The elements are then assigned an identifier corresponding to whichever grain they constitute in the original microstructure (Figure 4.6(c)). Finally, since we are simulating three-dimensional geometries using our CPFE framework, the 2D microstructure section is extruded along the third direction to create a slice of the microstructure, where the 4-node quadrilateral elements now turn to 8-node brick elements.

Then each microstructure section was subjected to deformation via two boundary conditions:

(iii) **Boundary Condition 1** – For the four lateral boundaries (x=0, x=L_x, y=0, y=L_y), the x and y components of displacements were enforced based on a constant velocity gradient representative of uniaxial tension along the x-direction.

$$\mathbf{L} = \dot{\mathbf{F}}\mathbf{F}^{-1},\;\; \mathbf{F}(0) = \mathbf{I} \;\Rightarrow\; \mathbf{F} = \exp(t\mathbf{L})\;;\; \mathbf{L} \;=\; \begin{bmatrix} 1 & 0 & 0 \\ 0 & -0.5 & 0 \\ 0 & 0 & -0.5 \end{bmatrix} \tag{4.17}$$

$$u_x = F_{11}x + F_{12}y + F_{13}z\;, u_y = F_{21}x + F_{22}y + F_{23}z$$

where **F** is the time-dependent deformation gradient, **L** is the constant velocity gradient, t is the time, and u_x and u_y are the x and y components of the displacement, respectively. The face z-displacement of the face $z = 0$ is set to 0 while the opposite face is treated as a traction-free surface.

(iv) **Boundary Condition 2**: Symmetry boundary conditions are enforced. The surfaces x=0, y=0 and z=0, respectively, are constrained from displacing along the direction perpendicular to corresponding faces. The surfaces y = L_y and z = L_z are traction free while the face x = L_x is displaced along the x-direction by the amount u_0.

Two sets of boundary conditions were chosen as possible portrayals of tension along x-direction, since the true deformation of the microstructural boundary is not available. Microstructure slices in the simulations strained to about 2% along the x-direction so that the grains under investigation show some slip activity in order to identify the potential outgoing slip system in the grain blocking the slip band. We choose this to be the slip system with the highest accumulated slip in the neighborhood of the slip trace-grain boundary intersection once the deformation of the microstructure section is complete.

Table 4.2 Elastic stiffness constants (in GPa) for Mg-4Al alloy [49-51]

C_{11}	C_{33}	C_{12}	C_{13}	C_{44}
59.4	61.6	25.61	21.44	16.4

Table 4.3 Crystal plasticity constitutive model parameters post-calibration

Mode	s_0^α	h_0^α	s_s^α	a^α
Basal <a>	10.0	0.0	-	1.0
Prismatic <a>	78.0	1000.0	150.0	1.0
Pyramidal <c + a>	140.0	0.0	-	1.0
Twin <c + a>	18.0	0.0	-	1.0

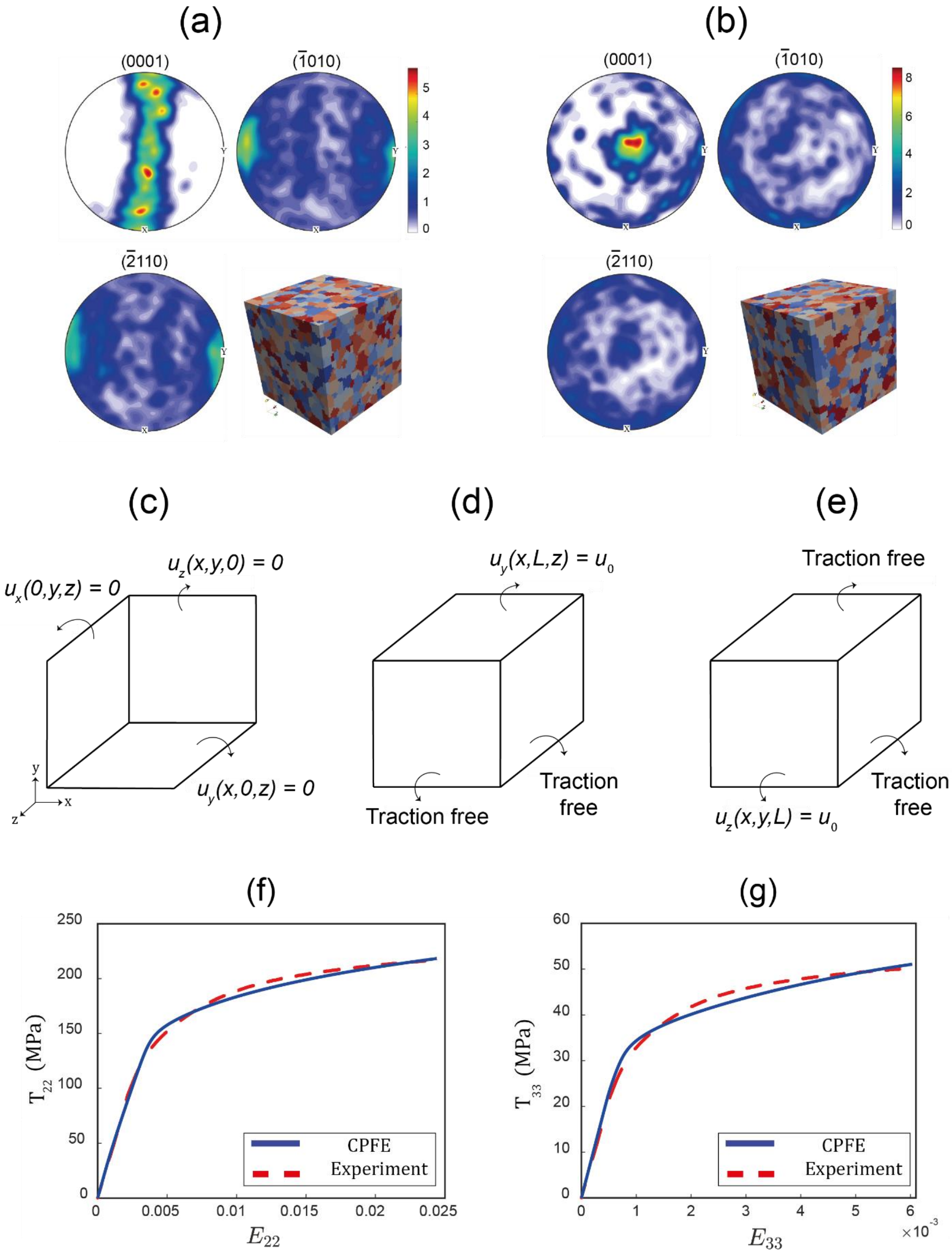

Figure 4.5 a) Pole figures and synthetic microstructure for first scenario, (b) Pole figures and synthetic microstructure for second scenario, (c) Faces at x=0, y=0 and z=0 enforced as flat surfaces, (d) Deformation boundary condition for first scenario, (e) Deformation boundary condition for second scenario, (f) Stress-strain curve comparison between CPFE and experiments for the first scenario, and (g) Stress-strain curve comparison between CPFE and experiments for the second scenario.

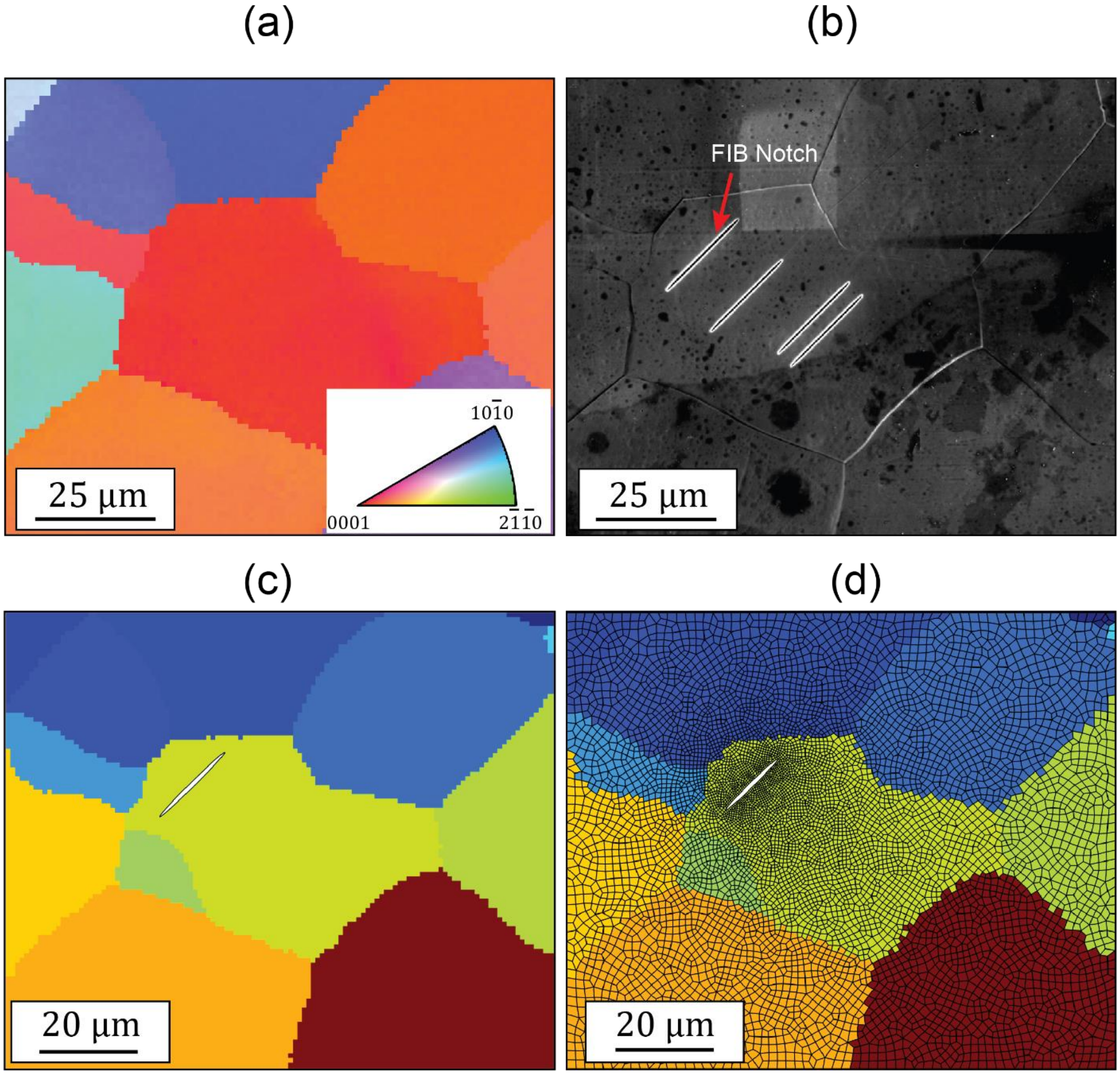

Figure 4.6 (a) EBSD section for the region around grain boundary, (b) Grain with notch generated using FIB, (c) Grain identifiers for microstructure section, and (d) Microstructure section meshed using Gmsh with 4-node quadrilateral elements with grain identifiers assigned.

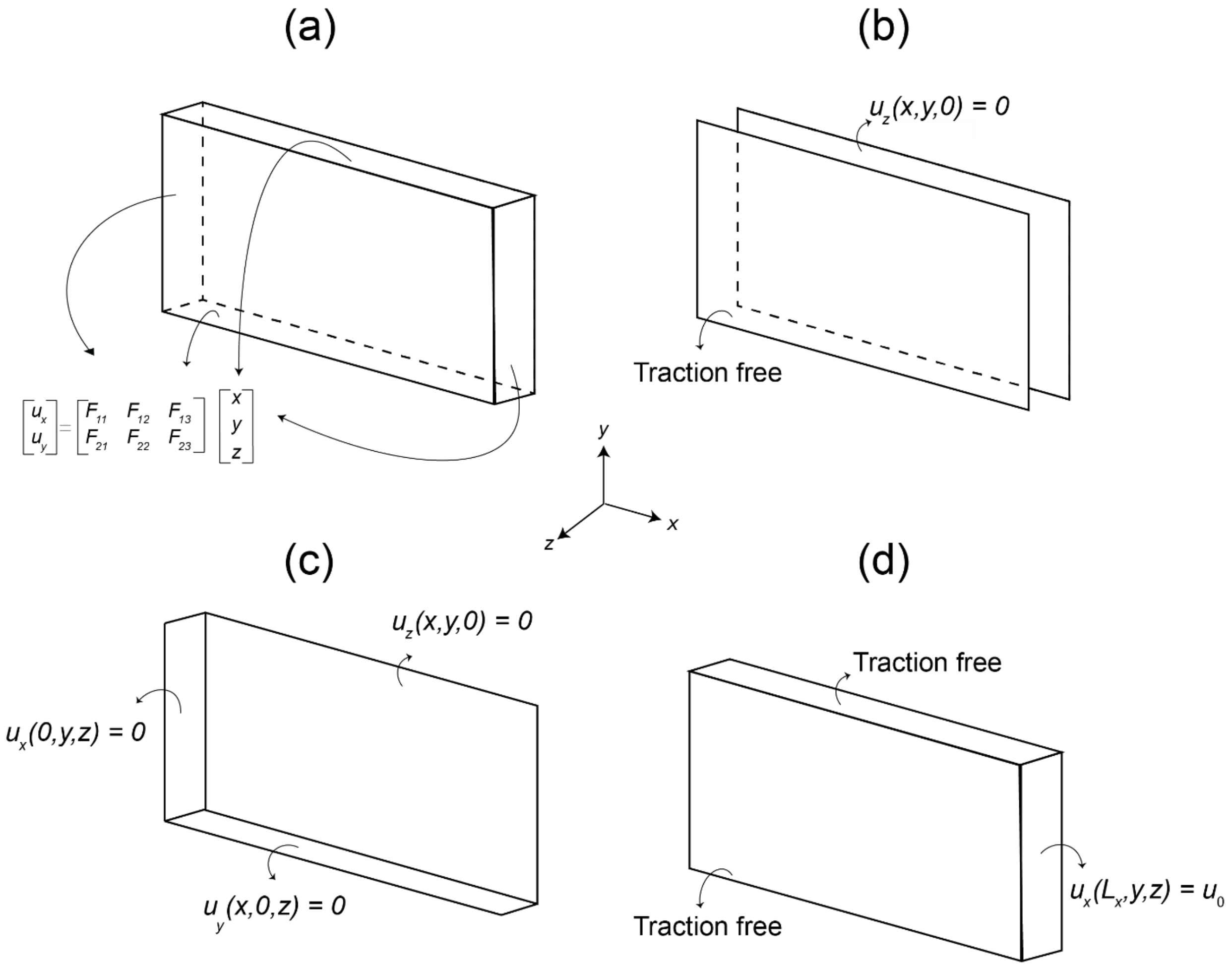

Figure 4.7 Boundary condition 1 (BC#1): (a) *x* and *y* displacement components set on lateral surfaces, (b) *x*-*y* plane constrained along *z*-direction, Boundary condition 2 (BC#2): (c), (d) denote symmetry boundary conditions similar to the boundary condition enforced in the calibration section for scenario 1.

4.4 Results

4.4.1 Micro-Hall-Petch Coefficient Calculation

Grain boundaries that block the slip bands generated from the micro-notches are found using SEM, as shown in Figure 4.3(c) (GB#1). HR-EBSD scans around the interaction zones are captured and the full elastic stress tensor is calculated in the sample. An example of the full tensor map of the stress concentration ahead of a blocked slip band measured by HR-EBSD is shown in

Figure 4.8. More details on how to measure stress components by HR-EBSD are discussed in the previous studies [53, 54]. As it can be seen from Figure 4.8, the stress induced by the blocked slip band at the grain boundary is revealed most clearly in the σ_{11} and σ_{22} stress components.

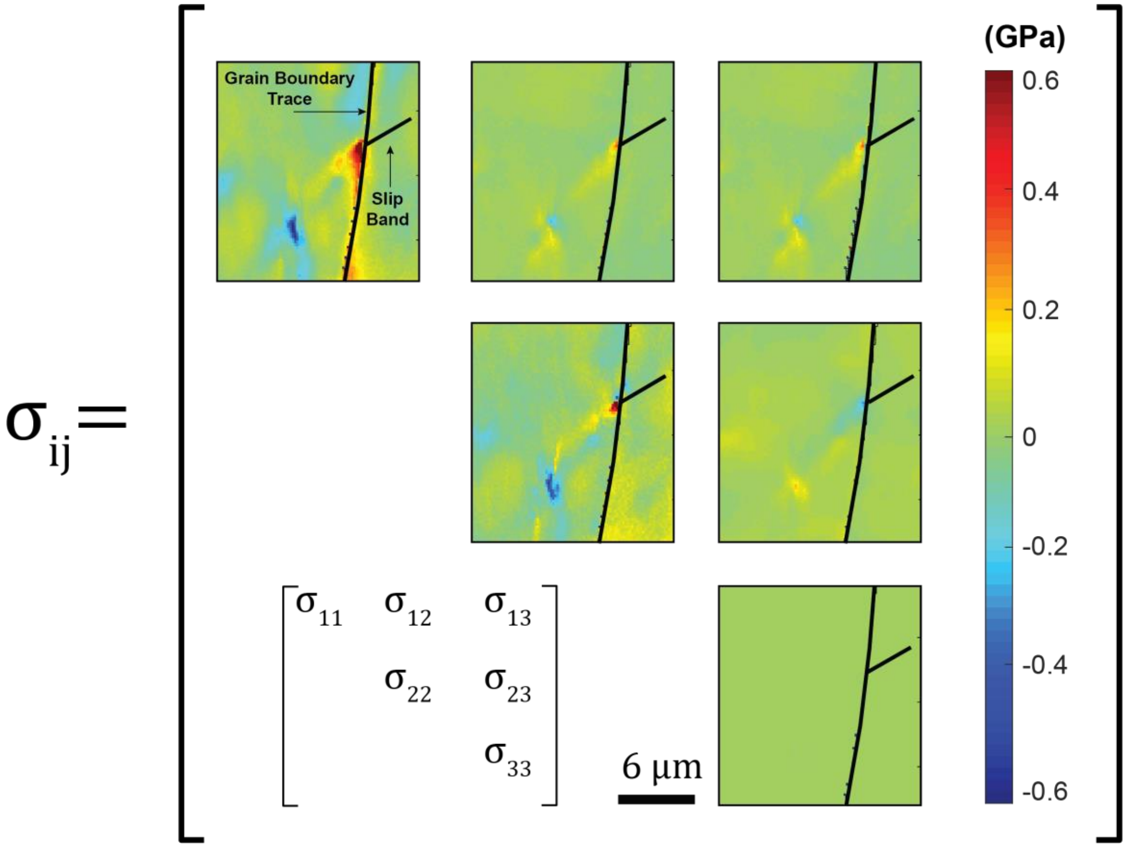

Figure 4.8 An example of full stress tensor measured in the sample frame by HR-EBSD for a slip band blocked at Grain Boundary 1 (Note: these images are rotated 180 degrees from Figure 4.3).

The stress tensors in the sample frame are then resolved onto the active slip system of the deformed grain determined by methods explained in section 4.2.2.4. Figure 4.9(a) shows an example of the resolved shear stress derived by rotation of stress tensor shown in Figure 8 to another axis system $x_1^r x_2^r x_3^r$, where x_1^r, x_3^r, and x_2^r are along the slip plane normal, Burgers vectors, and the direction perpendicular to the Burgers vector on the slip plane of the active slip system, respectively.

Stress values ahead of the pile up is extracted along with the slip band in the undeformed grain, indicated by X direction in Figure 4.9(a). The stress values are compared with the dislocation pile-up model given by Eqn. 4.6 as shown in Figure 4.9(b). The experimental data shows the same trend as the theoretical model. The micro-Hall-Petch coefficients k_{μ}^{α}, for all seven grain boundaries are estimated by fitting the experimental data with the dislocation pile-up model, and the results are presented in Table 4.4. The slip system level grain sizes in the deformed grains and the micro-notch sizes for each grain boundary are also reported in Table 4.4.

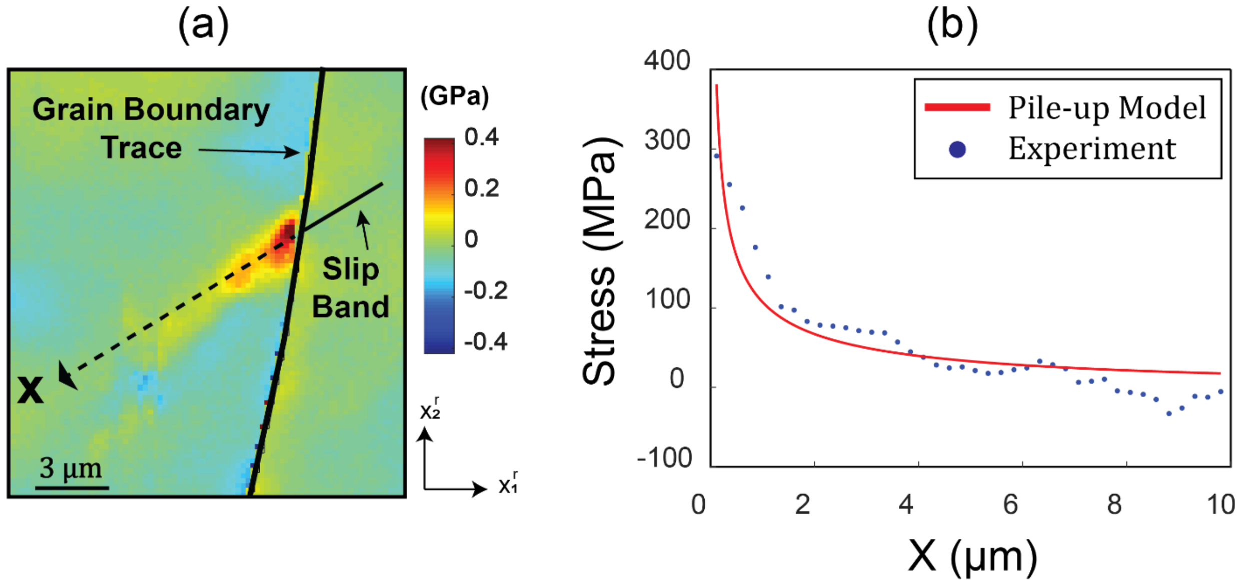

Figure 4.9 (a) HR-EBSD stress map of the resolved shear stress on the active slip system in the right grain. The active slip system is defined based on the trace analysis and CPFE. The observed stress profile in front of the pile-up is extracted along the dashed line and compared with the pile-up model. (b) The comparison of resolved shear stress ahead of pile-up was measured by HR-EBSD and the pile-up model (Eqn. 4.6) to assess the prismatic micro-Hall-Petch slope in different GBs.

Table 4.4 A list of the prismatic micro-Hall-Petch coefficient for different GB

GB Number	1	2	3	4	5	6	7
Slip Level Grain Size in the Grain with Slip Band (μm)	40	40	39	44	41	41	41
Notch Size (μm)	20	20	19	21	18	17	17
$k_{\mu}^{prismatic}$ $(\mathbf{MPa.m^{1/2}})$	0.455 ± 0.05	0.618 ± 0.06	0.661 ± 0.07	0.635 ± 0.07	0.685 ± 0.02	0.138 ± 0.02	0.641 ± 0.07

4.4.2 Grain Boundary Parameters

To understand the effect of grain boundary parameters on micro-Hall-Petch coefficient, the quantitative geometrical angles describing the slip transmission across grain boundary as shown in Figure 4.10 need to be determined. To achieve this goal (4.3.2.1), the grain boundary plane orientation angles are measured, and (4.3.2.2) the active slip systems in Grain 1 (grain with the slip band, Grain 1 in Figure 4.3c) and Grain 2 (grain without evidence of any slip band, Grain 2 in Figure 4.3c) are determined.

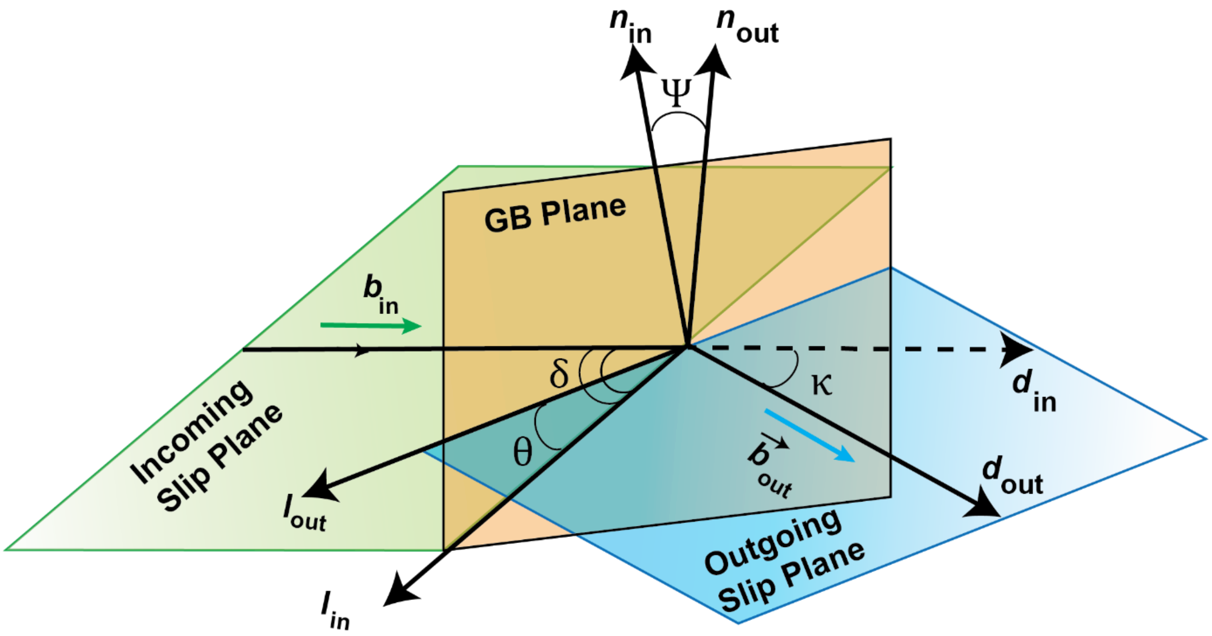

Figure 4.10 A schematic representative for slip transmission through a GB. $\vec{b}_{in}$: Burgers vector of the incoming slip system, $\vec{b}_{out}$: Burgers vector of the outgoing slip system, $\vec{n}_{in}$: Slip plane normal of the incoming slip system, $\vec{n}_{out}$: Slip plane normal of the outgoing slip system, $\vec{l}_{in}$: Intersection line of the incoming slip plane and GB, $\vec{l}_{out}$: Intersection line of the outgoing slip plane and GB, $\vec{d}_{in}$: Slip direction of the incoming slip system, $\vec{d}_{out}$: Slip direction of the outgoing slip system, θ: Angle between the two slip plane traces on the grain boundary plane, κ: Angle between slip directions, ψ: Angle between slip plane normal, δ: Angle between the incoming slip direction and the incoming slip plane trace on the grain boundary plane.

4.4.2.1 Grain Boundary Plane Orientation Angles Measurement

The GB plane orientation angles include the *trace* angle (α), defined as the angle between the loading direction and the trace of the GB plane on the sample surface, and the grain boundary *plane* angle (β), defined as the angle between the sample surface normal and the trace of the GB plane (Figure 4.11(a)). α can be manually assessed using the plan view image captured by scanning electron microscopy (SEM), as shown in Figure 4.11(b). It is worth noting that x_1- direction in the plan-view image should be aligned with the loading axis. Cross-sectional analysis of the grain boundary is performed to obtain the grain boundary plane angle, as shown in Figure 4.11(c). A focused ion beam (FIB) is used to lift out a region of material perpendicular to the grain boundary line on the sample surface, and the angle β is manually measured for the different GBs. Table 4.5 summarizes the measured α and β angles for the seven different GBs studied in this work.

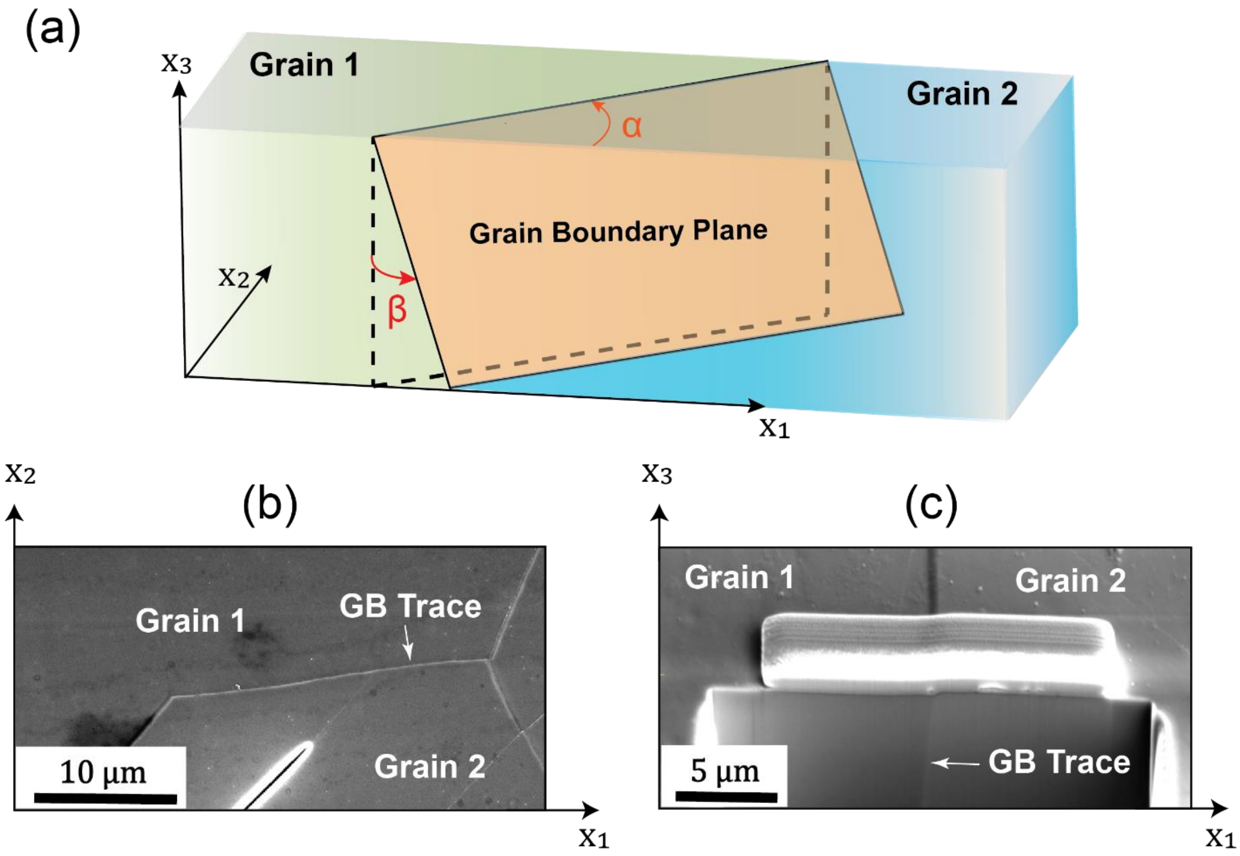

Figure 4.11 (a) Schematic representation of the GB plane. (c) The GB trace angle (α) is measured using the GB's plan view image (SEM image). (e) The GB plane angle (β) is measured using a cross-section of the GB after FIB removal of adjacent material.

Table 4.5 List of the trace angle (α) and the plane angle (β) of the different GBs investigated in this study

GB ID	1	2	3	4	5	6	7
α (°)	176.18	113.03	10.71	149.23	102.42	73.67	7.41
β (°)	127.35	87.16	55.16	62.26	49.34	76.96	90.11

4.4.2.2 Grain neighborhood simulations

Simulations were conducted on GB neighborhoods for seven GB cases with two boundary conditions, as described in Section 4.2.2.4. Figure 4.12 depicts the variation of accumulated slip for the 3 basal and 3 prismatic slip systems for a particular GB neighborhood represented by the microstructure in Figure 4.6, for BC#1. As expected, profuse basal slip is observed in most regions of the microstructure section, and particularly in the grains not containing the notch. It is interesting to observe significant prismatic slip (relative to basal slip) in the grain containing a notch close to both notch ends. This affirms to some extent the experimental observation of a slip band emanating from the notch coincident with the trace of a prismatic plane, parallel to the trace of the notch. In this particular case, the alignment of the notch corresponds to that of the $[1\bar{2}10](10\bar{1}0)$ prismatic system. Figure 4.12(d) depicts the accumulated slip variation of the $[1\bar{2}10](10\bar{1}0)$ prismatic system, where a diffuse localization of accumulated slip can be observed. This could perhaps denote a representation of sharper slip localization observed in the experiment since one of the directions in which the accumulated slip localizes in the simulations is parallel to the trace of the notch. Figure 4.14(a) is a discrete map denoting the slip system ID (Table 4.6) with the most accumulated slip at each element of the FE mesh, with Figure 4.14(b) zooming in on the region around the notch from which the slip band emanates. The dominance of $[1\bar{2}10](10\bar{1}0)$ prismatic activity is apparent.

Figure 4.13 depicts the variation of accumulated slip for the 3 basal and 3 prismatic slip systems of the same microstructure for BC#2, where one can observe more profuse basal slip and relatively lower prismatic slip in the microstructure as compared to BC#1. However, it continues to demonstrate significant prismatic slip activity close to the notch, particularly for the $[1\bar{2}10](10\bar{1}0)$ prismatic system. Figure 4.14(c) is a discrete map denoting the slip system ID with the most accumulated slip at each element of the FE mesh for BC#2, with Figure 4.14(b) zooming in on the region around the notch from which the slip band emanates. The conclusions remain the same as for BC#1, with the $[1\bar{2}10](10\bar{1}0)$ prismatic system being dominant in terms of accumulated slip.

Another interesting observation is the activation of all the prismatic systems in the vicinity of the notch for both boundary conditions (Figure 4.14(b) and 4.14(d)), irrespective of the direction of the notch. This is most likely caused by significant changes in the in-plane stress state around the notch due to the combined effect of the traction-free boundary and notch curvature. This entire exercise essentially demonstrates the effectiveness of such simple crystal plasticity models in predicting slip localizations in agreement with experimental observations. Additionally, it showcases the need to simulate only a very local neighborhood of the GB (about 10 grains) to make these predictions which are noteworthy considering performing inexpensive simulations which garner essential information.

The slip system ID map in Figure 4.14 is now used to obtain the potential outgoing slip system. In this case, the potential outgoing slip system is chosen as the one with the most accumulated slip in the vicinity of the slip trace-GB intersection (Figure 4.14(b) and 4.14(d)). For the present case, the neighborhood of this intersection for BC#1 presents two possibilities – slip system ID 2 and 3. In case of multiple possibilities, the slip system representing the majority of the grain in the slip system ID map is chosen, which in this case is ID 2. Similarly, slip system ID 2 is considered the potential outgoing slip system for BC#2 as well. Table 4.7 lists the incoming slip system (from slip trace) and potential outgoing slip system predicted by CPFE, along with some of the relevant angles characterizing the GB and the slip system-GB pair.

Table 4.6 List of slip direction and slip plane orientations for different slip/twin systems for Mg alloys.

Slip/Twin System	**ID**	**Slip Direction**	**Slip Plane**
Basal	1	$[11\bar{2}0]$	(0001)
	2	$[\bar{2}110]$	(0001)
	3	$[1\bar{2}10]$	(0001)
Prismatic<a>	4	$[1\bar{2}10]$	$(10\bar{1}0)$
	5	$[2\bar{1}\bar{1}0]$	$(01\bar{1}0)$
	6	$[11\bar{2}0]$	$(\bar{1}100)$
Pyramidal<c+a>	7	$[\bar{1}\bar{1}23]$	$(11\bar{2}2)$
	8	$[1\bar{2}13]$	$(\bar{1}2\bar{1}2)$
	9	$[2\bar{1}\bar{1}3]$	$(\bar{2}112)$
	10	$[11\bar{2}3]$	$(\bar{1}\bar{1}22)$
	11	$[\bar{1}2\bar{1}3]$	$(1\bar{2}12)$
	12	$[\bar{2}113]$	$(2\bar{1}\bar{1}2)$

Twin<c + a>	13	$[\bar{1}011]$	$(10\bar{1}2)$
	14	$[10\bar{1}1]$	$(\bar{1}012)$
	15	$[\bar{1}101]$	$(1\bar{1}02)$
	16	$[1\bar{1}01]$	$(\bar{1}102)$
	17	$[0\bar{1}11]$	$(01\bar{1}2)$
	18	$[01\bar{1}1]$	$(0\bar{1}12)$

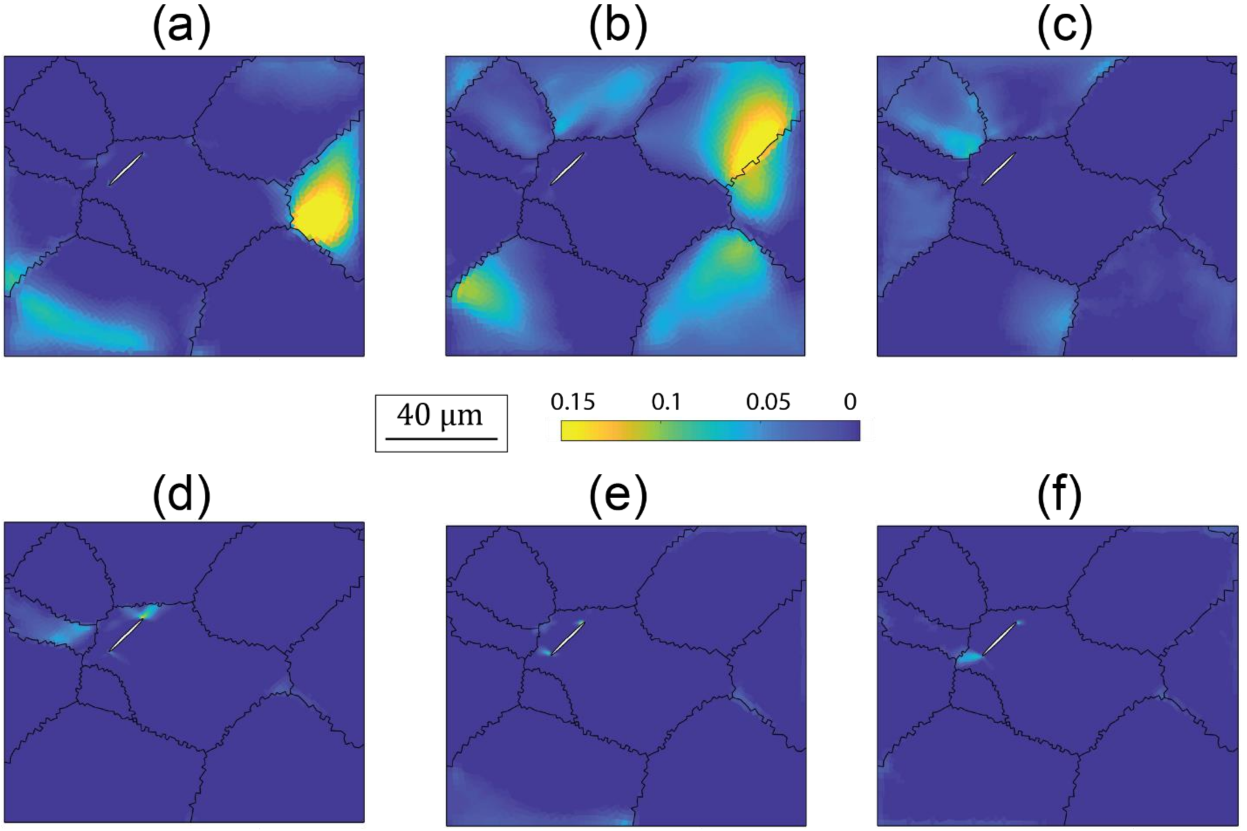

Figure 4.12 Boundary Condition 1: (a) Accumulated slip for Basal 1, (b) Accumulated slip for Basal 2, (c) Accumulated slip for Basal 3, (d) Accumulated slip for Prismatic 1, (e) Accumulated slip for Prismatic 2, and (f) Accumulated slip for Prismatic 3. It can be observed that prismatic slip is particularly dominant in the neighborhood of the notches on either side.

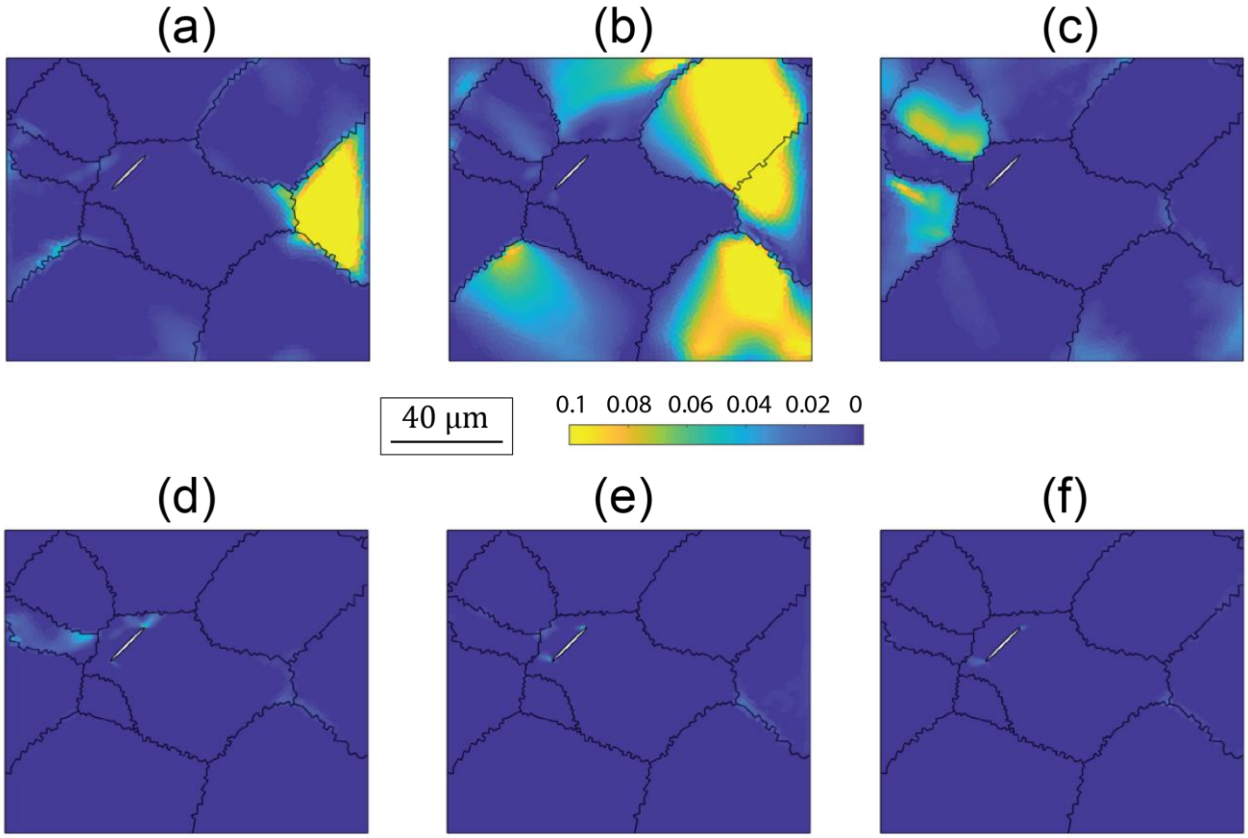

Figure 4.13 Boundary Condition 2: (a) Accumulated slip for Basal 1, (b) Accumulated slip for Basal 2, (c) Accumulated slip for Basal 3, (d) Accumulated slip for Prismatic 1, (e) Accumulated slip for Prismatic 2, and (f) Accumulated slip for Prismatic 3. It can be observed that prismatic slip is particularly dominant in the neighborhood of the notches on either side.

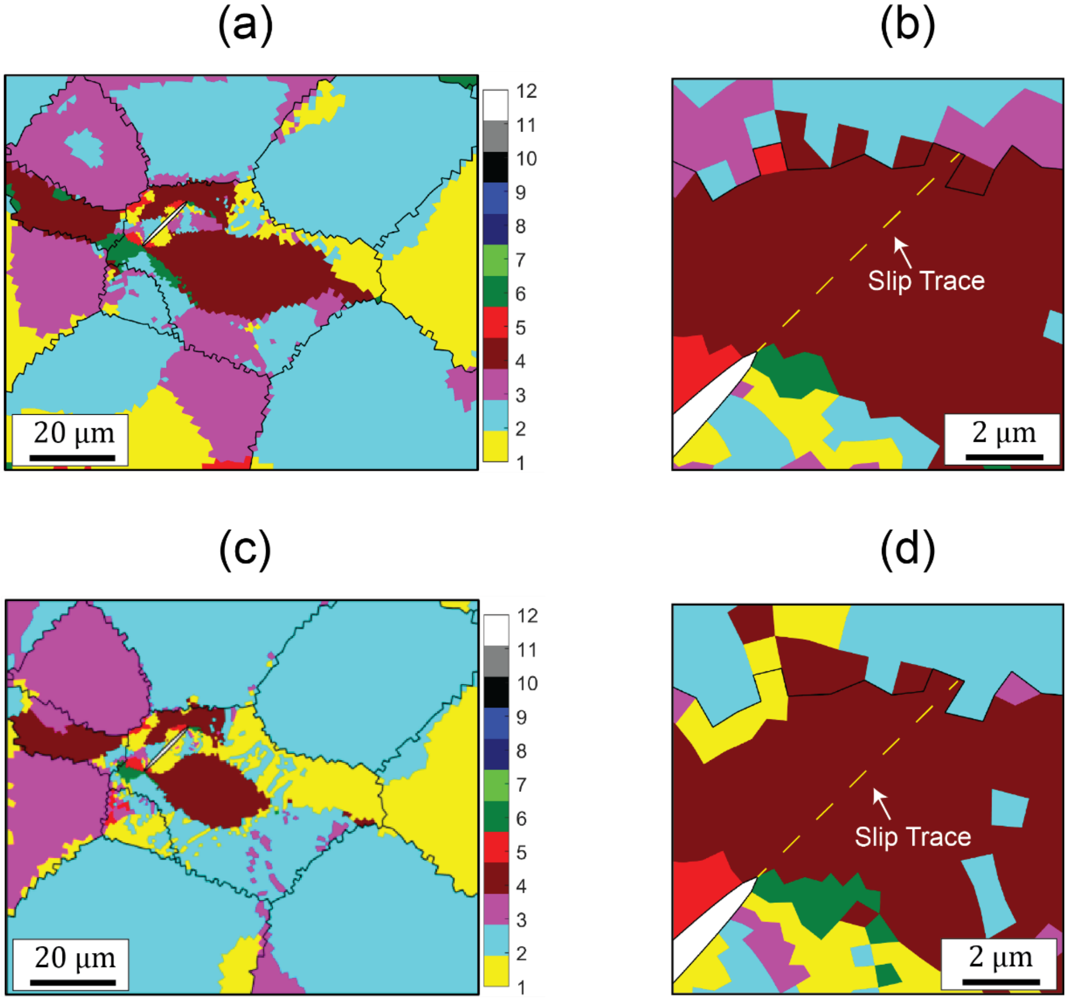

Figure 4.14 Visualization of most active slip system for all elements of the microstructure, corresponding to GB ID 3, included in Table 4.7. The numbers in the color bar correspond to the slip system IDs in Table 4.6. The most active slip system in every element is recognized as the one with the highest accumulated slip within the element. The basal and prismatic <a> slip systems dominate in slip activity for both boundary conditions considered. (a) BC#1 – Most active slip system map (b) Close-up with prismatic slip trace superposed, (c) BC#2 – Most active slip system map (d) Close-up with prismatic slip trace superposed. For both BC#1 and BC#2, the incoming slip system is $(10\bar{1}0)[1\bar{2}10]$ and the potential outgoing slip system is $(0001)[\bar{2}110]$.

4.4.3 Estimation of micro-Hall-Petch Coefficient as a Function of Grain-Boundary Parameters

Table 4.7 and Table 4.8 summarize the slip systems of the observed prismatic slip band generated from the micro-notch and the potential outgoing slip systems under BC#1 and BC#2 for each individual grain boundary, respectively. The relevant angles (θ, κ, ψ, δ) are calculated and listed in these tables for each GB case.

Table 4.7 List of the incoming prismatic slip system and the potential outgoing slip system of each grain boundary under BC#1, and the relevant angles ($\theta, \kappa, \psi, \delta$) describing the prismatic slip band interaction with each grain boundary.

GB ID	**Incoming Slip System**	**Potential Outgoing Slip System**	**θ (°)**	**κ (°)**	**ψ (°)**	**δ (°)**
1	$(01\bar{1}0)[2\bar{1}\bar{1}0]$	$(0001)[\bar{2}110]$	74.73	69.94	63.26	27.48
2	$(01\bar{1}0)[2\bar{1}\bar{1}0]$	$(10\bar{1}0)[1\bar{2}10]$	65.74	88.33	88.35	9.64
3	$(10\bar{1}0)[1\bar{2}10]$	$(0001)[\bar{2}110]$	80.95	70.06	65.53	26.67
4	$(\bar{1}100)[11\bar{2}0]$	$(0001)[1\bar{2}10]$	79.26	42.34	53.72	49.29
5	$(10\bar{1}0)[1\bar{2}10]$	$(0001)[11\bar{2}0]$	47.36	36.59	40.92	59.65
6	$(01\bar{1}0)[2\bar{1}\bar{1}0]$	$(01\bar{1}0)[2\bar{1}\bar{1}0]$	43.92	31.10	22.73	86.94
7	$(01\bar{1}0)[2\bar{1}\bar{1}0]$	$(0001)[\bar{2}110]$	87.95	70.54	72.79	58.48

Table 4.8 List of the incoming prismatic slip system and the potential outgoing slip system of each grain boundary under BC#2, and the relevant angles (θ,κ,ψ, δ) describing the prismatic slip band interaction with each grain boundary.

GB ID	**Incoming Slip System**	**Potential Outgoing Slip System**	**θ (°)**	**κ (°)**	**ψ (°)**	**δ (°)**
1	$(01\bar{1}0)[2\bar{1}\bar{1}0]$	$(0001)[\bar{2}110]$	65.89	69.94	63.26	27.48
2	$(01\bar{1}0)[2\bar{1}\bar{1}0]$	$(10\bar{1}0)[1\bar{2}10]$	70.22	88.33	88.35	9.64
3	$(10\bar{1}0)[1\bar{2}10]$	$(0001)[\bar{2}110]$	80.95	70.06	65.53	26.67
4	$(\bar{1}100)[11\bar{2}0]$	$(0001)[\bar{2}110]$	79.26	59.01	53.72	49.29
5	$(10\bar{1}0)[1\bar{2}10]$	$(0001)[1\bar{2}10]$	47.36	47.53	40.92	59.65
6	$(01\bar{1}0)[2\bar{1}\bar{1}0]$	$(01\bar{1}0)[2\bar{1}\bar{1}0]$	43.92	31.10	22.73	86.94
7	$(01\bar{1}0)[2\bar{1}\bar{1}0]$	$(0001)[\bar{2}110]$	87.95	70.54	72.79	58.48

The prismatic micro-Hall-Petch coefficient values (Table 4.4) are plotted versus the corresponding θ, the angle between the two slip plane traces on the grain boundary plane (Figure 4.15(a) for BC#1, Figure 4.16(a) for BC#2); versus κ, the angle between incoming and outgoing slip directions (Figure 4.15(b) for BC#1, Figure 4.16(b) for BC#2); versus δ, the angle between the incoming slip direction and the intersection of the incoming slip plane with the grain boundary plane (Figure 4.15(c) for BC#1, Figure 4.16(c) for BC#2); and versus ψ, the angle between slip plane normals (Figure 4.15(d) for BC#1, Figure 4.16(d) for BC#2). The coefficient of determination, the R-squared value (0< R^2 <1), is used to quantify and compare the correlation between each of the geometrical expression angles and the micro-Hall-Petch coefficient (as shown in each plot). The linear regression is stronger at higher values of R^2.

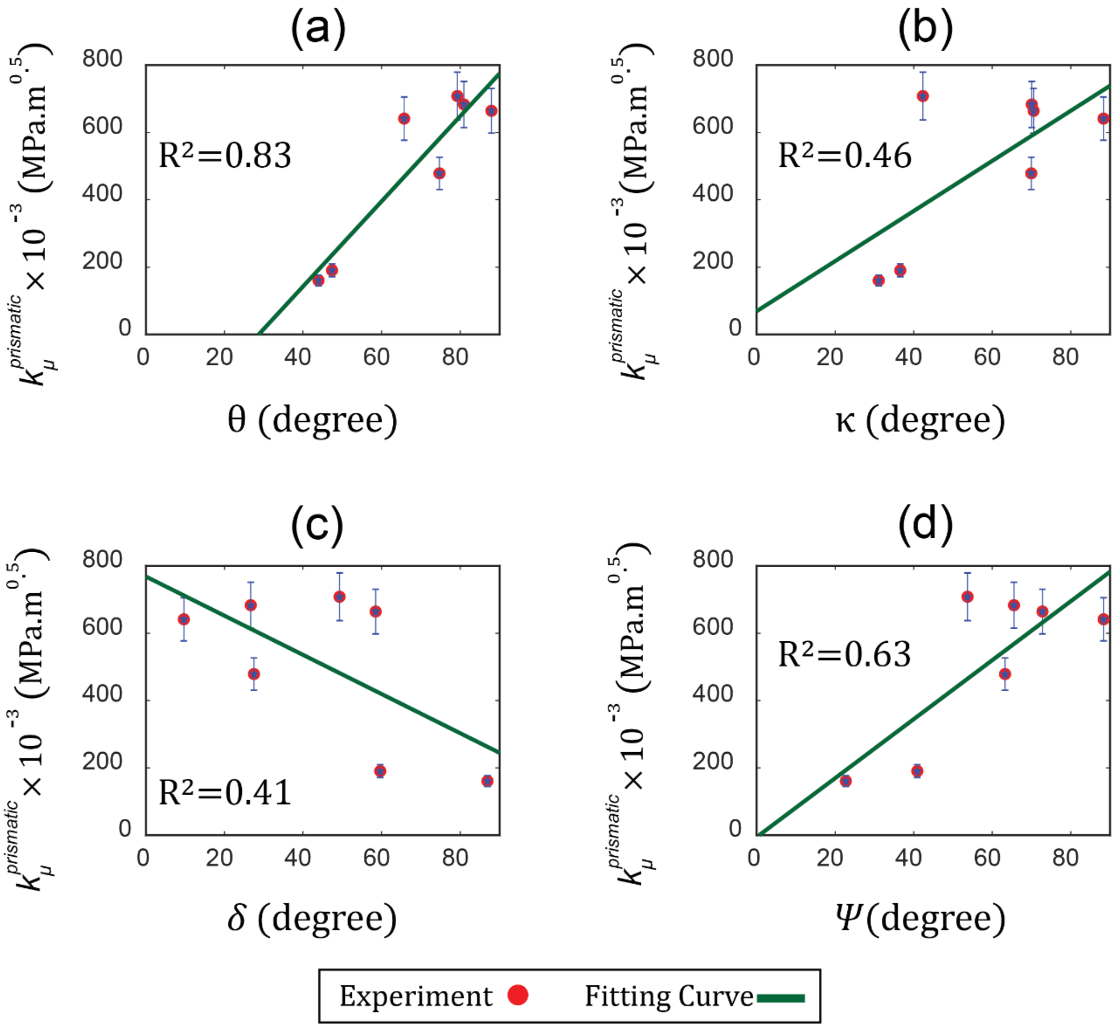

Figure 4.15 The prismatic micro-Hall-Petch coefficient values relevant angles (θ, κ, ψ, δ) calculated based on BC#1. (a) $k_\mu^{prismatic}$ vs the angle between the two slip plane intersections with the GB (θ). (b) $k_\mu^{prismatic}$ vs the Angle between incoming and outgoing slip directions (κ). (c) $k_\mu^{prismatic}$ vs the angle between slip plane normal (ψ). (d) $k_\mu^{prismatic}$ vs the angle between the incoming slip direction and the incoming slip plane trace on the GB plane (δ).

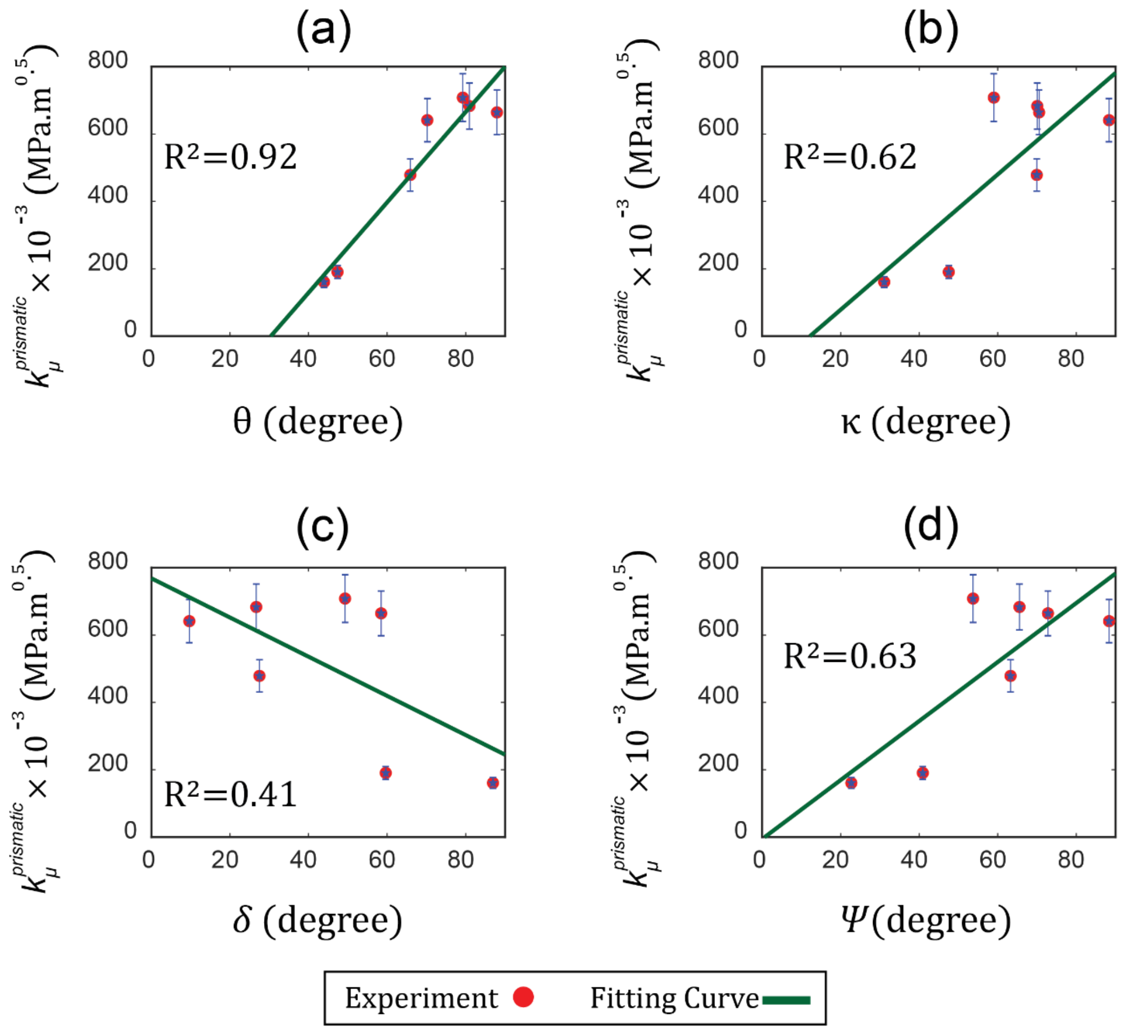

Figure 4.16 $k_\mu^{prismatic}$ values against relevant angles (θ, κ, ψ, δ) calculated based on BC#2. (a) $k_\mu^{prismatic}$ vs the angle between the two slip plane intersections with the GB (θ). (b) $k_\mu^{prismatic}$ vs the angle between incoming and outgoing slip directions (κ). (c) $k_\mu^{prismatic}$ vs the angle between slip plane normal (ψ). (d) $k_\mu^{prismatic}$ vs the angle between the incoming slip direction and the incoming slip plane trace on the GB plane (δ).

4.5 Discussion

Prismatic slip band pile-ups at seven different GBs (Table 4.1) were studied using a combination of HR-EBSD, dislocation pile-up theory, and CPFE simulations. The grains with the highest Schmid factor for the prismatic slip system and the lowest Schmid factor for the basal slip were selected. A series of micro-FIB notches (Figure 4.3) parallel to the prismatic slip plane was machined in the grains to act as initiation sites for the prismatic slip bands. The resolved shear stress field ahead of the pile-up was measured using HR-EBSD approach (Figure 4.8), and the resulting stress profiles were fit to the expressions from a dislocation pile-up model to assess the micro-Hall-Petch coefficient for each individual GB (Table 4.4). The calculated $k_{\mu}^{prismatic}$ values vary from 0.138 $\mathrm{MPa.m^{1/2}}$ to 0.665 $\mathrm{MPa.m^{1/2}}$ which are almost three times larger than the calculated values for the k_{μ}^{basal} (0.054 $\mathrm{MPa.m^{1/2}}$ $-$ 0.184 $\mathrm{MPa.m^{1/2}}$) [29]. In our phenomenological model, since the applied resolved shear stress equilibrating a pile-up is assumed to be a Hall-Petch type relation, $k_{\mu}^{prismatic}$ values already subsume the higher critical stress for prismatic slip compared to basal. This expectation is also consistent with experimental Hall-Petch constants for textures with prismatic + basal slip being higher than when primarily basal slip is present [21, 55, 56].

To understand the role of grain boundaries in the observed variation of $k_{\mu}^{prismatic}$, the relevant angles ($\theta, \kappa, \psi, \delta$) for each individual GB was calculated. First, cross-sectional analysis of the GBs was performed by FIB to provide 3-D insights of the GBs plane, as summarized in Table 4.5. Then, CPFE modeling of each GB and the surrounding microstructure in the presence of micro-FIB notches under two different boundary conditions were used to predict the potential outgoing slip system (Table 4.7 and Table 4.8). The $k_{\mu}^{prismatic}$ values were plotted against the relevant geometric quantities involving the angles (θ,κ,ψ, δ) for both boundary conditions (Figure 4.15 and Figure 4.16) and the results are evaluated using R^2 values. In both boundary conditions, the plots of $k_{\mu}^{prismatic}$ values against the angle between the two slip plane intersections with the GB (θ) have the highest R^2 values (Figure 4.15(a) and Figure 4.16(a)), which is implying the critical role of the GB plane in estimating the prismatic micro-Hall-Petch coefficient. A similar observation was reported in our previous work [29], in the case of k_{μ}^{basal} and its strong correlation with θ. This observation can be interpreted by the model presented by Davis [57] where it was shown that the energy barrier of each individual GB for stepped dislocation formation is proportional to $\sin(\theta)$.

The angle between the slip directions (κ), which was reported as the second most effective angle in determining basal micro-Hall-Petch in the previous work [29], shows a considerable correlation with $k_{\mu}^{prismatic}$ values ((Figure 4.15(b) and Figure 4.16(b)). It is well known that the magnitude of residual Burgers vectors in slip transmission is proportional to κ angle and used as a criterion to evaluate the strength of each individual GB against slip transmission [58-61].

Although, the angle between the incoming slip direction and the intersection of the incoming slip plane with the GB plane (δ), and the angle between slip plane normals (ψ), show a correlation with the $k_{\mu}^{prismatic}$ values ((Figure 4.15(c), Figure 4.15(d), Figure 4.16(c), and Figure 4.16(d)), they are not as informative about slip transmission and GB as the other two angles. δ does not capture the outgoing slip system and its grain information and ψ does not include any information about grain boundary plane orientations.

To consider both θ and κ angles in the estimation of the $k_{\mu}^{prismatic}$, the following equation is proposed:

$$k_{\mu}^{prismatic} = K^{prismatic}(1-\cos(\theta)\cos(\kappa))^{c} \;\; ; c > 0 \tag{4.18}$$

where $K^{prismatic}$ and c are model parameters. A similar relationship was proposed for the estimation of k_{μ}^{basal}[29]. The model was proposed based on the slip transmission criteria developed by Lee–Robertson–Birnbaum[62-64], where the factor cos(θ)cos(κ) was used to estimate the outgoing slip systems.

$k_{\mu}^{prismatic}$ values (Table 4.4) were fit with Equation 4.18 under both boundary conditions (Figure 4.17). The model parameters under BC#1 (Table 4.7) and BC#2 (Table 4.8) are obtained as $K^{prismatic} = 0.680 \pm 0.07 \text{ MPa.m}^{\mathbf{1/2}}$ and c = 1.55 under BC#1, and $K^{prismatic} = 0.687 \pm 0.07 \text{ MPa.m}^{\mathbf{1/2}}$ and c = 1.83 under BC#2. Substituting Equation 4.18 in Equation 4.5 yields an expression for the slip resistance of prismatic slip systems as follows:

$$\tau^{prismatic} = \tau_{0}^{prismatic} + \frac{K^{prismatic}(1-\cos(\theta)\cos(\kappa))^{c}}{\sqrt{2a}} \tag{4.19}$$

with the effect of texture and microstructural size taken into account. Along with a similar expression proposed for the basal slip in earlier work [29], this provides avenues to capture texture-grain size coupling for Mg alloys. It is worthwhile to note that the entire procedure developed in this work can be extended to any alloy system and is particularly important when there is significant plastic anisotropy arising from the underlying crystallography.

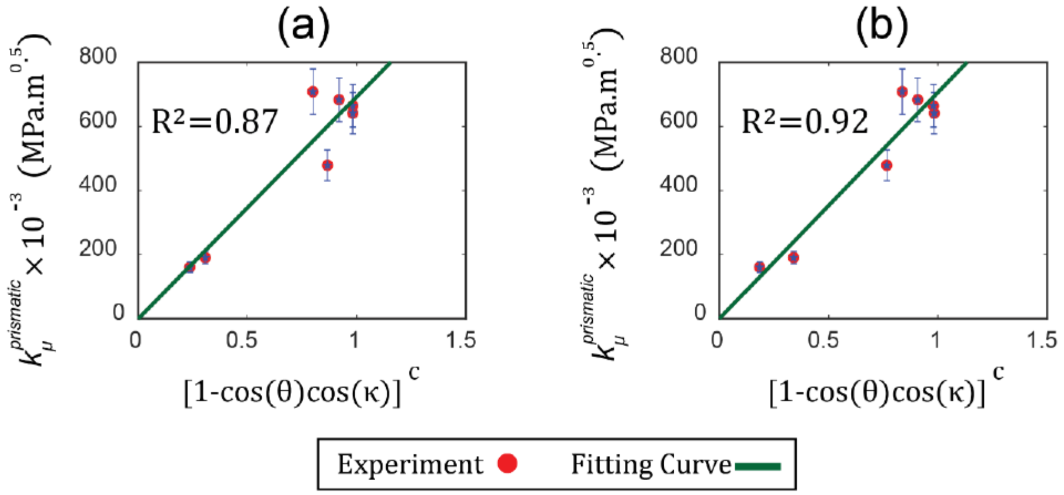

Figure 4.17 $k_{\mu}^{prismatic}$ values against $(1 - \cos(\theta)\cos(\kappa))^c$ based on (a) BC#1 and (b) BC#2.

The dependence of the micro-Hall-Petch coefficient for different slip systems on grain boundary metrics can be used as inputs to CPFE simulations, which can simulate the coupling between texture and grain-size effect. It is important to note that these simulations often involve 3-D synthetic microstructures generated based on input statistics which either don't provide grain boundary inclinations due to a voxelated mesh (like in DREAM.3D) or where grain boundary conforming meshes are generated with flat grain boundaries and not curved boundaries (like in Neper). As an alternative, one can use the angles κ and ψ to construct the compatibility factor $\cos(\psi)\cos(\kappa)$. Figure 4.18 depicts $k_{\mu}^{prismatic}$ values against $(1 - \cos(\psi)\cos(\kappa))^c$ with $K^{prismatic} = 0.689 \pm 0.07\ \mathrm{MPa.m}^{\mathbf{1/2}}$ and c = 0.85 under BC#1, and $K^{prismatic} = 0.699 \pm 0.07\ \mathrm{MPa.m}^{\mathbf{1/2}}$ and c = 1.07 under BC#2. This functional form can be used in CP modeling where each slip system and material point pair in the microstructure is assigned a slip-system level grain size (calculate from microstructural position data) and micro-Hall-Petch coefficient (using the functional form in Equation 4.18). This is the subject of study in our upcoming work, where the proposed model is input into a CPFE framework to study texture-grain size coupling.

From the perspective of modeling the microstructural slices, it is to be noted that the slip band is not explicitly modeled, but the stress concentration at the notch is used to naturally initiate prismatic slip in the vicinity. Alternatively, the slip band itself can be explicitly modeled in CPFE using softening-based models [65-67] or using more recent crystal plasticity peridynamics (CPPD) models [68-70] where localizations are a natural consequence of non-local interactions. These approaches can capture the existence of localization bands more in line with experimental observations.

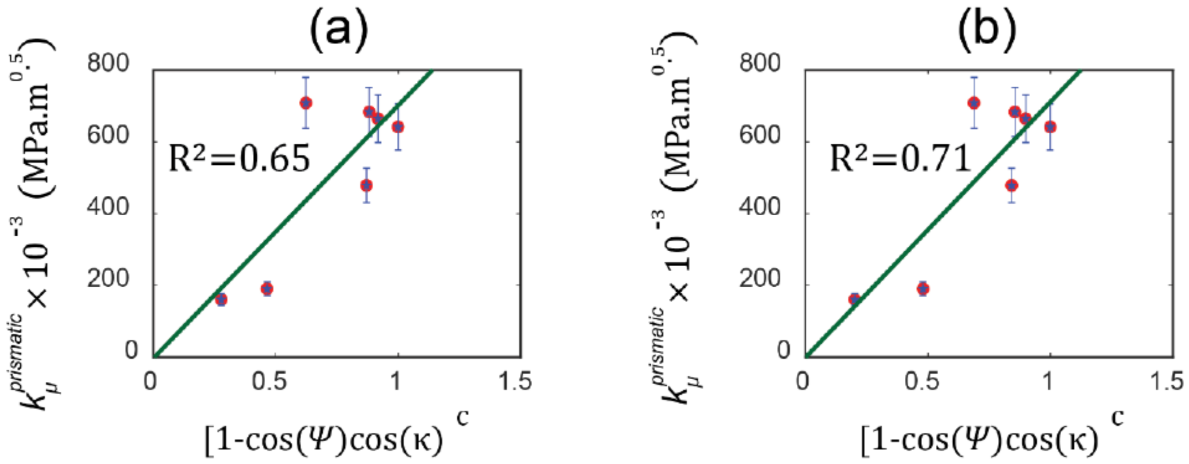

Figure 4.18 The prismatic slip system micro-Hall-Petch coefficients $(k_\mu^{prismatic})$ for the seven-cases are plotted against the factor $(1-\cos(\psi)\cos(\kappa))^c$ based on (a) BC#1 and (b) BC#2.

4.6 Conclusions

- An experimental method was developed to initiate the prismatic slip in the form of the localized band at low-stress levels in Mg-4Al. A series of sharp micro-notches parallel to the prismatic slip plane in specific grains were machined to act as slip initiation sites due to stress concentration and subsequent plasticity accommodation in front of a notch.

- A one-dimensional continuum dislocation pile-up model, coupled with the micro-Hall-Petch phenomenological model, was used to estimate the micro-Hall-Petch coefficient for prismatic slip from pile-up stress data.
- The resolved shear stress ahead of blocked prismatic slip bands at seven different grain boundaries in Mg-4Al was measured using HR-EBSD method. The calculated $k_{\mu}^{prismatic}$ values vary from 0.138 $\mathrm{MPa.m}^{\mathbf{1/2}}$ to 0.665 $\mathrm{MPa.m}^{\mathbf{1/2}}$ which are almost three times larger than the calculated values for the k_{μ}^{basal} (0.054 $\mathrm{MPa.m}^{\mathbf{1/2}}$ –0.184 $\mathrm{MPa.m}^{\mathbf{1/2}}$).
- Crystal plasticity simulations of microstructure slices for different GB cases were performed to inform the potential outgoing slip system, required to construct geometric expressions and ascribe $k_{\mu}^{prismatic}$ values to dependence on these quantities.
- The $k_{\mu}^{prismatic}$ values were correlated with the geometric descriptors of the GBs, and it was concluded that the angle between the two slip plane traces on the GB plane (θ), and the angle between slip directions (κ) were the two most effective geometric parameters in estimating the magnitude of $k_{\mu}^{prismatic}$. A relationship, $k_{\mu}^{prismatic} = K^{prismatic}(1 - \cos(\theta)\cos(\kappa))^{c}$, was suggested including both of these angles to estimate the slip system level Hall-Petch slope for prismatic slip system, and the model parameters, $K^{prismatic}$ and c, were calibrated for Mg-4Al alloys.

4.7 References

1. Easton, M., et al., *Magnesium alloy applications in automotive structures.* Jom, 2008. **60**(11): p. 57-62.
2. Landkof, B., *Magnesium applications in aerospace and electronic industries.* Magnesium Alloys and their Applications, 2000: p. 168-172.
3. Zhang, E., et al., *Microstructure, mechanical and corrosion properties and biocompatibility of Mg–Zn–Mn alloys for biomedical application.* Materials Science and Engineering: C, 2009. **29**(3): p. 987-993.
4. Riaz, U., I. Shabib, and W. Haider, *The current trends of Mg alloys in biomedical applications—A review.* Journal of Biomedical Materials Research Part B: Applied Biomaterials, 2019. **107**(6): p. 1970-1996.
5. Yuan, W., et al., *Influence of grain size and texture on Hall–Petch relationship for a magnesium alloy.* Scripta Materialia, 2011. **65**(11): p. 994-997.
6. Yu, H., et al., *Hall-Petch relationship in Mg alloys: a review.* Journal of Materials Science & Technology, 2018. **34**(2): p. 248-256.
7. Stanford, N., et al., *Effect of plate-shaped particle distributions on the deformation behaviour of magnesium alloy AZ91 in tension and compression.* Acta materialia, 2012. **60**(1): p. 218-228.
8. Nie, J.-F., *Precipitation and hardening in magnesium alloys.* Metallurgical and Materials Transactions A, 2012. **43**(11): p. 3891-3939.
9. Robson, J.D., N. Stanford, and M.R. Barnett, *Effect of precipitate shape on slip and twinning in magnesium alloys.* Acta materialia, 2011. **59**(5): p. 1945-1956.
10. Ma, X., et al., *Effect of basal precipitates on extension twinning and pyramidal slip: A micro-mechanical and electron microscopy study of a Mg–Al binary alloy.* Acta Materialia, 2020. **189**: p. 35-46.
11. Singh, A., et al., *Quasicrystal strengthened Mg–Zn–Y alloys by extrusion.* Scripta Materialia, 2003. **49**(5): p. 417-422.
12. Wu, B., et al., *Ductility enhancement of extruded magnesium via yttrium addition.* Materials Science and Engineering: A, 2010. **527**(16-17): p. 4334-4340.
13. Sandlöbes, S., et al., *Ductility improvement of Mg alloys by solid solution: Ab initio modeling, synthesis and mechanical properties.* Acta Materialia, 2014. **70**: p. 92-104.
14. Guan, B., et al., *Quantitative prediction of texture effect on Hall–Petch slope for magnesium alloys.* Acta Materialia, 2019. **173**: p. 142-152.
15. Yang, Q. and A. Ghosh, *Deformation behavior of ultrafine-grain (UFG) AZ31B Mg alloy at room temperature.* Acta materialia, 2006. **54**(19): p. 5159-5170.
16. Hall, E., *The deformation and ageing of mild steel: III discussion of results.* Proceedings of the Physical Society. Section B, 1951. **64**(9): p. 747.
17. Armstrong, R.W., *60 years of Hall-Petch: past to present nano-scale connections.* Materials Transactions, 2014. **55**(1): p. 2-12.
18. Petch, N., *The cleavage strength of polycrystals.* Journal of the Iron and Steel Institute, 1953. **174**: p. 25-28.
19. Armstrong, R.W., *Hall–Petch k dependencies in nanopolycrystals.* Emerging Materials Research, 2014. **3**(6): p. 246-251.

20. Wang, Y. and H. Choo, *Influence of texture on Hall–Petch relationships in an Mg alloy.* Acta Materialia, 2014. **81**: p. 83-97.
21. Wang, Y., et al., *Texture and weak grain size dependence in friction stir processed Mg–Al–Zn alloy.* Scripta Materialia, 2006. **55**(7): p. 637-640.
22. Yu, H., et al., *The mechanism for the high dependence of the Hall-Petch slope for twinning/slip on texture in Mg alloys.* Acta Materialia, 2017. **128**: p. 313-326.
23. Liu, J., et al., *Mean-field polycrystal plasticity modeling with grain size and shape effects for laser additive manufactured FCC metals.* International Journal of Solids and Structures, 2017. **112**: p. 35-42.
24. Sun, S. and V. Sundararaghavan, *A probabilistic crystal plasticity model for modeling grain shape effects based on slip geometry.* Acta Materialia, 2012. **60**(13-14): p. 5233-5244.
25. Weng, G., *A micromechanical theory of grain-size dependence in metal plasticity.* Journal of the Mechanics and Physics of Solids, 1983. **31**(3): p. 193-203.
26. Ravaji, B. and S.P. Joshi, *A crystal plasticity investigation of grain size-texture interaction in magnesium alloys.* Acta Materialia, 2021. **208**: p. 116743.
27. Singh, A., et al., *Effect of microstructure on strength and ductility of high strength quasicrystal phase dispersed Mg–Zn–Y alloys.* Materials Science and Engineering: A, 2014. **611**: p. 242-251.
28. Andani, M.T., et al., *A quantitative study of stress fields ahead of a slip band blocked by a grain boundary in unalloyed magnesium.* Scientific reports, 2020. **10**(1): p. 1-8.
29. Andani, M.T., et al., *Quantitative study of the effect of grain boundary parameters on the slip system level Hall-Petch slope for basal slip system in Mg-4Al.* Acta Materialia, 2020. **200**: p. 148-161.
30. Murphy-Leonard, A., *The Effects Of Alloying And Grain Size On Fatigue Life Behavior, Cyclic Stress-Strain Behavior, and Microstructural Evolution of Unalloyed Mg and A Mg-Al Alloy*. 2018.
31. Bachmann, F., R. Hielscher, and H. Schaeben. *Texture analysis with MTEX–free and open source software toolbox*. in *Solid State Phenomena*. 2010. Trans Tech Publ.
32. Bachmann, F., R. Hielscher, and H. Schaeben, *Grain detection from 2d and 3d EBSD data—Specification of the MTEX algorithm.* Ultramicroscopy, 2011. **111**(12): p. 1720-1733.
33. Wilkinson, A.J., G. Meaden, and D.J. Dingley, *High-resolution elastic strain measurement from electron backscatter diffraction patterns: new levels of sensitivity.* Ultramicroscopy, 2006. **106**(4-5): p. 307-313.
34. Britton, T. and A.J. Wilkinson, *High resolution electron backscatter diffraction measurements of elastic strain variations in the presence of larger lattice rotations.* Ultramicroscopy, 2012. **114**: p. 82-95.
35. Yaghoobi, M., et al., *PRISMS-Plasticity: An open-source crystal plasticity finite element software.* Computational Materials Science, 2019. **169**: p. 109078.
36. Bilby, B.A., A.H. Cottrell, and K. Swinden, *The spread of plastic yield from a notch.* Proceedings of the Royal Society of London. Series A. Mathematical and Physical Sciences, 1963. **272**(1350): p. 304-314.
37. Taira, S., K. Tanaka, and Y. Nakai, *A model of crack-tip slip band blocked by grain boundary.* Mechanics Research Communications, 1978. **5**(6): p. 375-381.

38. Shiue, S.T. and S. Lee, *The effect of grain size on fracture: Dislocation-free zone in the front of the finite crack tip.* Journal of applied physics, 1991. **70**(6): p. 2947-2953.
39. Muskhelishvili, N.I. and J.R.M. Radok, *Singular integral equations: boundary problems of function theory and their application to mathematical physics*. 2008: Courier Corporation.
40. Zhao, C., et al., *Strain Hardening Behavior in Mg–Al Alloys at Room Temperature.* Advanced Engineering Materials, 2019. **21**(3): p. 1801062.
41. Kröner, E., *Allgemeine kontinuumstheorie der versetzungen und eigenspannungen.* Archive for Rational Mechanics and Analysis, 1959. **4**(1): p. 273-334.
42. Lee, E.H., *Elastic-plastic deformation at finite strains.* 1969.
43. Asaro, R.J. and A. Needleman, *Overview no. 42 texture development and strain hardening in rate dependent polycrystals.* Acta metallurgica, 1985. **33**(6): p. 923-953.
44. Anand, L., *Constitutive equations for hot-working of metals.* International Journal of Plasticity, 1985. **1**(3): p. 213-231.
45. Kalidindi, S.R., C.A. Bronkhorst, and L. Anand, *Crystallographic texture evolution in bulk deformation processing of FCC metals.* Journal of the Mechanics and Physics of Solids, 1992. **40**(3): p. 537-569.
46. Yaghoobi, M., et al., *PRISMS-Fatigue computational framework for fatigue analysis in polycrystalline metals and alloys.* npj Computational Materials, 2021. **7**(1): p. 1-12.
47. Lakshmanan, A.Y., M.; Stopka, K.S.; Sundararaghavan, V. Crystal Plasticity Finite Element Modeling of Grain Size and Morphology Effects (Submitted).
48. Groeber, M.A. and M.A. Jackson, *DREAM. 3D: a digital representation environment for the analysis of microstructure in 3D.* Integrating materials and manufacturing innovation, 2014. **3**(1): p. 56-72.
49. Long, T. and C.S. Smith, *Single-crystal elastic constants of magnesium and magnesium alloys.* Acta Metallurgica, 1957. **5**(4): p. 200-207.
50. Slutsky, L.J. and C. Garland, *Elastic constants of magnesium from 4.2 K to 300 K.* Physical Review, 1957. **107**(4): p. 972.
51. Zhang, J. and S.P. Joshi, *Phenomenological crystal plasticity modeling and detailed micromechanical investigations of pure magnesium.* Journal of the Mechanics and Physics of Solids, 2012. **60**(5): p. 945-972.
52. Geuzaine, C. and J.F. Remacle, *Gmsh: A 3-D finite element mesh generator with built-in pre-and post-processing facilities.* International journal for numerical methods in engineering, 2009. **79**(11): p. 1309-1331.
53. Britton, T.B. and A.J. Wilkinson, *Stress fields and geometrically necessary dislocation density distributions near the head of a blocked slip band.* Acta Materialia, 2012. **60**(16): p. 5773-5782.
54. Britton, T. and A. Wilkinson, *Measurement of residual elastic strain and lattice rotations with high resolution electron backscatter diffraction.* Ultramicroscopy, 2011. **111**(8): p. 1395-1404.
55. Jain, A., et al., *Grain size effects on the tensile properties and deformation mechanisms of a magnesium alloy, AZ31B, sheet.* Materials Science and Engineering: A, 2008. **486**(1-2): p. 545-555.
56. Raeisinia, B., S.R. Agnew, and A. Akhtar, *Incorporation of solid solution alloying effects into polycrystal modeling of Mg alloys.* Metallurgical and Materials Transactions A, 2011. **42**(5): p. 1418-1430.

57. Davis, K.G., *Slip continuity across grain boundaries in aluminum*. 1959, University of British Columbia.
58. Bollmann, W., *Crystal defects and crystalline interfaces*. 2012: Springer Science & Business Media.
59. Lim, L. and R. Raj, *The role of residual dislocation arrays in slip induced cavitation, migration and dynamic recrystallization at grain boundaries.* Acta Metallurgica, 1985. **33**(12): p. 2205-2214.
60. Marcinkowski, M. and W.F. Tseng, *Dislocation behavior at tilt boundaries of infinite extent.* Metallurgical Transactions, 1970. **1**(12): p. 3397-3401.
61. Lee, T., I. Robertson, and H. Birnbaum, *AnIn Situ transmission electron microscope deformation study of the slip transfer mechanisms in metals.* Metallurgical Transactions A, 1990. **21**(9): p. 2437-2447.
62. Shen, Z., R. Wagoner, and W. Clark, *Dislocation pile-up and grain boundary interactions in 304 stainless steel.* Scripta metallurgica, 1986. **20**(6): p. 921-926.
63. Shen, Z., R. Wagoner, and W. Clark, *Dislocation and grain boundary interactions in metals.* Acta metall., 1988. **36**(12): p. 3231-3242.
64. Lee, T., I. Robertson, and H. Birnbaum, *TEM in situ deformation study of the interaction of lattice dislocations with grain boundaries in metals.* Philosophical Magazine A, 1990. **62**(1): p. 131-153.
65. Marano, A., L. Gélébart, and S. Forest, *Intragranular localization induced by softening crystal plasticity: Analysis of slip and kink bands localization modes from high resolution FFT-simulations results.* Acta Materialia, 2019. **175**: p. 262-275.
66. Zhang, M., et al., *Simulation of slip band evolution in duplex Ti–6Al–4V.* Acta materialia, 2010. **58**(3): p. 1087-1096.
67. Ahmadikia, B., M.A. Kumar, and I.J. Beyerlein, *Effect of Neighboring Grain Orientation on Strain Localization in Slip Bands in HCP Materials.* International Journal of Plasticity, 2021: p. 103026.
68. Luo, J., A. Ramazani, and V. Sundararaghavan, *Simulation of micro-scale shear bands using peridynamics with an adaptive dynamic relaxation method.* International Journal of Solids and Structures, 2018. **130**: p. 36-48.
69. Lakshmanan, A., et al., *Three-dimensional crystal plasticity simulations using peridynamics theory and experimental comparison.* International Journal of Plasticity, 2021. **142**: p. 102991.
70. Gu, X., Q. Zhang, and E. Madenci, *Non-ordinary state-based peridynamic simulation of elastoplastic deformation and dynamic cracking of polycrystal.* Engineering Fracture Mechanics, 2019. **218**: p. 106568.

Chapter 5: Implementation of Micro-Hall-Petch Equation into Crystal Plasticity with Application to Mg-4Al

5.1 Abstract

This chapter presents a method to incorporate the micro Hall-Petch equation into crystal plasticity constitutive models accounting for the microstructural features to understand the coupling between grain size, texture and loading direction. A rate-dependent crystal plasticity model implemented into the open-source PRISMS-CPFE plasticity code is adopted for crystal plasticity simulations. The effect of grain size and texture is accounted for by modifying the slip resistances of individual basal and prismatic slip systems based on the micro Hall-Petch equation. This modification endows each microstructural point with a slip system-level grain size and maximum compatibility factor which are used to modify the slip resistance. Comparisons in the Hall-Petch coefficients are presented between predicted stress-strain curves using original parameters from previous work and subsequently calibrated parameters. This approach provides the foundation to quantitatively model more complicated scenarios of coupling between grain size, texture and loading direction in the plasticity of Mg alloys.

5.2 Introduction

Simulations based on crystal plasticity constitutive models have proven to be a powerful tool to derive insights into polycrystalline microstructures from single-crystal constitutive models integrated with the governing equations on continuum mechanics. While classical crystal plasticity constitutive models [1-5] have been extremely useful, by construction they are unable to capture the difference in mechanical behavior that arises from changes in the internal microstructural length scale, like the grain size. To address this issue one alternative has been the strain-gradient plasticity approach which has proven [6-9] particularly useful in capturing the intrinsic size effects arising in a number of plasticity-related phenomena. However, these models are relatively expensive to evaluate and also pose a challenge for parameter calibration since they involve a large number of internal variables. Another simpler alternative has been to include a grain size-dependent contribution to the CRSS of individual slip systems by simply extending the Hall-Petch relationship to individual slip systems empirically. Based on such a modification, there have been very few computational studies addressing the coupling between grain size and texture in Mg alloys. Jain *et al*. [10, 11] conducted studies using a grain size-dependent viscoplastic self-consistent crystal plasticity (VPSC) model on a rolled Mg alloy, which indicated the role of grain size-effect associated with prismatic slip in the tensile behavior. Such VPSC models have also been used to explore the role of grain size on the twin growth [12], the density of twins [13], and also the correlation between the crystallographic orientation of the grain and corresponding twin variant selected [14]. Ravaji *et al*. [15] investigated the interacting effects between the grain size, loading direction and texture on the response of an Mg alloy. They investigated the role of grain size-texture coupling in reducing the net plastic anisotropy, the tension-compression asymmetry and the tempering of extension twinning with grain refinement across different textures and loading directions. Common in all these important studies is that a single average grain size is used to modify the CRSS for all the grains in the simulated microstructure. Moreover, this modification to the CRSS at the slip system level, which resembles the linear dependence on the inverse square-root of the average grain size, uses a constant Hall-Petch type parameter for a particular slip system for all the grains in the microstructure. In other words, the microstructural features are not captured directly in the parts of the constitutive model accounting for the grain size in some manner.

Such an inclusion of the microstructural features builds on our recent work [16-18] which uses the micro-Hall-Petch equation as the basis for including the grain size effect in our constitutive model:

$$\tau^{\alpha} = \tau_0^{\alpha} + \tau_g^{\alpha} = \tau_0^{\alpha} + \frac{k_{\mu}^{\alpha}}{\sqrt{d^{\alpha}}} \tag{5.2}$$

where τ^{α} denotes the initial slip resistance (identical to CRSS) associated with slip system α, decomposed into a grain size-independent contribution (τ_0^{α}) and grain size-dependent contribution (τ_g^{α}). Additionally, this grain size-dependent contribution has a form similar to the classical Hall-Petch equation but extended to the slip system level where k_{μ}^{α} denotes the micro-Hall-Petch parameter and d^{α} is a measure of the slip system-level grain size. Andani *et al*. [17, 18] integrated experimental measurements of pile-up stress ahead of slip bands blocked by a grain boundary, with a dislocation pile-up model and crystal plasticity simulations, to obtain the empirical power-law relationship between k_{μ}^{α} and certain geometrical descriptors of the grain boundaries for basal and prismatic slip systems:

$$k_{\mu}^{\alpha} = K_{\mu}^{\alpha}(1 - \cos(\theta)\cos(\kappa))^{c^{\alpha}} \tag{5.3}$$

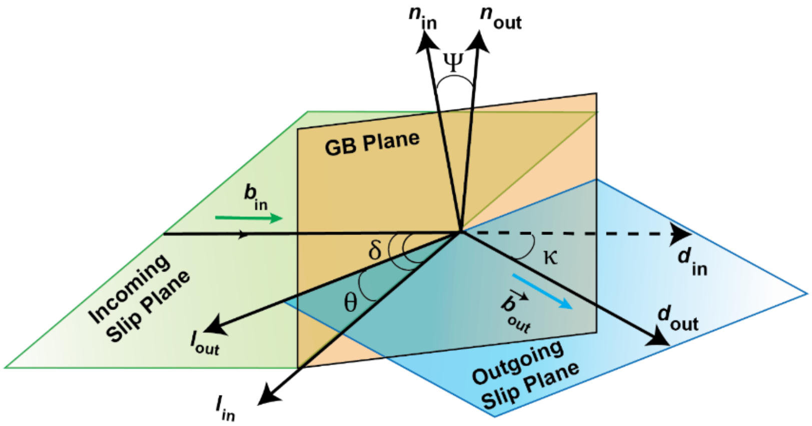

Figure 5.1 A schematic representative for slip transmission through a GB. $\vec{b}_{in}$: Burgers vector of the incoming slip system, $\vec{b}_{out}$: Burgers vector of the outgoing slip system, $\vec{n}_{in}$: Slip plane normal of the incoming slip system, $\vec{n}_{out}$: Slip plane normal of the outgoing slip system, $\vec{l}_{in}$: Intersection line of the incoming slip plane and GB, $\vec{l}_{out}$: Intersection line of the outgoing slip plane and GB, $\vec{d}_{in}$: Slip direction of the incoming slip system, $\vec{d}_{out}$: Slip direction of the outgoing slip system, θ: Angle between the two slip plane traces on the grain boundary plane, κ: Angle between slip directions, ψ: Angle between slip plane normal, δ: Angle between the incoming slip direction and the incoming slip plane trace on the grain boundary plane.

where K_{μ}^{α} denotes the micro-Hall-Petch multiplier and c^{α} the micro Hall-Petch exponent, respectively for slip system α. 'ψ' and 'κ' denote angular quantities obtained from knowledge of the slip systems in neighboring grains and the geometric properties of the grain boundary (Figure 5.1). As a result of these studies, K_{μ}^{α} and c^{α} were estimated for basal [17] and prismatic [18] slip systems, providing quantitative insights into the role of grain boundaries in informing the grain size-dependent contribution to the slip resistance. Additionally, in the interest of implementing such a relationship in crystal plasticity constitutive models, a similar power-law relationship was drawn where instead of the angle 'θ', the angle 'ψ', was used:

$$k_{\mu}^{\alpha} \;=\; K_{\mu}^{\alpha}(1-\cos(\theta)\cos(\kappa))^{c^{\alpha}} \tag{5.4}$$

This aspect is particularly important in the simulation context since grain boundary inclination in synthetic microstructures is sensitive to the mesh used in their discretization. The relationship in

Eqn. 4 provides a way to sidestep the grain boundary information, and as a first step only include the relative crystallographic orientation between grains as the key parameter in parametrizing the micro-Hall-Petch parameter.

In this chapter, we present our attempts to implement the micro-Hall-Petch equation into a crystal plasticity simulation framework and perform parametric studies. We briefly outline the rate-dependent crystal plasticity constitutive model implemented into the open-source PRISMS-Plasticity crystal plasticity finite element (CPFE) framework [19-21], that is used for all our simulations. Then, we outline the procedure to compute the micro-Hall-Petch parameter, k_{μ}^{α}, and the slip system-level grain size, d^{α}, which forms part of the preprocessing step to then modify the slip resistances based on the micro-Hall-Petch equation. Following this, comparisons of stress-strain curves are presented between simulations and experiments to assess the slip resistance and micro Hall-Petch multipliers reported in previous chapter [17, 18], before calibrating for a new set of parameters.

5.3 Computational and Experimental Methods

The author conducted the computational work in collaboration with Prof. Veera Sundararaghavan and his student Aaditya Lakshmanan.

5.3.1 Micro Hall-Petch Constitutive Model

As mentioned in the previous section, the initial slip resistance consists of a size-independent and a size-dependent contribution. The computation of k_{μ}^{α} includes information concerning the grain neighbors while d^{α} encodes the information of both the grain size and grain morphology. We now outline the procedure followed in computing these key quantities (illustrated in Figure 2).

Assuming we are given a microstructure discretized as a structured grid of voxels, along with information about the grains, i.e., a set of grain identifiers(integers), and the orientation associated with those identifiers. With this input, d^{α} is computed for each voxel of the microstructure as follows:

1. Consider any particular voxel defined by it's centroidal coordinates $\mathbf{p}_c = (x_c, y_c, z_c)$ along with the corresponding grain, G, it belongs to. With this voxel fixed, consider slip system α for which we wish to compute k^{α} and d^{α}, with $\mathbf{m}^{\alpha}$ denoting the slip direction.
2. For grain G, identify its boundary ∂G, which is essentially a collection of rectangular patches.
3. Find the point $\mathbf{p}_1$ on ∂G closest[1] to point $\mathbf{p}_c$ along direction $\mathbf{m}^{\alpha}$. Denote this closest distance by d_1^{α}.
4. Find the point $\mathbf{p}_2$ on ∂G closest to point $\mathbf{p}_c$ along direction $-\mathbf{m}^{\alpha}$. Denote this closest distance by d_2^{α}.
5. The slip system-level grain size d^{α} is defined as $d^{\alpha} = d_1^{\alpha} + d_2^{\alpha}$.

k_{μ}^{α} is computed as follows:

1. Having computed points $\mathbf{p}_1$and $\mathbf{p}_2$ the neighboring grains sharing these points with grain G are first found. Denote them by G_1 and G_2, respectively.
2. Define $\psi_1^{\alpha\beta}$ as the angle satisfying the relation $cos\left(\psi_1^{\alpha\beta}\right) = \mathbf{n}^{\alpha} \cdot \mathbf{n}_1^{\beta}$ where $\mathbf{n}^{\alpha}$is the slip plane corresponding to slip system α and $\mathbf{n}_1^{\beta}$ is the slip plane corresponding to slip system β in G_1. Define $\kappa_1^{\alpha\beta}$ as the angle satisfying the relation $cos\left(\kappa_1^{\alpha\beta}\right) = \mathbf{m}^{\alpha} \cdot \mathbf{m}_1^{\beta}$ where

---

[1] Since the grain *G* need not be a convex set.

$\mathbf{m}^{\alpha}$ is the slip plane corresponding to slip system α and $\mathbf{m}_1^{\beta}$ is the slip plane corresponding to slip system β in G_1.

3. Compute the compatibility factor defined as $cos\left(\psi_1^{\alpha\beta}\right) cos\left(\kappa_1^{\alpha\beta}\right)$ over a chosen set of slip systems in $G_1$and identify the maximum over this set. Denote this maximum by μ_1.
4. Define $\psi_2^{\alpha\beta}$ as the angle satisfying the relation $cos\left(\psi_2^{\alpha\beta}\right) = \mathbf{n}^{\alpha} \cdot \mathbf{n}_2^{\beta}$ where $\mathbf{n}^{\alpha}$is the slip plane corresponding to slip system α and $\mathbf{n}_2^{\beta}$ is the slip plane corresponding to slip system β in G_2. Define $\kappa_2^{\alpha\beta}$ as the angle satisfying the relation $cos\left(\kappa_2^{\alpha\beta}\right) = \mathbf{m}^{\alpha} \cdot \mathbf{m}_2^{\beta}$ where $\mathbf{m}^{\alpha}$is the slip plane corresponding to slip system α and $\mathbf{m}_2^{\beta}$ is the slip plane corresponding to slip system β in G_2.
5. Compute the compatibility factor defined as $cos\left(\psi_2^{\alpha\beta}\right) cos\left(\kappa_2^{\alpha\beta}\right)$ over a chosen set of slip systems in G_2 and identify the maximum over this set. Denote this maximum by μ_2.
6. Compute k^{α} using the micro Hall-Petch equation as $k_{\mu}^{\alpha} = K_{\mu}^{\alpha}(1 - max(\mu_1, \mu_2))^{c^{\alpha}}$, where K_{μ}^{α} is the micro Hall-Petch multiplier, c^{α} is the micro Hall-Petch exponent, fixed for the material under consideration and $max(\mu_1, \mu_2)$ denotes the maximum computability factor which is the maximum among μ_1 and μ_2.

The computation of d^{α} and k_{μ}^{α} is implemented in a MATLAB script which is used as a pre-processor to generate this data in a format readable by PRISMS-Plasticity CPFE.

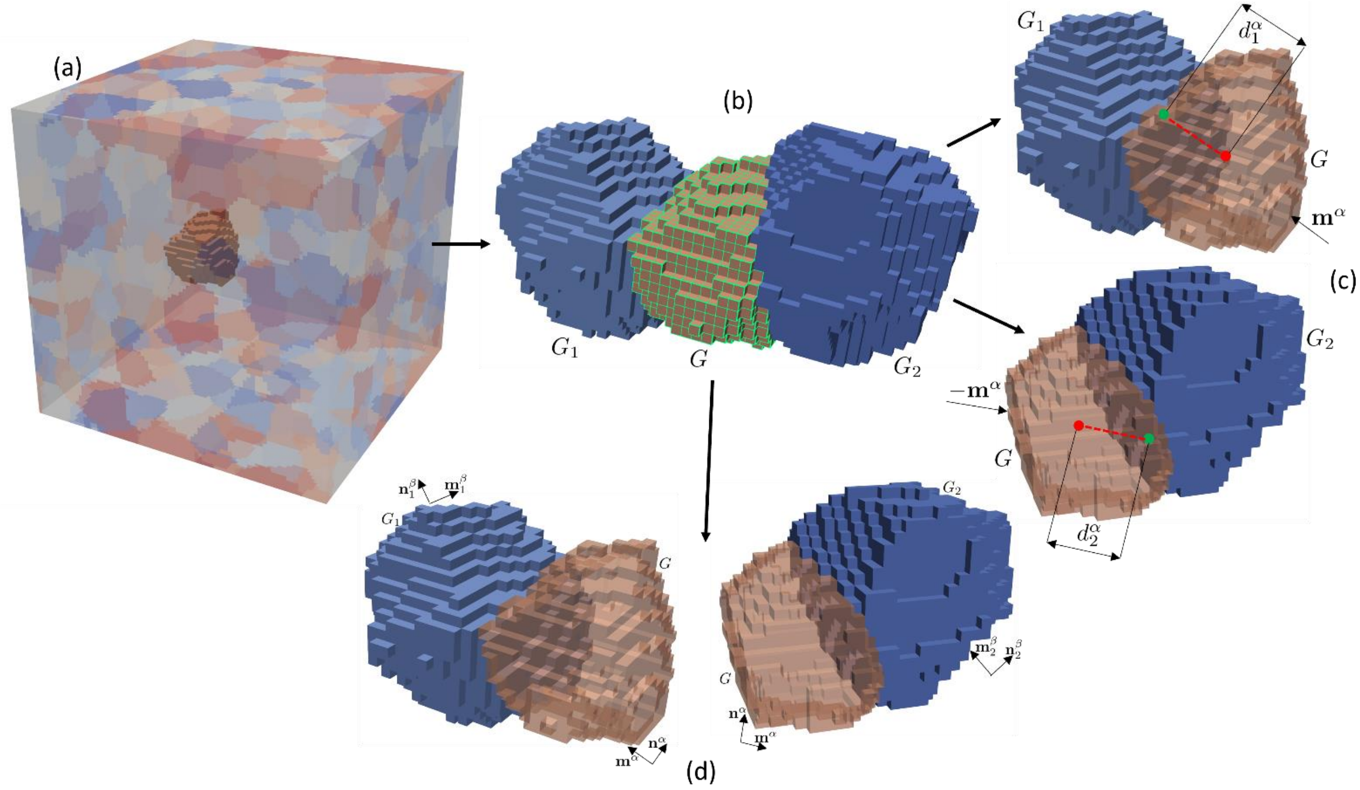

Figure 5.2 Illustration depicting the workflow described in Section 5.2.2 to compute d^α and k_μ^α. (a) Voxelated microstructure from DREAM.3D. (b) For any microstructural point in grain G and line passing through it with slip direction $\mathbf{m}^\alpha$, find the neighboring grains G_1 and G_2 based on the points of intersection of the line with the boundary. (c) The slip system level grain size d^α is computed for every point in the microstructure by finding the length of the line segment passing through that point connecting the two points on the grain boundary with direction $\mathbf{m}^\alpha$. (d) To compute k_μ^α the primary quantity is the maximum compatibility factor which is computed using the knowledge of slip systems corresponding to the neighboring grains G_1 and G_2. The neighboring grains are identified by the neighbors of G that share each of the two points on the grain boundary that were found for computing d^α.

5.4 Materials and experimental procedures

Extruded Mg-4Al (wt.%) bars provided by CanmetMaterials are used in this work. The texture of the as-received material and the compressed samples (5% compression along the extrusion direction following heat treatment at 300°C for 3 hours) with the average grain size of

55 µm and 68 µm, respectively are shown in Figure 5.3a and Figure 5.3b. Additional heat treatment was conducted on the as-received samples to provide specimens with average grain sizes of approximately 187 µm (515°C for 15 minutes) and 333 µm (550°C for 150 minutes) with textures very similar to the starting texture. Similarly, additional heat treatment was conducted on the compressed samples to provide specimens with average grain sizes of approximately 227 µm (515°C for 15 minutes) and 343 µm (550°C for 150 minutes) with textures very similar to the starting texture.

Crystallographic orientation information was obtained using electron backscatter diffraction (EBSD). Scans were conducted using a Tescan Mira 3 scanning electron microscope equipped with an EDAX Hikari XP EBSD detector. Each scan was captured at a voltage of 30kV and a beam intensity of 20 nA with an average step size of 1 µm. The samples are mechanically ground using SiC papers up to a grit of 1200. Polishing is completed using three steps 6 µm, 3 µm, and 1 µm diamond suspensions, followed by a final polish using Buehler Masterpolish on a Buehler Chemomet polishing cloth. Finally, samples are chemically etched in acetic-nitric solution (60 mL ethanol, 20 mL water, 15mL acetic acid, and 5 mL nitric acid) for 3-5 seconds. Tensile tests are conduced on samples with the gauge dimensions of 10 mm × 2 mm × 2 mm using INSTRON load frame equipped with a 100kN load cell at a constant displacement rate of 1µm/second. The macroscopic strain was measured using an extensometer attached to the sample.

(a)

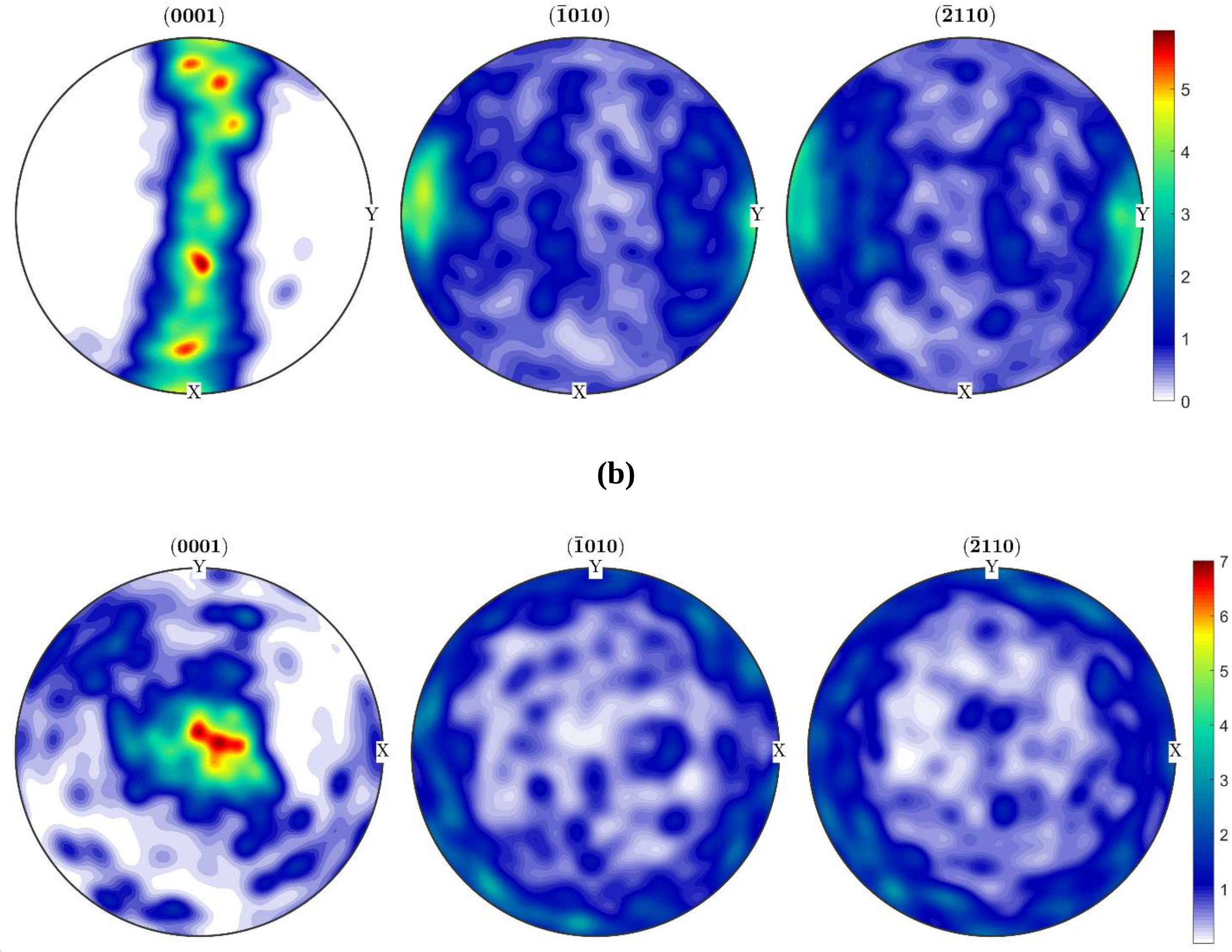

(b)

Figure 5.3 (a) Texture 1 - As-extruded texture for which the specimens with the three average grain sizes are deformed along the extrusion direction (y-axis), (b) Texture 2 – Close to basal texture for which the specimens with the three average grain sizes are deformed along normal direction (z-axis).

5.5 Preprocessing

5.5.1 Synthetic Microstructure Generation

Here we outline the procedure to generate synthetic microstructures for our simulations using DREAM.3D [22], an open-source tool to generate artificial microstructures given certain input statistics. The primary inputs required by DREAM.3D to generate microstructures are the texture and grain size distribution. For each of the nine cases, the input from microscopy is an

EBSD orientation map consisting of the orientations of the pixels in the pixelated image of a 2D section of the microstructure (Figure 5.4a). MTEX [23], a free MATLAB toolbox for texture analysis, is used to read in the EBSD map, compute the ODF and pole figures (Figure 5.4d), and write out this EBSD data in a format readable by DREAM.3D. For the grain size distribution data, the equivalent grain sizes for all the grains in the 2D section is straightforward to obtain using MTEX. However, this furnishes a 2D measure of grain size, which is always an under-estimation of the real grain size because these EBSD maps are 2D sections. The way we addressed this issue is to use the 2D equivalent grain size statistics(Figure 5.4b) obtained from MTEX along with the Scheil-Schwartz-Saltykov method [24-26] to obtain the 3D grain size statistics, assuming equiaxed grains. Saltykov [24] proposed a general algorithm to compute the probability distribution of spheres of different sizes, given information about the apparent sizes (from 2D sections). The 3D grain size statistics are then fit with a lognormal distribution (Figure 5.4c), whose characteristic parameters (mean and variance) are fed into DREAM.3D to generate synthetic microstructures (Figure 5.4e).

Once these microstructures are generated, the relevant information is passed into the MATLAB script to compute d^{α} and k_{μ}^{α} for all voxels constituting the microstructure, using the procedure described in Section 2.2.

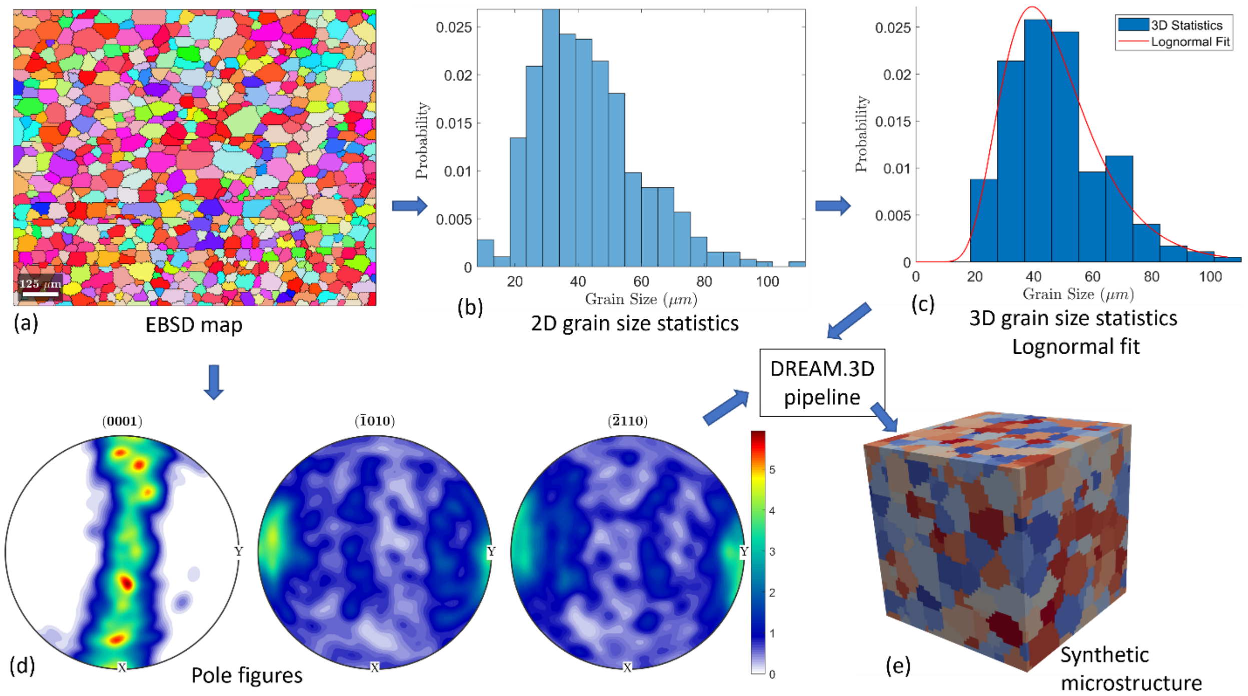

Figure 5.4 Illustration depicting the workflow described in Section 2.4.1 to obtain necessary inputs for synthetic microstructure generation in DREAM.3D. (a) Microstructure section from experiment, (b) 2D grain size statistics extracted from microstructure section, (c) Use Saltykov's method to obtain 3D grain size statistics and fit it with lognormal distribution, (d) Pole figures from experimental texture data, (e) Use lognormal fit and pole figures as input to DREAM.3D to generate synthetic microstructure.

5.5.2 Constitutive Parameters

All crystal plasticity simulations were performed assuming possible activity of 12 slip systems, listed in Table 5.1 - 3 basal, 3 prismatic, 6 pyramidal <c+a> - and 6 pyramidal <c+a> twin systems. Table 5.2 lists the elastic stiffness constants used in calibration [27-29]. In the hardening law, the latent hardening coefficient was set to $q = 1.0$, while the flow rule parameters were set as $\dot{\gamma}_0 = 0.001$ and $m = 34$. The basal and prismatic slip resistances and micro-Hall-Petch multipliers are the four parameters that fit based on comparison with experimental data, which we present later.

Table 5.3 presents the original set of crystal plasticity constitutive parameters to examine the predictions of the stress-strain curves for the different grain size and texture cases. Table 5.4 shows the same table with some values replaced by symbols which represent free parameters which we calibrate to obtain better match with the stress-strain curves.

Table 5.1 List of slip direction and slip plane orientations for different slip/twin systems for Mg alloys.

Slip/Twin System	**ID**	**Slip Direction**	**Slip Plane**
Basal	1	$[11\bar{2}0]$	(0001)
	2	$[\bar{2}110]$	(0001)
	3	$[1\bar{2}10]$	(0001)
Prismatic<a>	4	$[1\bar{2}10]$	$(10\bar{1}0)$
	5	$[2\bar{1}\bar{1}0]$	$(01\bar{1}0)$
	6	$[11\bar{2}0]$	$(\bar{1}100)$
Pyramidal<c+a>	7	$[\bar{1}\bar{1}23]$	$(11\bar{2}2)$
	8	$[1\bar{2}13]$	$(\bar{1}2\bar{1}2)$
	9	$[2\bar{1}\bar{1}3]$	$(\bar{2}112)$
	10	$[11\bar{2}3]$	$(\bar{1}\bar{1}22)$
	11	$[\bar{1}2\bar{1}3]$	$(1\bar{2}12)$
	12	$[\bar{2}113]$	$(2\bar{1}\bar{1}2)$
Twin<c + a>	13	$[\bar{1}011]$	$(10\bar{1}2)$
	14	$[10\bar{1}1]$	$(\bar{1}012)$
	15	$[\bar{1}101]$	$(1\bar{1}02)$
	16	$[1\bar{1}01]$	$(\bar{1}102)$
	17	$[0\bar{1}11]$	$(01\bar{1}2)$
	18	$[01\bar{1}1]$	$(0\bar{1}12)$

Table 5.2 Elastic stiffness constants (in GPa) for Mg-4Al alloy [27-29]

C_{11}	C_{33}	C_{12}	C_{13}	C_{44}
59.4	61.6	25.61	21.44	16.4

Table 5.3 Original crystal plasticity constitutive model parameters [16-18]

Mode	s_0^α(MPa)	h_0^α(MPa)	s_s^α(MPa)	a^α	$K_\mu^\alpha\ (MPa\, m^{0.5})$	c^α
Basal <a>	4.34	0.0	-	1.0	0.159	0.6
Prismatic <a>	42.54	1000.0	150.0	1.0	0.699	1.07
Pyramidal <c + a>	140.0	0.0	-	1.0	-	-
Twin <c + a>	18.0	0.0	-	1.0	-	-

5.6 Results and Discussion

5.6.1 Original parameters vs Calibration parameters

Synthetic microstructures were generated for as-extruded and basal textures for three different average grain sizes. For each texture and grain size case, DREAM.3D was fed the input texture and lognormal distribution parameters to generate a microstructure represented as a 50 x 50 x 50 voxelated grid containing approximately 500 grains. All microstructures generated using texture 1 were deformed along the extrusion direction(y-axis) with periodic boundary constraints to a strain of 1.5%. All the microstructures generated using texture 2 were deformed along the normal direction(z-axis) with periodic boundary constraints to a strain of 0.35%.

As mentioned earlier, there are parameters that we calibrate – initial basal slip resistance (s_0^b), initial prismatic slip resistance (s_0^p), the basal micro Hall-Petch coefficient (K_μ^b) and the prismatic micro Hall-Petch multiplier (K_μ^p). Before calibrating these four constitutive parameters, we test the stress-strain curve predictions given by the original slip resistance parameters which formed part of the simple continuum dislocation pile-up models in previous work and the corresponding micro Hall-Petch multipliers obtained from curve fitting in those works (Table 5.3). Figures 5a and 5b depict the stress-strain curve comparison between CPFE simulations and experiments for texture 1 and texture 2, respectively. It is interesting to note that even though the stress-strain curves do not all match with a single parameter set, they produce quite reasonable stress-strain curves. It should be noted that the slip resistance values used here were fed to pile-up models, and the micro Hall-Petch coefficients were then obtained from localized measurements ahead of slip bands blocked by grain boundaries.

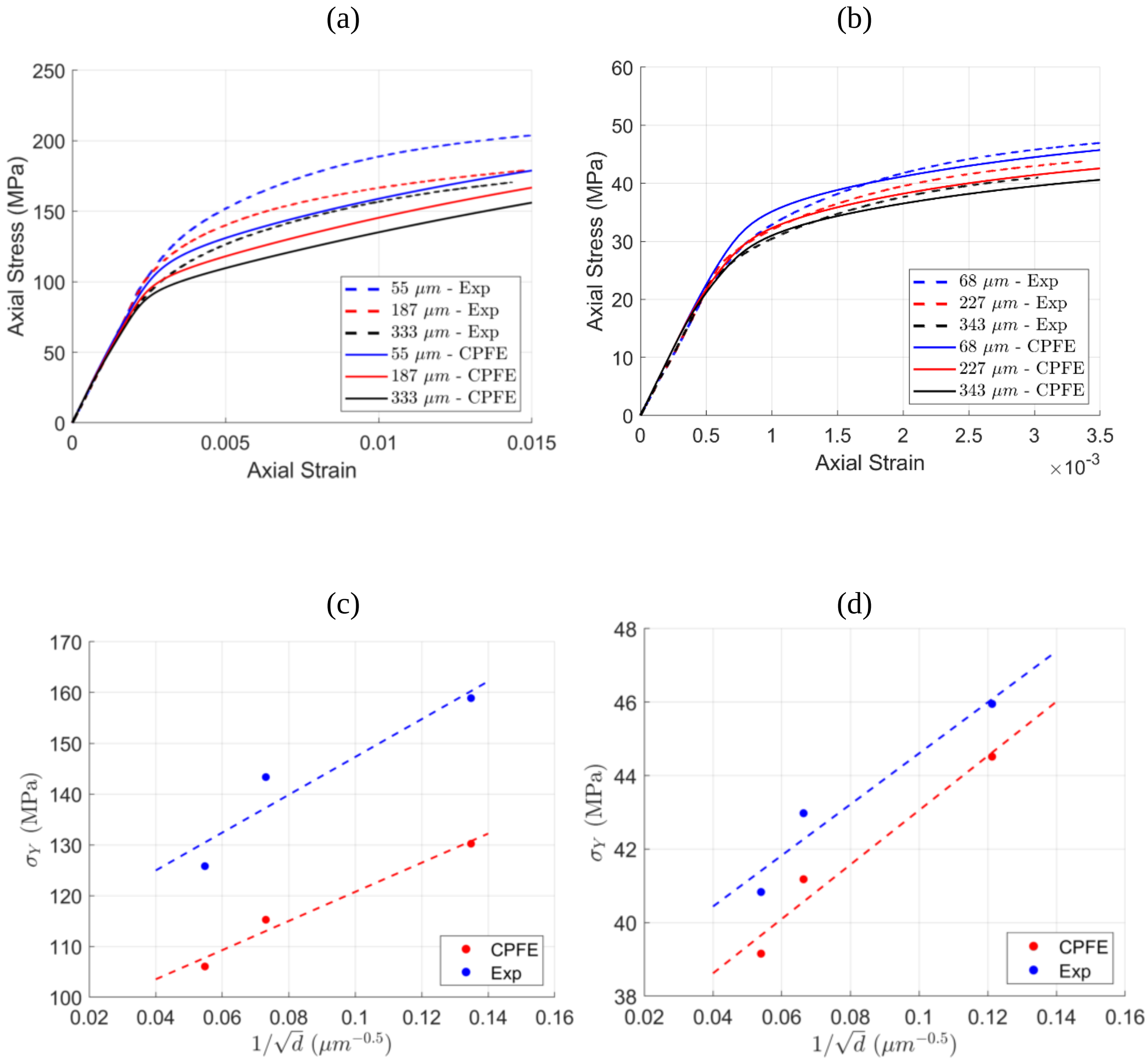

Figure 5.5 Stress-strain curve comparison between CPFE simulations and experiments for (a) texture 1 and, (b) texture 2. Yield stress vs inverse square-root grain size comparison between CPFE simulations and experiments for (c) texture 1 and, (d) texture 2.

Figures 5.5c and 5.5d depict the yield stress (σ_Y) plotted against the corresponding inverse square-root of grain size $\left(\sqrt{d}^{-1}\right)$, computed from the average 2D grain size measured in the experimental microstructure sections. In all our plots of yield stress against the grain size we always set d to be the 2D grain size of the microstructural section. Table 5.4 shows the comparison between the Hall-Petch coefficients, i.e., the Hall-Petch intercept (σ_0) and Hall-Petch slope (K_{HP}) for the two textures between CPFE simulations and experiments.

Table 5.4 Comparison of Hall-Petch coefficients between CPFE simulations and experiments for texture 1 and texture 2

Hall-Petch coefficients	Texture 1: Exp.	Texture 1: CPFE	Texture 2: Exp.	Texture 2: CPFE
σ_0 (MPa)	110.06	92.05	37.66	35.66
K_{HP} $(MPa\ m^{0.5})$	0.37242	0.28697	0.06944	0.07393

We then calibrated the stress-strain curves to obtain a better match with experiments by modifying the four crystal plasticity constitutive parameters. Figures 6a and 6b depicts the stress-strain curve comparison between CPFE simulations and experiments for texture 1 and texture 2, respectively, for the calibrated set of parameters - $s_0^b = 9.3\ MPa$, $s_0^p = 50.5\ MPa$, $K_\mu^b = 0.060\ MPa\ m^{0.5}$, $K_\mu^p = 1000\ MPa\ \mu m^{0.5}$, $s_0^t = 14\ MPa$ and $K^t\ =\ 0.030\ MPa\ m^{0.5}$. Figures 6c and 6d depict the yield stress (σ_Y) plotted against the corresponding inverse square-root of grain size $\left(\sqrt{d}^{-1}\right)$ based on the simulations with the calibrated parameters.

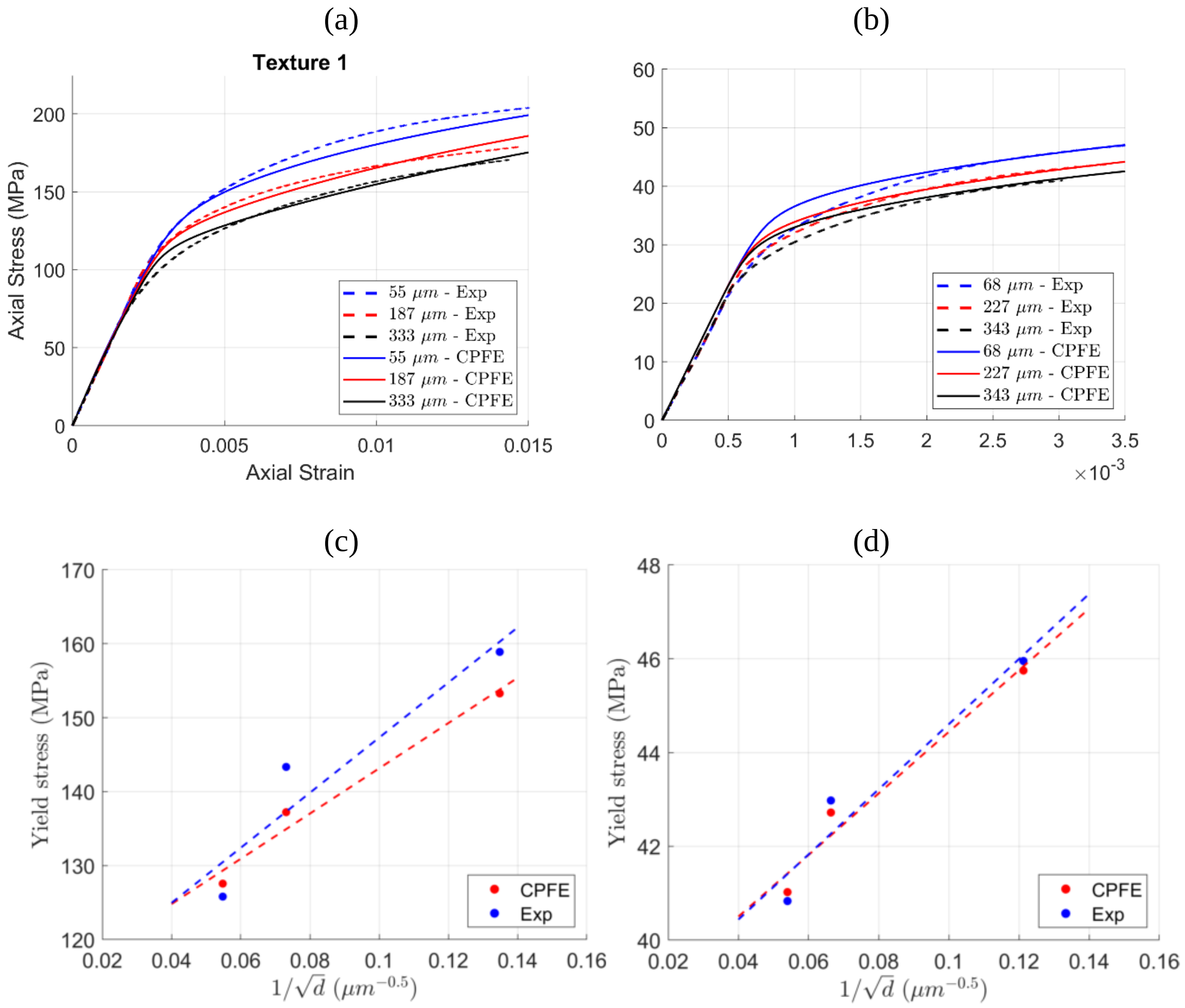

Figure 5.6 Stress-strain curve comparison between CPFE simulations with calibrated parameters and experiments for (a) texture 1 and, (b) texture 2. Yield stress vs inverse square-root grain size comparison between CPFE simulations with calibrated parameters and experiments for (c) texture 1 and, (d) texture 2.

Table 5.5 shows the comparison between the Hall-Petch coefficients, i.e., the Hall-Petch intercept (σ_0) and Hall-Petch slope (K_{HP}) for the two textures between CPFE simulations with calibrated parameters and experiments.

Table 5.5 Comparison of Hall-Petch coefficients between CPFE simulations with calibrated parameters and experiments for texture 1 and texture 2

Hall-Petch coefficients	Texture 1: Exp.	Texture 1: CPFE	Texture 2: Exp.	Texture 2: CPFE
σ_0 (MPa)	110.06	112.56	37.66	37.86
K_{HP} $(MPa\ \mu m^{0.5})$	0.37242	0.30584	0.06944	0.06565

5.6.2 *Crystal Plasticity Finite Element Method*

A rate-dependent crystal plasticity constitutive model is adopted within the framework of finite deformation continuum mechanics. The primary kinematic quantity is the deformation gradient, **F**, which maps tangent vectors in the reference configuration to corresponding vectors in the deformed configuration. Assuming **F** abides by a multiplicative decomposition [30, 31] into elastic($\mathbf{F}^{\mathrm{e}}$) and plastic($\mathbf{F}^{\mathrm{p}}$) components as follows:

$$\mathbf{F} = \mathbf{F}^{\mathrm{e}}\mathbf{F}^{\mathrm{p}} \tag{5.5}$$

$\mathbf{F}^{\mathrm{p}}$ encodes the distortion of the body as a consequence of crystallographic slip via dislocation slip on specific slip systems. It maps the reference configuration to an intermediate configuration where the underlying lattice remains unchanged. $\mathbf{F}^{\mathrm{e}}$ captures the elastic stretch and lattice rotation and maps the intermediate configuration to the deformed configuration. Since plasticity is inherently deformation path-dependent we invoke certain deformation rates. Using Eqn. (5.5), the velocity gradient, $\mathbf{L} = \dot{\mathbf{F}}\mathbf{F}^{-1}$, can then be decomposed into elastic and plastic components:

$$\mathbf{L} = \underbrace{\dot{\mathbf{F}}^{\mathrm{e}}\mathbf{F}^{\mathrm{e}-1}}_{\text{Elastic part}} + \underbrace{\mathbf{F}^{\mathrm{e}}\dot{\mathbf{F}}^{\mathrm{p}}\mathbf{F}^{\mathrm{p}-1}\mathbf{F}^{\mathrm{e}-1}}_{\text{Plastic part}} \tag{5.6}$$

Contributions to the velocity gradient from elastic and plastic parts are both defined in the deformed configuration. We can alternatively work with the plastic part of the velocity gradient defined on the intermediate configuration, $\mathbf{L}^{\mathrm{p}}$, as:

$$\mathbf{L}^{\mathrm{p}} = \dot{\mathbf{F}}^{\mathrm{p}}\mathbf{F}^{\mathrm{p}-1} \tag{5.7}$$

Noting that the kinematics of crystallographic slip effectively involves shearing of the lattice on specific crystallographic slip planes along with specific crystallographic slip directions, we have

$$\mathbf{L}^{\mathrm{p}} = \dot{\mathbf{F}}^{\mathrm{p}}\mathbf{F}^{\mathrm{p}-1} = \sum_{\alpha=1}^{n_s} \dot{\gamma}^{\alpha}\mathbf{m}^{\alpha}\otimes\mathbf{n}^{\alpha} = \sum_{\alpha=1}^{n_s} \dot{\gamma}^{\alpha}\mathbf{S}^{\alpha} \tag{5.8}$$

where $\dot{\gamma}^{\alpha}$ is the shearing rate on slip system α, n_s is the number of slip systems, $\mathbf{m}^{\alpha}$ and $\mathbf{n}^{\alpha}$ are slip direction and slip plane normal unit vectors, respectively. $\mathbf{S}^{\alpha}$, referred to as the Schmid tensor for the slip system α, is a shorthand for the dyadic product of $\mathbf{m}^{\alpha}$ and $\mathbf{n}^{\alpha}$. We note that $\mathbf{m}^{\alpha}$ and $\mathbf{n}^{\alpha}$ are crystallographic vectors in the intermediate configuration.

We adopt a rate-dependent crystal plasticity framework, where the shearing rate $\dot{\gamma}^{\alpha}$ is a function of the resolved shear stress τ^{α} through a phenomenological power law [32] as follows:

$$\dot{\gamma}^{\alpha} = \dot{\gamma}_0 \left|\frac{\tau^{\alpha}}{s^{\alpha}}\right|^{m} \mathrm{sign}(\tau^{\alpha}) \tag{5.9}$$

where $\dot{\gamma}_0$ is the reference shearing rate, m is the strain rate sensitivity exponent, τ^{α} is the resolved shear stress on slip system α, s^{α} is the slip resistance on slip system α and 'sign' refers to the signum function. The resolved shear stress is expressed in terms of the second Piola-Kirchoff stress in the intermediate configuration [33, 34], $\mathbf{T}$, via the following relation:

$$\tau^{\alpha} = (\mathbf{F}^{\mathrm{e}\mathrm{T}}\mathbf{F}^{\mathrm{e}}\mathbf{T}) : \mathbf{S}^{\alpha} \tag{5.10}$$

where ':' denotes the inner product of second order tensors defined as $\mathbf{A} : \mathbf{B} = A_{ij}B_{ij}$. Eqn. (5.10) is derivable by equating the plastic part of the internal mechanical power to the power expended in crystallographic shearing of slip system α with resolved shear stress τ^{α} and shearing rate $\dot{\gamma}^{\alpha}$.

The second Piola-Kirchoff stress in the intermediate configuration is linked to the elastic Green-Lagrange strain as follows

$$\mathbf{T} = \mathcal{L} \cdot \mathbf{E}^{\mathrm{e}} = \frac{1}{2}\mathcal{L} \cdot (\mathbf{F}^{\mathrm{eT}}\mathbf{F}^{\mathrm{e}} - \mathbf{I}) \tag{5.11}$$

where $\mathbf{E}^{\mathrm{e}}$ is the elastic Green-Lagrange strain tensor, $\mathcal{L}$ is the elastic stiffness (a fourth-order tensor) and **I** is the second-order identity tensor. '·' denotes the product between a fourth-order tensor and second-order tensor to furnish a resultant second-order tensor, defined as $(\mathcal{L} \cdot \mathbf{A})_{ij} = \mathcal{L}_{ijkl}A_{kl}$. We additionally note that the Cauchy stress, $\boldsymbol{\sigma}$, and the first Piola-Kirchoff stress in the reference configuration, **P** , can be computed from **T** as follows:

$$\mathbf{T} = \mathbf{F}^{\mathrm{e}-1}\mathbf{P}\,\mathbf{F}^{T}\mathbf{F}^{\mathrm{e}-T} = \det(\mathbf{F}^{\mathrm{e}})\mathbf{F}^{\mathrm{e}-1}\boldsymbol{\sigma}\,\mathbf{F}^{\mathrm{e}-T} \tag{5.12}$$

Finally, the evolution of slip resistance for slip system α, which governs isotropic hardening, is defined as follows [34]:

$$\dot{s}^{\alpha} = \textstyle\sum_{\beta} h^{\alpha\beta}\dot{\gamma}^{\beta} \tag{5.13}$$

$$s^{\alpha}(0) = s_0^{\alpha} + s_g^{\alpha} = s_0^{\alpha} + \frac{k_{\mu}^{\alpha}}{\sqrt{d^{\alpha}}} \tag{5.14}$$

where $h^{\alpha\beta}$, denotes the hardening rate on slip system α due to the slip on system β. s_0^{α} and s_g^{α} denote the size-independent and size-dependent contributions, respectively, to the initial slip resistance. s_g^{α} is assumed to hold a functional-form identical to the classical Hall-Petch equation, but now extended to the level of an individual slip system, with k_{μ}^{α} denoting the micro Hall-Petch multiplier and d^{α} denoting a measure of the slip system-level grain size. The hardening moduli $h^{\alpha\beta}$ are prescribed as a power-law relationship involving the combined effect of work hardening and recovery, with both self and latent hardening contributions as follows:

$$h^{\alpha\beta} = \begin{cases} h_0^{\beta}\left[1-\frac{s^{\beta}}{s_s^{\beta}}\right]^{a^{\beta}} & ;\ \text{coplanar systems} \\ h_0^{\beta} q\left[1-\frac{s^{\beta}}{s_s^{\beta}}\right]^{a^{\beta}} & ;\ \text{otherwise} \end{cases} \tag{15}$$

where h_0^{β} denotes the hardening parameter for slip system β, q is the latent hardening ratio, s_s^{β} is the saturation slip resistance for slip system β, and a^{β} is a material constant for slip system β governing the sensitivity of the hardening moduli to the slip resistance. The constitutive model is implemented in the PRISMS-Plasticity CPFE code [20, 21], an open-source, scalable software framework to simulate elasto-plastic boundary value problems built on top of the deal.II [35] open source finite element(FE) library.

5.7 Conclusions

- A procedure to compute the micro-Hall-Petch parameter, k_{μ}^{α} ($k_{\mu}^{\alpha} = K_{\mu}^{\alpha}(1 - \cos(\theta)\cos(\kappa))^{c^{\alpha}}$), and the slip system-level grain size, d^{α}, to calculate slip resistances based on the micro-Hall-Petch equation ($s^{\alpha}(0) = s_0^{\alpha} + s_g^{\alpha} = s_0^{\alpha} + \frac{k_{\mu}^{\alpha}}{\sqrt{d^{\alpha}}}$) was developed.
- The method to incorporate the modified slip system resistance into a CPFE framework to simulate the plastic behavior of microstructures, including the grain size and texture effects, was developed.
- We presented a comparison of the stress-strain curves between CPFE and experiments using parameters proposed in previous work before calibration using four parameters – the basal and prismatic slip resistances and the basal and prismatic micro Hall-Petch multipliers.
- The comparison between the Hall-Petch coefficients, i.e., the Hall-Petch intercept (σ_0) and Hall-Petch slope (K_{HP}) for the two textures between CPFE simulations with calibrated parameters and experiments were presented. The results show the CPFE model with modified

slip resistance based on the micro-Hall-Petch equation can capture the role of grain size and the texture in predicting the mechanical behavior of materials. This work provides the foundation to quantitatively model more complicated scenarios of coupling between grain size, texture, and loading direction in the plasticity of Mg alloys.

5.8 References

1. Asaro, R.J. and J.R. Rice, *Strain localization in ductile single crystals.* Journal of the Mechanics and Physics of Solids, 1977. **25**.
2. Hill, R., *Generalized constitutive relations for incremental deformation of metal crystals by multislip.* Journal of the Mechanics and Physics of Solids, 1966. **14**.
3. Hill, R. and K.S. Havner, *Perspectives in the mechanics of elastoplastic crystals.* Journal of the Mechanics and Physics of Solids, 1982. **30**.
4. Hill, R. and J.R. Rice, *Constitutive analysis of elastic-plastic crystals at arbitrary strain.* Journal of the Mechanics and Physics of Solids, 1972. **20**.
5. Peirce, D., R.J. Asaro, and A. Needleman, *An analysis of nonuniform and localized deformation in ductile single crystals.* Acta Metallurgica, 1982. **30**.
6. Acharya, A., J.L. Bassani, and A. Beaudoin, *Geometrically necessary dislocations, hardening, and a simple gradient theory of crystal plasticity.* Scripta Materialia, 2003. **48**.
7. Fleck, N.A., et al., *Strain gradient plasticity: Theory and experiment.* Acta Metallurgica Et Materialia, 1994. **42**.
8. Gao, H., et al., *Mechanism-based strain gradient plasticity - I. Theory.* Journal of the Mechanics and Physics of Solids, 1999. **47**.
9. Gudmundson, P., *A unified treatment of strain gradient plasticity.* Journal of the Mechanics and Physics of Solids, 2004. **52**.
10. Jain, A. and S.R. Agnew, *Modeling the temperature dependent effect of twinning on the behavior of magnesium alloy AZ31B sheet.* Materials Science and Engineering A, 2007. **462**.
11. Jain, A., et al., *Grain size effects on the tensile properties and deformation mechanisms of a magnesium alloy, AZ31B, sheet.* Materials Science and Engineering A, 2008. **486**.
12. Arul Kumar, M., I.J. Beyerlein, and C.N. Tomé, *Grain size constraints on twin expansion in hexagonal close packed crystals.* Journal of Applied Physics, 2016. **120**.
13. Kumar, M.A. and I.J. Beyerlein, *Influence of plastic properties on the grain size effect on twinning in Ti and Mg.* Materials Science and Engineering A, 2020. **771**.
14. Beyerlein, I.J., R.J. McCabe, and C.N. Tomé, *Effect of microstructure on the nucleation of deformation twins in polycrystalline high-purity magnesium: A multi-scale modeling study.* Journal of the Mechanics and Physics of Solids, 2011. **59**.
15. Ravaji, B. and S.P. Joshi, *A crystal plasticity investigation of grain size-texture interaction in magnesium alloys.* Acta Materialia, 2021. **208**.

16. Andani, M.T., et al., *A quantitative study of stress fields ahead of a slip band blocked by a grain boundary in unalloyed magnesium.* Scientific Reports, 2020. **10**.
17. Andani, M.T., et al., *Quantitative study of the effect of grain boundary parameters on the slip system level Hall-Petch slope for basal slip system in Mg-4Al.* Acta Materialia, 2020. **200**.
18. Taheri Andani, M., et al., *Estimation of micro-Hall-Petch coefficients for prismatic slip system in Mg-4Al as a function of grain boundary parameters.* Acta Materialia.
19. Aagesen, L.K., et al., *PRISMS: An Integrated, Open-Source Framework for Accelerating Predictive Structural Materials Science*, in *JOM*. 2018.
20. Yaghoobi, M., et al., *PRISMS-Plasticity: An open-source crystal plasticity finite element software.* Computational Materials Science, 2019. **169**.
21. Yaghoobi, M., et al., *PRISMS-Fatigue computational framework for fatigue analysis in polycrystalline metals and alloys.* npj Computational Materials, 2021. **7**.
22. Groeber, M.A. and M.A. Jackson, *DREAM.3D: A Digital Representation Environment for the Analysis of Microstructure in 3D.* Integrating Materials and Manufacturing Innovation, 2014. **3**.
23. Hielscher, R. and H. Schaeben, *A novel pole figure inversion method: Specification of the MTEX algorithm.* Journal of Applied Crystallography, 2008. **41**.
24. Saltykov, S., *Calculation of the distribution curves for the size of dispersed grains.* Plant Laboratory, 1949. **15**: p. 1317-1319.
25. Scheil, E. and A. Lange-Weise, *Statistische Gefugeuntersuchungen.* 1935.
26. Schwartz, H., *The metallographic determination of the size distribution of temper carbon nodules.* Metals Alloys, 1934. **5**: p. 139.
27. Long, T. and C.S. Smith, *Single-crystal elastic constants of magnesium and magnesium alloys.* Acta Metallurgica, 1957. **5**(4): p. 200-207.
28. Slutsky, L.J. and C. Garland, *Elastic constants of magnesium from 4.2 K to 300 K.* Physical Review, 1957. **107**(4): p. 972.
29. Zhang, J. and S.P. Joshi, *Phenomenological crystal plasticity modeling and detailed micromechanical investigations of pure magnesium.* Journal of the Mechanics and Physics of Solids, 2012. **60**(5): p. 945-972.
30. Kröner, E., *Allgemeine Kontinuumstheorie der Versetzungen und Eigenspannungen.* Archive for Rational Mechanics and Analysis, 1959. **4**.
31. Lee, E.H., *Elastic-plastic deformation at finite strains.* Journal of Applied Mechanics, Transactions ASME, 1964. **36**.
32. Asaro, R.J. and A. Needleman, *Overview no. 42 Texture development and strain hardening in rate dependent polycrystals.* Acta Metallurgica, 1985. **33**.
33. Anand, L., *Constitutive equations for hot-working of metals.* International Journal of Plasticity, 1985. **1**.
34. Kalidindi, S.R., C.A. Bronkhorst, and L. Anand, *Crystallographic texture evolution in bulk deformation processing of FCC metals.* Journal of the Mechanics and Physics of Solids, 1992. **40**.
35. Arndt, D., et al., *The deal.II library, Version 9.2.* Journal of Numerical Mathematics, 2020. **28**.

Chapter 6: Conclusion and Remarks about Future Work

High-resolution electron backscatter diffraction method was used to measure the local stress ahead of blocked slip bands at grain boundaries in a deformed Mg-4Al alloy for different grain boundaries. The results were combined with a continuum dislocation pile-up model to assess the slip system level Hall-Petch slope for basal slip system (k_μ^{basal}) and the prismatic slip system ($k_\mu^{prismatic}$). The results indicate that k_μ^{basal} values vary from 0.054 $\mathrm{MPa{-}m^{1/2}}$ to 0.184 $\mathrm{MPa{-}m^{1/2}}$ and $k_\mu^{prismatic}$ values vary from 0.138 $\mathrm{MPa.m^{1/2}}$ to 0.665 $\mathrm{MPa.m^{1/2}}$ which are almost three times larger than the calculated values for the k_μ^{basal}. The slip system level Hall-Petch slope values were correlated with the geometric descriptors of the GBs, and it was concluded that the angle between the two slip plane traces on the GB plane (θ), and the angle between slip directions (κ) were the two most effective geometric parameters in estimating the magnitude of the slip system level Hall-Petch slope values A relationship, $k_\mu^{slip\ system} = K^{slip\ system}(1 - \cos(\theta)\cos(\kappa))^c$, was suggested including both of these angles to estimate the slip system level Hall-Petch slope for basal and prismatic slip system and the model parameters, $K^{slip\ system}$ and c, were calibrated for Mg-4Al alloys (chapter 3 and chapter 4). In chapter 5, a procedure to incorporate the micro Hall-Petch equation into a CPFE framework to simulate the plastic behavior of microstructures, including the grain size and texture effects, was developed. A comparison of the stress-strain curves between CPFE and experiments using parameters proposed in previous work before calibration using four parameters – the basal and prismatic slip resistances and the basal and prismatic micro-Hall-Petch multipliers was presented.

Based on the results and conclusion discussed throughout this dissertation, the following recommendations are made for future work:

- It will be important to understand the micro-Hall-Petch relationship for twining systems. It has been previously shown that twining interactions with grain boundaries play a key role in understanding the strength of Mg alloy. However, there is no comprehensive experimental work to quantify the micro-Hall-Petch relationship for different twining slip systems in Mg alloys. Having such unprecedented understanding can help to future develop the current crystal plasticity models to better predict the role of grain boundaries in strengthening mechanisms in Mg alloys.
- This study assumes that the slip bands blocked at the grain boundaries observed in SEM represent the dislocation pile-up. To confirm this hypothesis, site-specific transmission electron microscopy (TEM) analysis should be used to experimentally observe the dislocation pile up at the grain boundaries. This provides more quantitative information about how dislocation interacts with grain boundaries and dislocation distribution around grain boundaries.
- The 1D continuum dislocation pile-up model used in chapters 3 and 4 is an oversimplification of the actual physics, which is much more complicated. Additionally, the back-stress that might arise from geometrically necessary dislocation (GND) distributions in the vicinity of the GB is not considered explicitly in the pile-up model. Their importance has been demonstrated in the context of large-grained titanium, where correlations were drawn between GND content and geometric metrics of the GB. However, quantification of this back-stress for informing micromechanical models like the present pile-up model should be performed.

- This study proposed the slip system level Hall-Petch slope as a function of geometric descriptors of the GBs and the model parameters, $K^{slip\ system}$ and $c,$ were calibrated for Mg-4Al alloys. However, the proposed relationship should be extended to the other polycrystalline materials. It is required to perform a fundamental study to understand the interrelationship between the model parameters and the properties of the materials, such as the CRSS values.